Postflight Aerothermodynamic Analysis of Pegasus® Using Computational Fluid Dynamic Techniques

Gary D. Kuhn
Nielsen Engineering & Research, Inc.
Mountain View, CA 94043-2287

NASA

National Aeronautics and
Space Administration

Dryden Flight Research Facility
Edwards, California 93523-0273

CONTENTS

ABSTRACT

The objective of this effort was to validate the computational capability of the NASA Ames Research Center's Navier-Stokes code, F3D, for flows at high Mach numbers using comparison flight-test data from the Pegasus® air-launched, winged space booster. Comparisons were made with temperature and heat fluxes estimated from measurements on the wing surfaces and wing-fuselage fairing. Tests were conducted for solution convergence, sensitivity to grid density, and effects of distributing grid points to provide high density near temperature and heat-flux sensors. The measured temperatures were from sensors embedded in the ablating thermal protection system. Surface heat fluxes were from plugs fabricated of highly insulative, nonablating material, and mounted level with the surface of the surrounding ablative material. As a preflight-design tool, the F3D code produces accurate predictions of heat transfer and other aerodynamic properties, and it can provide detailed data for assessment of boundary layer separation, shock waves, and vortex formation. As a postflight-analysis tool, the code provides a way to clarify and interpret the measured results.

NOMENCLATURE

CFD	computational fluid dynamics
CPU	central processing unit
D	diameter of vehicle fuselage
dy/dt	recession rate of the surface
H	heat of ablation
HRSI	high-temperature reusable surface insulation
I	longitudinal coordinate direction
J	circumferential coordinate direction
K	radial coordinate direction
k	thermal conductivity of the fluid, Btu/ft^2 sec, °R
M	Mach
NEAR	Nielsen Engineering and Research, Inc.
Pr	Prandtl number, Btu/ft^2 sec
q	convective heat flux, Btu/ft^2 sec
R	gas constant
S	Sutherland's viscosity ratio
T	temperature, °R
T_o	outer temperature, °R
T_w	surface temperature of vehicle (used in CFD calculations), °R
TPS	thermal protection system
∞	undisturbed, free stream

® Pegasus is a registered trademark of Orbital Sciences Corp., Fairfax, Virginia.

/.

α angle of attack, deg

ρ density of the material, lbm/ft^3

INTRODUCTION

Pegasus®, a three-stage, air-launched, winged space booster (fig. 1), was developed by private industry to provide low-cost launch services for small satellites. The aerodynamic design and analysis of Pegasus were conducted by Nielsen Engineering and Research (NEAR Inc., Mountain View, CA), without benefit of wind-tunnel and subscale model testing using only computational aerodynamic and fluid mechanic methods. The first flight of Pegasus in April 1990 provided data for evaluation and validation of the computational fluid dynamic (CFD) techniques.

The objective of this effort was to validate the computational capability of the NASA Ames Research Center's Navier-Stokes code, F3D, for flows at high Mach numbers using Pegasus flight-test data for comparison. Attention was concentrated on temperature and heat-transfer measurements in the region of the wing and wing-fuselage fillet, because these were the only data measured on the first flight.

BACKGROUND

To gain the advantages of increased payload performance and operational flexibility, Pegasus was designed to be carried aloft beneath the wing of a B-52 bomber aircraft. Performance improvements over ground launch are a result of the aircraft forward velocity and the initial launch altitude. Launch at 40,000 ft contributed to lower dynamic pressure, lower drag, and lower structural and thermal stresses; and the reduced atmospheric pressure range encountered by the first stage permitted optimization of the first-stage nozzle.

In level flight at Mach 0.8 and 40,000 ft, Pegasus was released from the carrier aircraft and allowed to free fall for 5 sec (fig. 2). After first-stage ignition, Pegasus began a 2.5-g pullup maneuver using wing lift and thrust while accelerating through the transonic speed regime and maximum dynamic pressure. When first-stage burnout occurred after approximately 82 sec, the vehicle had reached Mach 8.7 at an altitude of more than 200,000 ft. The first stage, which included all aerodynamic lifting surfaces, then separated from the second and third stages. The separation of the first stage corresponded to the end of the aerodynamic analysis.

Because of the heavy reliance on analytic tools in the aerodynamic and thermal protection design process, the first flight of Pegasus included some instrumentation designed to aid in evaluating the prediction methods. This instrumentation has a system of temperature sensors and heat-flux gauges installed on the wing surfaces, wing leading edge, and wing-fuselage fairing (or fillet). The temperature sensors were embedded in the ablating thermal protection system (TPS) to cause minimal perturbation of the local structure and thermal boundary layers. The heat-flux gauges were constructed by attaching thermocouples to plugs fabricated from highly insulative, nonablating material. The plug-surface temperatures responded rapidly to local aerothermal conditions and provided the basis for estimates of convective heat flux. The distribution of the plug-mounted sensors on the sidewall of the fuselage-wing fairing helped to identify the effects of the shock wave and compression field generated by the wing.

2

ANALYSIS METHODS

In the preflight analysis, results from the F3D code gave a corroborating value for aerodynamic loads predicted by less sophisticated methods, identified possible areas of flow separation, and provided evidence of the nature of the interaction between the wing leading-edge shock wave and the boundary layer on the wing-fuselage fillet. The thermal boundary condition used for the preflight analysis was zero heat flux to the surface of the vehicle. This boundary condition was modified for the postflight analysis to allow specification of the temperature on the vehicle surface, and to permit calculation of the convective heat flux at the surface.

The postflight analysis addressed five aspects of the CFD prediction method:

- Convergence of the solution

- Achievement of a steady physically realistic flow

- Sensitivity to small perturbations of angle of attack

- Sensitivity to grid density

- Agreement with experimental results

The first four aspects involve only the computer code itself. The fifth involves the computer code and experimental data from analysis of the aerothermal measurements from the first flight of Pegasus (ref. 1).

Analysis of Solution Convergence

Convergence of the CFD calculations is determined by monitoring several quantities representing important aspects of the numerical method. Specifically, the residuals of the numerical solution and the surface heat flux at a reference point are monitored at each iteration step. The integrated forces and moments on the configuration are also examined at several steps. The residuals are generally expected to become smaller with each iteration, eventually reaching zero, which for the computers used in this investigation is about 10^{-14}. The surface heat flux is expected to become constant after some initial transitional behavior. Similarly, the integrated forces are expected to approach constant values.

Evaluation of Physical Realism of Solutions

Another aspect of convergence is the achievement of a steady, physically realistic flow field. Departures from realism could occur if the grid were too coarse to resolve important features of the flow field. Departures from realism also might indicate a lack of convergence, though other indicators suggest convergence is occurring. The physical realism of calculated flow fields was evaluated by examining the degree to which predicted flow features, such as shock waves or vortical flow regions, were correctly located and smoothly modeled. The ultimate test of physical realism is comparison with measured experimental results.

3

Evaluation of Sensitivity to Small Angle-of-Attack Perturbations

Because the flight data showed that the angle of attack (α) and angle of sideslip (β) were subject to small perturbations even during steady parts of the flight, it was of interest to examine the sensitivity to such perturbations of the calculated flow field, especially with regard to the aerodynamic heating near the impingement of the wing leading-edge shock on the fuselage. The wing shock moved with time because of the varying attitude and the acceleration of the vehicle. The angle of attack sensitivity study was to find the effect of perturbations of angle of attack alone. Therefore, solutions were calculated at a typical Mach number for two angles of attack differing by one degree.

Evaluation of Sensitivity to Grid Density

One important aspect of the application of CFD to real aircraft configurations is the computational grid. The general requirement for the grid is that there be enough points to resolve important flow features. For a Navier-Stokes code, this generally requires many points near the vehicle surface to resolve the large gradients that occur. If shock waves occur in the flow field away from surfaces, it may be important to have a high density of grid points near the shock.

In this investigation, several grids were used. The basic grid was the finest grid used in the preflight computational analysis. All other grids were obtained by choosing subsets of the points on that grid.

Evaluation of Agreement with Experimental Results

Finally, the ultimate test of the validity of a CFD code is the degree to which it produces results that agree with experiment. For this test, the aerodynamic heating data from the first flight of Pegasus were used. The flight-measured data were from sensors distributed on the wing surfaces, wing leading edge, and wing–body fairing or fillet (ref. 1). Most sensors were thin foil gauges installed near the surface within the vehicle TPS. Besides the foil gauges, 10 thermocouples were installed on the surface of nonablating plugs (high-temperature reusable surface insulation (HRSI) plugs) placed on the fillet near the wing shock impingement. These sensors are more responsive to changes in flight conditions than the foils, and allow a derivation of convective heat flux.

Because of the differences in the thermal properties of the HRSI plugs and the other thermal protection materials, the interpretation of the measurements must be made with caution. The difficulties of measuring surface heat flux in the hypersonic environment were discussed by Neumann (ref. 2). The major problem in integrating heat-transfer instrumentation with the surface is that of nonisothermal walls. When a heat-flux gauge is placed on a surface, it often takes on a different temperature from the surface. This then produces an incorrect reading of the heat flux to the surface. Though the heat-flux gauge may be extremely accurate at measuring heat flux, it measures the wrong heat flux. Another complication arises when the heat-flux gauge is placed in an ablative surface. Not only is the gauge not at the same temperature as the surrounding surface, but the products of ablation are mixed with the air flowing over the gauge, making the measured heat flux difficult to interpret in terms of the heated air. According to Neumann, gauges so placed are useful for qualitative rather than quantitative measurements, such as determining when transition occurs or detecting the presence of shock waves. Even thermocouples are of limited usefulness in evaluating convective heat flux. The reason is that

4

thermal modeling of ablative structures is very difficult, and thermocouples cannot be placed directly on the ablating surface. The full aerodynamic heating is not captured by the material, because the surface is ablating. It is difficult to determine the heat associated with the ablation, because the effective rate of heat removal by ablation depends on the rate at which the surface material is being removed. The ability to infer the convective heat flux from measured temperatures or to measure that heat flux using calorimeters loses meaning when ablating structures are considered.

The analysis of the data from the heat-flux gauges and the uncertainties attributed to the placement of the gauges on a surrounding surface with very different characteristics have important implications for the comparison of the measured data with the CFD results. The comparison is further complicated by the transient nature of the experiment and the presence of products of ablation of the surface. The CFD analysis is for a steady flight at constant Mach number and angle of attack with a simple no-slip, constant temperature boundary condition and with air as the only constituent of the fluid flowing around the vehicle. In the actual flight, the Mach number was constantly increasing, the angle of attack varied with time, and the surface temperature varied over the entire vehicle.

The surface heat flux was determined from the HRSI plugs and also estimated from the foil gauge temperature measurements in the TPS material. Estimates were also made of the ablative contribution to the heat balance.

The convective heat flux was calculated from the CFD solution as follows:

$$q = -k\,dT/dy$$

where

q is the convective heat flux, Btu/ft^2 sec,

k is the thermal conductivity of the fluid, Btu/ft^2 sec °R

T is the temperature, °R, and

y is the distance normal to the surface, ft.

The thermal conductivity of the fluid (air) was determined from the properties of a perfect gas with ratio of specific heats, $\gamma = 1.4$, and Prandtl number, $Pr = 0.7$. Thus,

$$k = [\gamma R/(\gamma - 1)] \times S \times \mu_\infty/Pr$$

where S is Sutherland's viscosity ratio

$$S = \frac{(T_\infty + 198.6)}{(T + 198.6)}(T/T_\infty)^{\frac{3}{2}}$$

and R is the gas constant.

The temperature gradient, dT/dy, was approximated by the difference between the values at the surface and first grid point normal to the surface and by the distance between the first grid point and surface. Except for the HRSI plug locations, the surface temperature over the entire vehicle surface was assumed to be a single value corresponding to a rough average of the temperatures indicated by sensors on the fillet side wall. The convective heat flux was calculated at the surface for comparison with measurements from the HRSI plugs. In addition, the temperature at the plug locations was varied to study the accuracy of modeling the nonisothermal nature of the plug–surface integration.

SIMULATION MODEL

The simulation model consisted of the computational code and grids to describe the configuration geometry and provide a framework for calculating the properties of the flow field.

Computational Code

The computation of the flow field was accomplished with the code F3D (ref. 3). The code solves the compressible three-dimensional, thin-layer Navier-Stokes equations, uses upwind spatial differencing in a streamwise direction, and is either first- or second-order accurate in space. For the calculations described here, the accuracy in time is first order. For the present work, some minor modifications were made to F3D to allow the specification of surface temperature and calculation of convective heat flux at the surface.

Grid-Generation Methods

A major part of the preflight CFD study was the development of the computational grid. The Chimera composite-grid approach (ref. 4) was chosen for the discretization process to get an accurate model of the entire configuration. The grid required for simulating the flow field around Pegasus was composed of two sections. The first section enclosed the body and wing, extending one grid cell beyond the trailing edge of the wing. The second section extended from the wing trailing edge to the base of the body, including the tail control fins. For the forward section, because of the blunt nose and thick, round-edged wing, the grid was generated using the NASA–Ames code, HYGRIIID (ref. 5), a three-dimensional hyperbolic grid generator. Because of the aft section's simpler, more cylindrical geometry, its grid was generated using a NEAR code, HYPDAPT (ref. 6), a two-dimensional hyperbolic grid generator. The two-dimensional grid generator was applied to compute grids in cross sections. The cross-section grids were then connected to create a fully three-dimensional grid.

Fine Mesh

For the postflight analysis, since the only measurements of temperature and heat flux were from the wing and fillet regions, only the forward section of the grid was used. The complete grid for the forward section contained $92 \times 83 \times 51$ points, a total of 389,436 points. Several subsets of the original grid were used to evaluate the sensitivity of the calculated flow solution to the grid.

A portion of the fine grid is shown in figure 3. A perspective view of the grid in figure 3(a) shows the grid in the vertical symmetry plane, on the vehicle surface, and in a cross section at the trailing edge of the wing. In this report, the curvilinear coordinates of the grid are called by the index notation (I, J, K) where I is the longitudinal coordinate direction, J is the circumferential coordinate direction, and K is the normal, or radial, coordinate direction defined in figure 3(a). A closer view of the fillet and the locations of heat-flux gauges (HRSI plugs) is shown in figure 3(b). A side view showing the grid on the fuselage and wing in a two-dimensional projection is shown in figure 3(c). A cross section of the grid near the wing root leading edge is shown in figure 3(d).

Important features of the grid should be noted. On the nose, the grid is uniform in the circumferential direction in each cross section of the body. Approaching the section where the fillet begins, the grid points on the body are clustered near the top of the body for use in defining the contours of the fairing and, subsequently, the wing. This clustering was necessary to maintain the number of circumferential points constant.

First Coarse Mesh

The first subset of the fine grid used for the analysis was shown in figure 4. This subset was derived by omitting alternate points in each of the three grid directions, with the exception that the first three points and the last three points were retained in the I and J directions. This ensured proper definition of the nose, wing trailing edge, and vertical symmetry plane. In the K direction, the first three points were retained to maintain the best resolution of the boundary layer at the vehicle surface. This grid is subsequently called the "sml" grid. It contained $49 \times 46 \times 26$ points, a total of 58,604 points. A sample side view and a cross section corresponding to those in figures 3(c) and (d) are shown in figures 4(a) and (b). The lines defining the wing edges, wing root, and outline of the fillet are highlighted by symbols in figure 4(a). The specific points corresponding to the location of heat-flux gauges on the vehicle are also shown.

Intermediate Mesh

The second subset grid (fig. 5) was obtained by removing fewer points from the fine grid. In the I direction, between the nose and the beginning of the wing-fuselage fairing, alternate points were omitted from the fine grid. All I points were retained under the wing, until well aft of the experimental heat-sensor locations. Alternate I points were then omitted for the remainder of the grid to the wing trailing edge. In the J direction, alternate points were used for the part of the grid corresponding to the wing and to the part of the body away from the fillet. The remaining points which fall on the fillet were retained as for the fine grid. Finally, for the K direction, the first 10 points were retained from the fine grid, and after that, alternate points were omitted. The final grid configuration had $73 \times 54 \times 30$ or 118,260 points. This is designated the "mm" grid. A sample side view and cross section corresponding to those in figures 3(c) and (d) are shown in figures 5(a) and (b).

Second Coarse Mesh

The final subset grid was a compromise between the sml and mm grids, developed to maintain the resolution of the fine grid over the fillet while also achieving the computational speed of the sml grid. It had the same number of points as the sml grid, but the distribution of points was similar to the mm grid. Points were chosen from the fine grid in all three directions to retain the complete grid over the fillet where the experimental measurements were obtained. In the K direction, the first five points were the same as for the fine grid, but the coarseness of the grid increased toward the outer boundary. This grid was designated the "sm2" grid. A sample side view and cross section corresponding to those in figures 3(c) and (d) are shown in figures 6(a) and (b). This grid was used for most of the comparisons with experimental data and other evaluations presented in this report.

FLIGHT-MEASURED DATA

Trajectory Data

The angle of attack and Mach number on the flight trajectory are presented in figure 7. Three cases were selected for comparison at 40, 50, and 60 sec in the flight trajectory. The Mach number at these times was 3.1, 4.0, and 5.0, respectively (fig. 7(a)), and the angle of attack was 7.5, 4.0, and 0.5°, respectively (fig. 7(b)). A typical plot of temperature variation at a sensor located under the ablative outer layer of the surface TPS material is presented in figure 7(c).

Free-stream flow conditions were from data provided in reference 1. The data were from postflight analysis of inertial data from an onboard inertial navigation system, ground-based radar, and atmospheric data from balloons, stratospheric charts, and climatological information. The required values of p_∞, T_∞, and ρ_∞ were from the pressure altitude presented in figure 8, from reference 1, and from Standard Atmosphere charts in reference 7.

The three cases provided three levels of difficulty in interpreting and correlating the calculated results. At 40 sec, where $M_\infty = 3.1$, $\alpha = 7.5°$, the angle of attack had been steady for several seconds and the surface temperature had apparently not yet reached the ablation temperature of the ablative coating on the fillet sidewall. This conclusion is not certain, however, since the temperature sensors were not on the outer surface but the inner surface of the layer of ablative material. An approximate analysis of the heat flow in the structure yielded a temperature difference of 10 °F between the sensors and the outer surface. At 40 sec, the temperature and heat transfer measurements should be free from the uncertainty that may be caused by the presence of the products of ablation. There is still the uncertainty, though, because of the nonisothermal nature of the placement of the heat-flux gauge in the ablative material. In addition, the 40-sec point is in the middle of an interval of rapidly rising temperature.

The second case, at 50 sec, corresponded to $M_\infty = 4.0$ and $\alpha = 4.0°$. The angle of attack was changing rapidly in a pitch-down maneuver (fig. 7(b)), while the temperature indicated by the embedded gauges in the fillet insulation was beginning to become steady as the TPS material began to ablate (fig. 7(c)). The measurements at the HRSI plugs were subject to uncertainty because of the presence of ablation products and the nonisothermal effects of the difference between the temperatures of the plugs and the surrounding surface.

The third case, at 60 sec, corresponded to $M_\infty = 5.0$ and $\alpha = 0.5°$. The angle of attack was nearly constant, and the temperatures of both the TPS material and the HRSI plugs had begun to stabilize. The level of the temperature of the TPS material suggests that ablation was keeping the temperature from increasing. The meaning of the convective heat-flux measurements from the HRSI plugs is subject to the uncertainty of the effect of the products of ablation on the composition of the fluid in the boundary layer. The specific conditions used for the CFD calculations for each case are summarized in table 1.

8

Surface Temperature Distribution

The temperature distribution on the Pegasus vehicle was known from measurements at a few locations on the wing, wing leading edge, and wing-fuselage fairing. From those measurements, a nominal value for the temperature on the entire surface was estimated for the three specific times in the flight discussed previously.

The Pegasus TPS consisted of insulative and ablative materials in various combinations applied to the external surface of a graphite–epoxy substructure. Four materials were used, two ablative and two insulative. The details of the installation of the TPS are presented in reference 1. The material used on the fillet sidewall is known as Thermolag (Thermal Science, Inc., St. Louis, Missouri), and it is a low-temperature polymer ablative that sublimates at about 230 °F. The Thermolag material was sprayed on the fillet sidewall, over a layer of cork phenolic insulator.

Foil thermocouples were installed between the Thermolag and the cork. The details of the installation are presented in reference 1. A rough analysis, using the properties of the Thermolag material, the nominal layer thickness, and the measured temperature and rate of temperature increase on the Thermolag–cork interface, produced an estimated difference of 10 °F between the cork and outer surface of the Thermolag. The surface temperature boundary condition for the CFD analysis was assumed to be 10 °F hotter than the measured temperatures. Temperatures at the plug surfaces were assumed to be the temperatures at the fluid boundary, since the thermocouples were separated from the fluid by only a thin protective coating.

Convective Heat Flux (High-Temperature Reusable Surface Insulation Plugs)

The HRSI plugs were constructed from solid pieces of shuttle tile material, LI2200, 1-in. wide and 0.4-in. thick. Thermocouples were fabricated from small-diameter (0.005 in.) wires mounted on the surface of the plugs. A high-temperature, high-emissivity coating was applied over the thermocouples. The emissivity of the coating was 0.85. The locations of the plugs on the fillet sidewall are shown in figure 4(a).

The HRSI plugs were generally hotter than the surrounding surface by more than 100 °F. Thus, at the first point of comparison, where $M_\infty = 3.1$ and the temperature at the Thermolag–cork interface had not reached the ablative temperature, the plug was a small, hot surface surrounded by a cooler surface. At the other two points of comparison, the plugs were in an atmosphere containing products of ablation of the surrounding surface.

The convective heat flux was found experimentally as the sum of the radiative and conductive heat flux away from the surface of the HRSI plug as determined from the measured temperatures at the surface of the plug (ref. 1). Thus, the heat flux derived from the flight data did not depend upon the properties of the fluid flowing over the plug, but only on the temperature distribution as measured in the plug. Conversely, the CFD analysis depended upon the properties of the fluid. In the CFD calculations, the convective heat flux was calculated directly by a finite-difference formula, assuming air as the working fluid.

Convective Heat Flux (Ablative Surfaces)

From the measured temperatures and their time history at the interfaces between the various layers of the TPS, it was possible to estimate the convective heat flux to the surface surrounding the HRSI plugs on the fillet and to the wing surface. The estimate was subject to large errors because of the uncertainty of the exact conditions on the outer surface of the material, but it provided a rough figure to aid in putting the heat flux calculated by the CFD analysis in perspective. The heat-flux estimate assumed an emissivity for the outer material, either Thermolag or Firex (Pfizer Minerals, Pigments and Metals Division, New York, New York), of 0.5.

If the surface is assumed to be planar and the various layers of material uniform in thickness, a one-dimensional analysis can be applied. The components of the flow of heat into the TPS are shown in figure 9. The temperatures T_1, T_2, and T_3, and the density and heat capacity of the materials were known (ref. 1). The convective heat flux is thus the sum of the radiation from the outer surface, the rate of increase of internal energy of the entire composite layer, and a heat flux caused by ablation, if applicable. It is written as

$$q_c = q_{i1} + q_{i2} + q_{i3} + q_r + q_a$$

where q_c is the convective heat flux, Btu/ft^2 sec, q_a is the heat flux caused by ablation, q_{in} is the rate of increase of internal energy of layer n, and q_r is the radiation of heat from the outer surface,

$$q_{in} = \rho y C_p (dT/dt)$$

where ρ is the density of the material, lbm/ft^3, y is the thickness of the layer, ft, C_p is the thermal capacity of the material, Btu/lbm sec ft^2 °R, and

$$q_a = \rho H (dy/dt)$$

where H is the heat of ablation, and dy/dt is the recession rate of the surface. The ablative contribution will be present when the outer temperature T_o reaches the ablation point of the outer layer. Values of q_c for the fillet and wing were estimated to range from 0.2 to 1.0 Btu/ft^2 sec without the ablative contribution, somewhat lower than the calculated surface convective heat flux.

RESULTS AND DISCUSSION

Initial Conditions for Computational Fluid Dynamic Calculations

Two methods of starting CFD calculations are discussed. The first method employed a uniform free-stream flow over the entire computational grid, gradually applying the no-slip condition at the vehicle surface over the first 30 iteration steps. This method is subsequently referred to as a cold start. The second starting method used a converged solution for $M_\infty = 5.0$, $\alpha = 5.0°$ and then gradually changed the value of M_∞ or α until the desired values were reached. The solution was then allowed to run until converged. This method is subsequently referred to as a warm start. The second method was developed to test the idea that computer time and effort could be reduced by using an existing solution for slightly different flow conditions.

For the calculations discussed here, the warm start initial condition was the preflight solution for $M_\infty = 5.0$, $\alpha = 5.0°$ converted from the fine mesh grid to the first coarse mesh (the sml grid). Because

10

the modified grid was a simple subset of the original grid, it was possible to use the preflight solution as a starting condition with no interpolation by simply selecting the computed flow properties at the corresponding grid locations. The starting condition was an approximation to a converged solution for $M_\infty = 5.0$, $\alpha = 5.0°$, with the adiabatic or zero temperature gradient condition at the vehicle surface. The solution was changed to $M_\infty = 5.0$, $\alpha = 0.5°$ and $M_\infty = 4.0$, $\alpha = 4.0°$ by adjusting the Mach number and angle of attack in step increments of 0.5 and 0.5°, respectively, from the starting solution, and running each step 100 iterations. When the final conditions were reached, the solution was allowed to run for 500 to 1000 additional iterations. When the final Mach number and angle-of-attack conditions were reached, a final change was made to adjust from the adiabatic surface condition to a condition of specified surface temperature.

Solution Convergence

For studies of solution convergence and the achievement of flow-field realism, solutions on the sml grid initialized with the preflight calculations on a fine mesh (warm start) were compared with solutions started from uniform free-stream conditions.

The history of the residuals of the solution from a warm start is shown in figure 10 for two cases. Figure 10(a) shows the history of the $M_\infty = 4.0$, $\alpha = 4.0°$ case during the transition from the original $M_\infty = 5.0$, $\alpha = 5.0°$ conditions, and figure 10(b) shows the history for the $M_\infty = 5.0$, $\alpha = 0.5°$ case during the transition from the same initial condition. Starting from $M_\infty = 5.0$, $\alpha = 5.0°$, both cases underwent a transient period in which the residuals decreased from a value of about 0.3 to values of about 10^{-4}. This is a rough indication of convergence of the solution.

Another indication of convergence is presented in figure 11. The heat-transfer rate at a reference point on the wing-fuselage fairing under the wing is shown for the two cases, $M_\infty = 4.0$, $\alpha = 4.0°$ and $M_\infty = 5.0$, $\alpha = 0.5°$, in figures 11(a) and 11(b), respectively. The reference point was chosen as a point near the actual HRSI locations, and it is indicated by an R in figures 4(a), 5(a), and 6(a). The specified temperature of the surface in both cases was 500 °F, the temperature of the HRSI plugs. Behavior suggestive of a converging solution was found for both cases, namely, a transient period in which the Mach number and angle of attack change at 100-iteration intervals, followed by a stable period. The curves in figure 11 have not reached a definite equilibrium; however, they appear to be approaching an asymptotic value.

As a better approximation to the actual conditions on the surface of the vehicle, a lower surface temperature of 250 °F was specified at iteration 3660, keeping the temperature at 500 °F at the HRSI plug locations, and the calculations shown in figures 10 and 11 were continued. The results after several hundred iterations more are shown in figures 12 and 13. When the value of T_w was changed, at iteration number 3660, the residual underwent a transient period for about 400 iterations, and then became essentially constant (fig. 12). Similarly, the heat transfer at the reference point appears to converge to a high value in the early iterations (fig. 11), and then to reach a lower value after the temperature was changed (fig. 13). However, the trends shown in these figures, especially with regard to the residuals, leave some doubt as to the degree of convergence of the solution.

The case for $M_\infty = 5.0$, $\alpha = 0.5°$ started from uniform flow conditions (cold start) was calculated on the sml grid for 3600 iterations. The complete history of the residuals of the solution is shown

11

in figure 14. The calculation revealed an asymptotic tendency of the residuals to reach a minimum value. This same tendency was exhibited by the case of the warm start using the result of the preflight calculations as the initial solution.

Another indication of convergence is presented in figure 15. The convective heat flux at the reference point on the wing-fuselage fairing under the wing is shown for the cold start for the case M_∞ = 5.0, α = 0.5°. This result was different from the warm start case in the sense that it appeared to reach a constant level, rather than an asymptote. Other quantities, such as integrated loads, also indicated convergence to constant values. Thus, it appeared that the solution can be considered converged.

The case for M_∞ = 4.0, α = 4.0° was also started from uniform flow conditions. The results for that case are shown in figures 16 and 17. The residuals shown in figure 16 displayed the behavior expected of a convergent solution, decreasing from large values continuously toward zero. After 6000 iterations, the residual reached a low value of less than 10^{-10}. The convective heat flux at the reference point reached a constant value fairly early in the calculation and remained at that value. This case was considered converged after 2400 iterations.

It is concluded that either approach to starting the calculations can provide a satisfactory result. The best approach generally is the cold start, starting from uniform flow conditions with the correct input parameters, rather than a start from a solution with different free-stream conditions and surface boundary conditions (as was the case for the warm start). The cold-start approach eliminates uncertainty regarding the quality of the starting solution and the manner in which the desired free-stream and boundary conditions are reached. The quantities of interest, such as convective heat flux, integrated loads, and flow-field properties converge to within practical tolerances in relatively few iterations compared with the number of iterations needed to achieve a near-zero value of the solution residuals. A solution can be achieved quickly on a coarse grid and then transferred to a finer grid for further convergence.

Flow-Field Realism and Solution Accuracy

In the following section, several aspects of the CFD solution are examined. First, the velocity vectors near the surface are shown, revealing the strong influence of the wing-fuselage fairing on the flow in the boundary layer. Second, the pressure in the flow field is examined in several surfaces of the computational grid to show how the solution captured the important phenomena in the flow field, such as the bow shock on the nose and the wing leading-edge shock wave. Third, the temperature variation normal to the fillet surface is presented to illustrate the definition of the temperature profile for determining the heat flux at the surface. Finally, boundary layer state is discussed.

Velocity Vector Field

The flow field for the case M_∞ = 4.0, α = 4.0° as calculated with the second coarse grid (the sm2 grid) is shown in figure 18. The velocity vectors at the first grid-point away from the surface (K = 2) are shown in a perspective view (fig. 18(a)), looking toward the tail from a viewpoint that is two body diameters ahead of the wing and aligned with the wing plane and wing tip. The data at every fourth grid point in the J direction are presented (recall figure 3 for the definitions of I, J, and K) to avoid confusion, and a few lines of the body grid have been included to aid in identifying the flow. The vectors at a grid surface farther from the fuselage surface (K = 7) are shown in figure 18(b).

12

The wing-fuselage fairing is seen to have a large influence on the flow in the boundary layer, causing the flow as viewed in planes normal to the body axis to reverse direction relative to the outer flow (fig. 18(c)). The fairing causes a swirling of the flow as it approaches the region under the wing.

Flow Contours

The shock wave at the nose of the Pegasus vehicle is shown for the $M_\infty = 5.0$ case in the density contours in figure 19(a). The contours are concentrated about a maximum density of about 5.0 (all flow properties in the CFD code are normalized by free-stream values). The location of the shock was more easily determined from the profile of density (fig. 19(b)) or stagnation density (fig. 19(c)) along a grid line emanating from the stagnation point of the nose. The specific grid line for these profiles is the K line for $I = 2$ and $J = 45$, in the lower plane of symmetry. The off-axis grid line was used for this plot because the small angle of attack displaced the stagnation point from the axis. The outline of the nose is also shown in the figures. From figure 19(b), the point where the density begins to increase as the flow approaches the body is about 0.05 body diameters from the surface. This also corresponds to the point in figure 19(c) where the stagnation density drops to the after-shock value before rising through the boundary layer to the value at the surface. This point is about 0.16 nose radii and compares favorably with the results presented in reference 8.

The other prominent shock wave in the flow field around the Pegasus vehicle formed at the leading edge of the wing. The wing leading edge had a small radius, and the shock was therefore detached from the wing. The shock would be expected to impinge on the fillet at a location determined by the sweep angle of the wing. The pressure jump across the shock decreased with distance from the wing leading edge; therefore, the pressure jump at the fillet impingement line would be expected to decrease moving aft. The swirling nature of the flow in the fillet region would be expected to interfere with the shock wave, further reducing the jumps in flow properties along the impingement line. Finally, the coarseness of the grid in the region between the wing and the fillet may cause a spreading of the shock wave that further reduces the calculated effect on the fillet.

Examples of the wing shock wave are presented in figure 20. Contours of pressure are shown in a cross section through the wing (fig. 20(a)), and in the grid surface near the edge of the boundary layer (fig. 20(b)). The contours of constant pressure in a cross section near the wing root leading edge show the expected concentration around a high pressure at the wing leading edge. The shock wave can be traced along a line of decreasing pressure defined by the locus of points where the contours of constant pressure change direction (dashed line in figure 20(a)). The shock wave also spreads with distance from the leading edge, so that the impingement region on the fillet sidewall is not a sharp line.

The next three parts of figure 20 show the evidence of the wing shock impingement on the fillet. First, in figure 20(b), the contours of constant pressure on a surface near the edge of the boundary layer (K = 7) on the body are shown in a side view. The plot is a projection of the three-dimensional wing-body surfaces onto the two-dimensional plane of the paper, the same view shown in the grid definition, figure 6(a). The part of the fillet where the HRSI plugs are located is nominally parallel to the plane of the paper, so that most distortion in the view is in the contours outside the region of interest. The highest pressure occurred at the intersection between the wing and the fairing (at an axial station about 6.25 on the figure). The pressure decreased as the flow moves away from that corner. It is recalled (figs. 18(a) and (b)) that the flow in this region was very complicated, moving nearly vertically

13

downward near the surface of the vehicle and becoming more axially oriented farther from the surface. The wing leading-edge shock wave was therefore not expected to be clearly discernible on the fillet. The shock wave appears to have had some influence on the flow over the fillet, since near the aft set of HRSI plugs the pressure contours are aligned with a line that approximates the Mach angle.

The influence of the wing shock wave is even more in evidence in the contours of velocity magnitude at the edge of the boundary layer shown in figure 20(c). This figure shows that the velocity contours formed a line extending from the wing–body junction over the fillet at an angle near the Mach angle.

The temperature contours on the K=2 grid surface parallel to the fillet surface are presented in figure 20(d). This variation of temperature is similar to the variation of heat flux to the surface, since the temperature was constant in the grid surface that coincides with the fillet surface. The temperature distribution in this grid surface suggests that the maximum heat flux occurred along the same line described for the pressure and velocity contours. For this Mach number, the HRSI plugs in the front of the top row and the back of the middle row have the maximum heat flux according to the calculation. This is also consistent with the experimental results to be discussed subsequently.

Temperature Variation Normal to the Fillet Surface

To calculate accurately the heat flux at the surface, it was essential that the computational grid was spaced closely enough near the surface to provide an accurate determination of the temperature gradient. Examples of the temperature variation normal to the fillet sidewall are shown in figure 21. In figure 21(a), the grid used in the heat-flux calculations is illustrated. A cross section including the wing is shown with the grid lines that pass through the locations of the HRSI plugs. The grid lines are normal to the fillet sidewall for a distance that includes several grid lines. The temperature variations shown in the next two figures (21(b) and (c)) are the profiles of the temperature along lines that are normal to the fillet sidewall until well past the peak temperature. In the figures, the body cross section is included to aid in locating the temperature profile. An arrow and the grid line in each figure show the location of the profile on the cross section. The scale of the vertical axis is the normalized temperature. The temperature profiles, represented by symbols in figures 21(b) and (c), show that the temperature at the surface was cooler than the peak temperature in the flow. The peak temperature occurred within the boundary layer on the surface.

The profile shown in figure 21(b) is expanded in figure 21(d) to illustrate more precisely the nature of the variation near the surface. The curvature of the temperature profile is evident in this figure. An estimate of the accuracy of the temperature gradient as determined from the temperature values at the surface and at the first grid point away from the surface can be made by calculating the gradient using the surface temperature and the temperatures at the first two grid points individually. Extrapolation of these temperature gradients to the wall yields a value of approximately 750. The value for the first grid point is 673, an error of approximately 10 percent. The heat flux calculated from the CFD solution would also be low by 10 percent because of this error in the temperature gradient at the surface. For this distribution, there is positive convective heat flux to the surface from the air flow.

14

State of Boundary Layer Flow

For the calculations shown in this report, the boundary layer was assumed to be laminar. At the lower Mach numbers, it is possible that the boundary layer on the actual vehicle in flight is turbulent on the body and fillet because of the high Reynolds numbers. On the wing, the boundary layer may be laminar in all cases because of the short distance for boundary layer growth. On the other hand, since the wing blends smoothly into the body, some boundary layer streamlines will go from the body directly onto the wing, providing the possibility for more boundary layer growth and increasing the probability of turbulence developing. In the absence of sufficient data to identify the exact state of the boundary layer, the laminar option was used throughout the CFD calculations.

Studies of Sensitivity to Small Angle-of-Attack Perturbations

Because the flight data show that the angle of attack and angle of sideslip are subject to small perturbations even during steady parts of the flight, it is of interest to examine the sensitivity of the flow field to such perturbations. For the present effort, with limited time and computer resources, only perturbations in angle of attack were examined. Perturbations of the angle of sideslip will require a grid that surrounds the configuration, and require twice the computer resources of the present case.

In table 2, the heat fluxes at the HRSI plug locations are listed for the case of $M_\infty = 5.0$ and angles of attack of $0.5°$ and $1.5°$. The calculations were performed using the sml grid (fig. 4). A $1.0°$ change in angle of attack produced a perturbation in the heat flux in these calculations ranging from -3 to $+9$ percent of the $\alpha = 0.5°$ value.

In figure 22, the calculated temperature contours in the $K = 2$ grid surface are presented for the two angles of attack. There are barely perceptible differences in the contours over the fillet.

Studies of Effect of Grid Density

It is usually considered important for CFD calculations of surface convective heat flux that the computational grid is of sufficient density to resolve accurately the steep gradients of temperature and velocity near the surface. In the present calculations, the grid was always the same as the finest grid in the normal direction for the first three points near the surface. The grid density varied greatly in the other two directions. In this section, the effect of these variations is discussed.

Heat Flux Along Grid Lines

In figure 23, the heat flux along grid lines on the fillet is presented for the three grids used in the analysis. Recall that the sml grid (fig. 4) is a simple subset of alternate points of the finest grid, and the mm (fig. 5) is a grid with more points containing all the fine grid points on the fillet and the points of the sml grid elsewhere. Recall too that the sm2 grid (fig. 6) is a compromise between the sml and mm grids, containing the fine grid points on the fillet and selected points elsewhere to result in a grid with the same number of points as the sml grid. The calculated heat flux was strongly influenced by the spacing of points in the direction tangential to the surface. Figure 23(a) shows the heat flux along a grid line coinciding with the bottom row of HRSI plugs. The sml grid gave a low value of heat flux, while the

15

sm2 grid gave a high value; the mm grid prediction was between the other two. The sharp deviations in the curve result from the specification of different temperatures at the grid points corresponding to the HRSI plugs than for the surrounding surface. This will be discussed later in the section on comparison with experimental results. In the CFD grid, the plugs are represented by single points, because even the finest grid did not have sufficient resolution to place more than one mesh point on each plug. The results are similar for three grid lines near the middle row of HRSI plugs (fig. 23(b)) and for four grid lines near the top row (fig. 23(c)). There was generally closer agreement between the prediction of the mm and sm2 grids, leading to the conclusion that the density of the grid in the tangential directions is important and must be considered along with the grid spacing normal to the surface.

Pressure Contours in a Cross Section

Other flow properties also revealed differences between the three grids. The contours of constant pressure indicated that the sm1 grid allows the wing leading-edge shock wave to diffuse more rapidly than the other two grids. The contours of constant pressure under the wing in figure 24(a) are slightly more round, that is, less elongated than the contours in figures 24(b) and (c), but the differences are small. The three grids appear to have similar accuracy for resolving the flow field. Good results for engineering purposes can be obtained by using a fine mesh where needed, while keeping the number of grid points low to increase running speed.

Evaluation of Computer Code Speed

Most of the required calculations for this effort were performed on the Numerical Aerodynamic Simulator Facility at NASA Ames Research Center, using both the Cray Y-MP and the Cray-2 computers. Results on the second coarse grid (the sm2 grid) were obtained using the Cray Y-MP8/832 computer in the Central Computer Facility at NASA Ames Research Center. Running times per iteration step on the fine and coarse grids are compared in the following table:

Computer	Grid	Number of grid points	CPU time/ step (sec)
Cray Y-MP	fine	389,436	16
Cray Y-MP	coarse	58,604	2.5
Cray-2	fine	389,436	33
Cray-2	coarse	58,604	5

A typical run of 1000 iterations for the coarse grid required about 40 min of central processing unit (CPU) time on the Cray Y-MP, or 80 min on the Cray-2. The same number of iterations for the fine grid required 5 hr on the Y-MP and 10 hr on the Cray-2; however, the solution was not as nearly converged on the fine grid as on the coarse grid. Since the coarse grid was found to yield adequate results when the grid points are concentrated where experimental data were available for comparison, it was cost effective to obtain solutions on the coarse grid. These results suggest that when a fine-grid solution is required, it is advantageous to obtain first a solution on the coarse grid. Then that solution can be transferred to the fine mesh for final processing. This will minimize the iterations required to obtain a converged solution on the fine grid.

16

Comparison with Experimental Results

In this section, comparisons are made with measurements taken during the first flight of Pegasus. To compare with the experiment, the surface temperature should have been specified over the entire fuselage and wing surface to correspond to the actual temperature. However, this was not feasible for several reasons. First, the actual temperature was only known at a few locations on the wing and fuselage-wing fillet. Second, the F3D code as then configured did not contain the required arrays to accommodate a table of temperatures for each surface grid point. Because of the lack of knowledge of the temperature distribution over most of the vehicle and to avoid the necessity of extensive modification of the code, a constant temperature was applied to the entire surface. This approach provided sufficient information to evaluate the heat flux in the region of the fillet. The temperature used was a nominal value from the available measurements as an average of the values indicated by the heat sensors under the Thermolag ablator on the fillet plus 10 °F to account for the temperature drop through the Thermolag layer. This temperature was specified everywhere except at the grid locations corresponding to the HRSI plug locations. The temperature specified at the plug locations was the value at which the HRSI plugs indicate a steady temperature after 50-60 sec of flight.

The locations of the HRSI plugs and grid points for comparison and reference heat-flux calculations are shown in figures 4–6. Comparison of figures 4 and 6 shows the relationship of the two coarse grids to the locations of the plugs. The first coarse grid (the sml grid) was a simple subset of the fine grid, with the experimental plug locations roughly at the center of grid elements. The points of the sml grid at which plug temperatures were specified are indicated by an x in figure 4(a). The temperature at the reference point, designated by R, was always specified as the temperature of the TPS surface. Figure 6(a) shows the second coarse grid for which the plug locations correspond to points of the grid and the grid retains the density of the fine grid near the plugs. The points on the intermediate (mm) grid corresponding to the plugs are shown on figure 5(a).

Heat Flux at High-Temperature Reusable Surface Insulation Plugs

As described previously, the HRSI heat-transfer gauges were constructed of shuttle tile material with a high-temperature, high-emissivity coating (ref. 1). Thermocouples were mounted with the junction under the coating. The gauges measured a surface temperature on an insulated, nonablative surface. From this temperature and the properties of the plug, the experimental convective heat flux was obtained. One goal of the application of the F3D code was to predict that heat flux. Since the plugs were surrounded by ablative material, however, the mean surface temperature near the plugs was more nearly equal to the ablation temperature of the TPS coating. Therefore, while the HRSI plug was nonablative, the air flowing over it was contaminated with the products of the sublimation of the surrounding surface and was somewhat cooler than would be the case if the entire surface was at the temperature of the plug.

Figure 25 shows the distribution of heat flux as represented by the HRSI plugs and calculations on the sml grid for the $M_\infty = 5.0$, $\alpha = 0.5$ case. The agreement is fairly good for most of the plugs for both the calculations started from uniform flow conditions, and the calculations restarted from the preflight solution. The data have been presented in groups according to the Z-level of the plugs or grid points. The specific points and their locations are shown in table 3 (X is measured from the nose, Z from the body centerline) and figure 4(a).

The agreement is fairly good for the first two groups in the list, points 1-4 and 5-7 (fig. 25(a) and (b), respectively). These are the gauges in the two highest rows. According to the preliminary analysis of the location of the wing leading-edge shock, points 3, 4, and 9 were directly under the impinging shock wave. The agreement between the predicted and measured heat flux for points 1-7 and for point 10 (fig. 25(c)) suggests that the shock location was predicted accurately by the CFD analysis. On the other hand, points 8 and 9 do not agree so well. This lack of agreement may be attributable to the coarse grid that did not adequately resolve the shock wave, causing the effect of the shock wave to be spread over an unrealistic area and, therefore, weakened. Thus, while the grid resolution seemed adequate in the direction normal to the surface for calculating the convective heat transfer, it was not adequate in the axial direction for resolving the oblique shock wave in the flow field.

Heat Flux Along Grid Lines from sm2 Grid

The sm2 grid was designed to improve the resolution of the solution in lateral directions as well as in the normal direction in the measuring region of the fillet. The calculations discussed previously indicated that the sm2 grid gave results more in agreement with the mm grid than the sml grid for the $M_\infty = 5.0$, $\alpha = 0.5°$ case. In this section, the sm2 grid is used to show the variation of surface heat flux along the fillet for all three test cases. The heat flux is presented as calculated along grid lines that pass through the HRSI plug locations along with the measured heat flux as derived from the HRSI plugs. Values of the heat flux from the plugs are listed in table 3.

Figures 26(a), (b), and (c) show the heat flux along the grid line that passes through plugs 8, 9, and 10. In both the calculations and measurements, there was an increase in the heat flux with increasing Mach number. However, there was also a significant difference between the measured and calculated results. It is believed that the difference was primarily because of the uncertainty of the conditions at the HRSI plugs. For the $M_\infty = 4.0$ and 5.0 cases (fig. 26(b) and (c)), the plug temperature was specified in the calculations to be the same as the measured temperature so that a lower, sometimes negative, heat flux was produced. The calculation could obviously be calibrated to produce the correct heat flux at the plugs. The higher level of heat flux on the surrounding surface was consistent, however, with the estimated heat flux discussed previously if the heat of ablation is included. The flight data indicated that the temperature at the inner side of the ablative outer layer of TPS material was near the ablation temperature for the higher Mach number cases. For the $M = 3.1$ case (fig. 26(a)), the temperature was increasing so rapidly that a calculation based on a steady temperature cannot be expected to agree exactly.

Similar results and conclusions are found in the middle and top rows of plugs as displayed in figures 27 and 28. While the heat flux for $M_\infty = 3.1$ was nearly constant along the fillet as indicated in figure 26, the highest heating rate for the highest Mach number was at the forward plugs of the top row as shown in figure 28. This effect was believed to be caused by the impinging wing leading-edge shock wave. Further evidence of this conclusion will be presented in the next section.

Temperature Distribution on Grid Surface K = 2

In figure 29 several plots of temperature contours are shown on the first grid surface over the fillet. This temperature distribution corresponded approximately to the heat-flux distribution, since the wall temperature was constant except for the HRSI plug locations. The view is a two-dimensional projection of the side view of the vehicle showing the characteristic diagonal contours near the plugs in all three

18

cases. In figure 29(a) for $M_\infty = 3.1$, $\alpha = 7.5°$, the temperature at the HRSI plug locations was the same as all other surface points, so a smooth variation of temperature was produced at the first grid surface away from the boundary. The contours show that the highest heating rate occurred around plugs 6, 7, and 10.

In figure 29(b) and (c), for $M_\infty = 4.0$, $\alpha = 4.0°$ and $M_\infty = 5.0$, $\alpha = 0.5°$, respectively, the plugs are hot spots as indicated by the dense grouping of temperature contours around the plug locations. The diagonal shock-induced pattern was present as for the $M_\infty = 3.1$ case, and the highest heating rate as indicated by the temperature contours on the fillet surface moved up with Mach number, so that for the highest Mach number, figure 29(c), the highest rate was around plugs 3 and 4. This result was consistent with the results shown in figures 25-28.

Heat Flux on Wing

While the grid on the wing was not made as fine as that over the fillet, an approximate assessment of the capability of the F3D code can still be made for the measured data in that region. In figure 30(a), the grid on the lower surface of the wing from the sm2 grid is shown, along with lines indicating the locations of thermocouples under the TPS material. As for the previous comparisons, the calculated heat flux from the CFD analysis would be expected to be higher than the value deduced from the surface temperature measurements because of the omission of the heat of ablation at the higher Mach numbers and the transient nature of the temperature at $M = 3.1$. However, certain trends still appear to be consistent. The data presented in reference 1 indicated that because the temperature increased more rapidly on the thermocouples near the root leading edge, the convective heat flux increased toward that corner. In addition, for points away from the root leading edge, the heat flux would appear not to vary greatly since the temperature increases at the same rate for all the thermocouples on the horizontal wing surfaces. This was also reflected in the calculated results. Along grid line 16, the heat flux decreased gradually from ahead of the wing to the trailing edge (fig. 30(b)). Along line 14, the flux was significantly higher near the root leading edge and then decreased to values only slightly higher than those on line 16. The estimated heat flux from the measured temperatures at two points on the inboard row of sensors is included in figure 30(b).

CONCLUDING REMARKS

An analysis was conducted of aerothermodynamic measurements from the first flight of Pegasus to validate the Navier-Stokes computer code F3D. The results achieved confirm that the F3D code can accurately predict the heat transfer on a vehicle such as Pegasus for preflight-design purposes.

An important aspect of any computational fluid dynamic analysis is grid generation. In this study, grids of various densities and point distributions provided evidence of the effect of the grid on calculated flow fields. The use of a coarse grid provided the advantage of fast convergence and allowed many tests in a short time. The coarse grid resulted in only slight loss in accuracy regarding the boundary layer but was not adequate for resolving shock waves. Good results can be obtained for engineering purposes by adapting the grid to put a fine mesh where needed, while keeping the number of grid points low to increase running speed.

Flight measurements of temperature and heat transfer on a vehicle like Pegasus require careful analysis and interpretation. Heat-flux gauges placed in a surface that is ablating can be very precise in their measurement, but give a meaningless value unless other data are available to identify the exact conditions in the flow over the gauge. In this analysis, an attempt was made to supplement the high-temperature reusable surface insulation heat-flux gauge data with estimates of the heat flux to the surrounding thermal protection system material. An exact analysis was impossible because of the lack of precise data on the conditions on the ablative surface. There was also some uncertainty regarding the properties of the thermal protection system materials. The estimated heat flux was lower than the results calculated by the computational fluid dynamic code, but consistent with the assumptions and locations of important flow features, such as the wing leading-edge shock wave. The approximation of the wall temperature as a constant equal to the ablation temperature of a protective coating (except at specific points where the temperature is measured on a ceramic plug) is a reasonable representation of the experimental situation.

As a preflight-design tool, the F3D code produces accurate predictions of the heat transfer, and it can provide detailed data for assessment of boundary layer separation, shock waves, and vortex formation. As a postflight-analysis tool, the code provides a way to clarify and interpret the measured results.

REFERENCES

1. Noffz, G., R.E. Curry, E. Haering, Jr., and P. Kolodziej, *Aerothermal Test Results from the First Flight of the Pegasus Air-Launched Space Booster*, NASA TM-4330, 1990.

2. Neumann, R.D., P.J. Erbland, and L.O. Kretz, "Instrumentation of Hypersonic Structures: A Review of Past Applications and Needs of the Future," AIAA-88-2612, June 1988.

3. Ying, S.X., J.L. Steger, and L.B. Schiff, "Numerical Simulation of Unsteady, Viscous, High Angle-of-Attack Flows Using a Partially Flux-Split Algorithm," AIAA-86-2179, August 1986.

4. Buning, P.G., I.T. Chiu, S. Obayashi, Y.M. Rizk, and J.L. Steger, "Numerical Simulation of the Integrated Space Shuttle Vehicle in Ascent," AIAA-88-4359, August 1988.

5. Rizk, Y.M., J.L. Steger, and D. Chausee, *Use of a Hyperbolic Grid Generation Scheme in Simulating Supersonic Viscous Flow About Three-Dimensional Winged Configurations*, NASA TM-86776, 1985.

6. Klopfer, G. H., "Solution Adaptive Meshes with a Hyperbolic Grid Generator," in 2nd International Conference on Numerical Grid Generation in Computational Fluid Dynamics, Dec. 1988, Miami Beach, FL, Published by Pineridge Press, Mumbles, Swansea, UK, pp. 443-454.

7. U. S. Standard Atmosphere, National Oceanic and Atmospheric Administration, 1976.

8. Hsieh, T., "Calculations of Flowfields About Indented Nosetips," NSWC TR-82-286, Naval Surface Warfare Center, Dahlgren VA, August 1982.

TABLES

Table 1. Free stream and other conditions for CFD calculations.

Case	M_∞	α	Re	T_∞ (°F)	T_w (°F)
1	3.1	7.5	$6.463(10^6)$	−68.8	135
2	4.0	4.0	$2.855(10^6)$	−55.9	225
3	5.0	0.5	$1.075(10^6)$	−34.0	250

Table 2. Heat-transfer rate on wing fillet for $M_\infty = 5$, $\alpha = 0.5°$ (sml grid).

Point		q(Btu/ft^2 sec)		
I	J	$\alpha = 0.5.0°$	$\alpha = 1.5°$	% Change
37	26	0.514295	0.530128	−3.0
33	27	0.876573	0.843007	+3.8
32	27	0.884289	0.836098	+5.5
37	28	0.793589	0.759780	+4.2
33	30	0.682396	0.619340	+9.2
32	30	0.637447	0.562254	+7.5
38	32	0.925851	0.898511	+2.9
37	32	0.779837	0.752663	+3.5
33	32	0.589492	0.533798	+9.4

Table 3. Measured heat flux on fillet at HRSI plugs.

Point number	X/D	Z/D	q(Btu/ft^2 sec)		
			$M = 3.1$	$M = 4.0$	$M = 5.0$
2	7.146	0.459	0.75	0.78	0.60
3	6.597	0.459	0.65	0.75	0.83
4	6.441	0.459	0.70	0.80	0.95
5	7.146	0.359	0.55	0.65	0.70
6	6.597	0.339	0.52	0.60	0.60
7	6.441	0.339	0.50	0.60	0.58
8	7.388	0.220	0.60	0.65	0.60
9	7.146	0.220	0.60	0.78	1.00
10	6.597	0.220	0.50	0.56	0.50

FIGURES

PAYLOAD
AND
3RD STAGE

2ND
STAGE

1ST STAGE

Figure 1. Pegasus.

Launch
t=0 sec
h=40,000 ft
M=0.80

First Stage Burnout
t=81.8 sec
h = 199,000 ft
M=8.1

Second Stage Burnout
t=160 sec
h=556,000 ft
v=17,500 fps
γ=19.4

Second Stage/Third Stage Coast

Third Stage Ignition
t=466 sec
h=248 nmi
v=15,800 fps
γ=2.0

Third Stage Burnout and Orbital Insertion
t=531.5 sec
h=250 nmi
v=25,043.2 fps
γ=0.0

Payload Fairing Separation
t=124 sec
h=369,000 ft
v=11,900 fps

Second Stage Ignition
t=85.3 sec
h=213,000 ft
γ=27.0

Max q̄
1000 psf

2.5 g Pull up

First Stage Ignition
t=5 sec
h=39,700 ft

Aerodynamic Attitude Control (Fins)

TVC Attitude Control (Pitch & Yaw)
Cold Gas RCS (Roll)

Figure 2. Pegasus baseline mission profile.
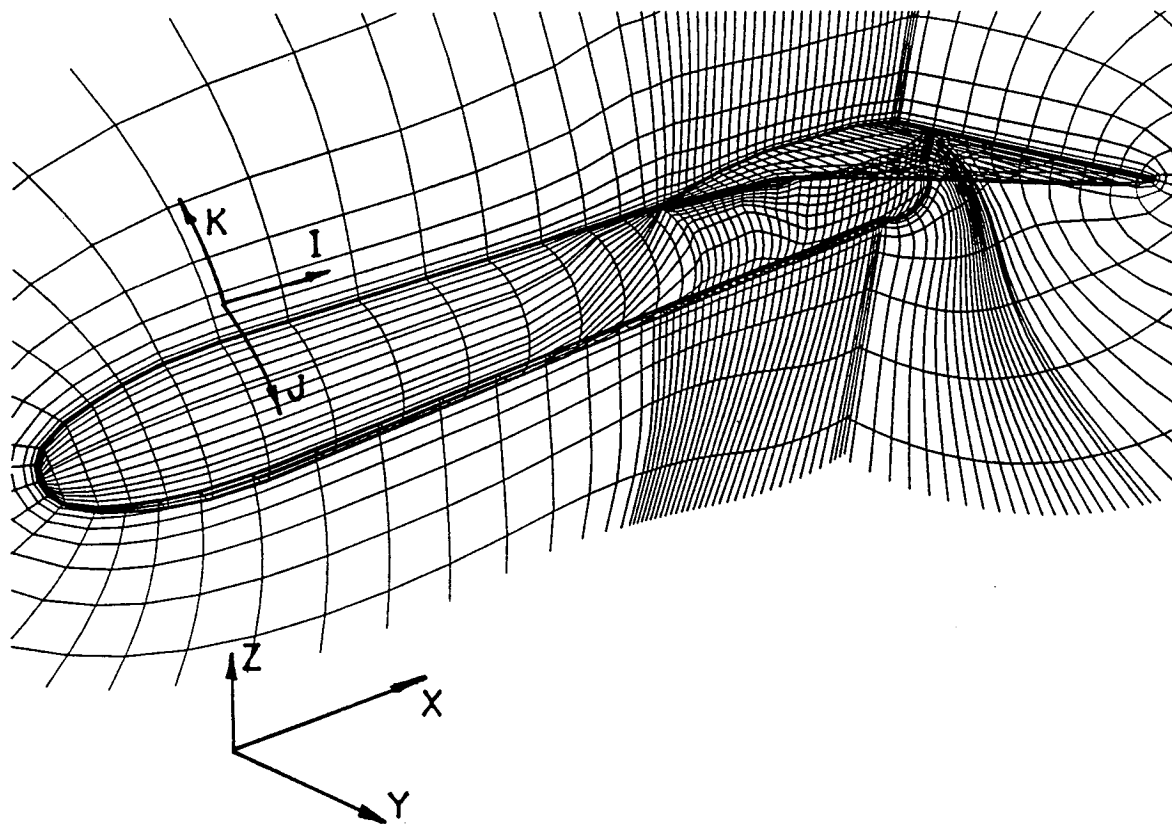
(a) Perspective view.

Figure 3. Views of portions of fine grid on Pegasus nose and wing.
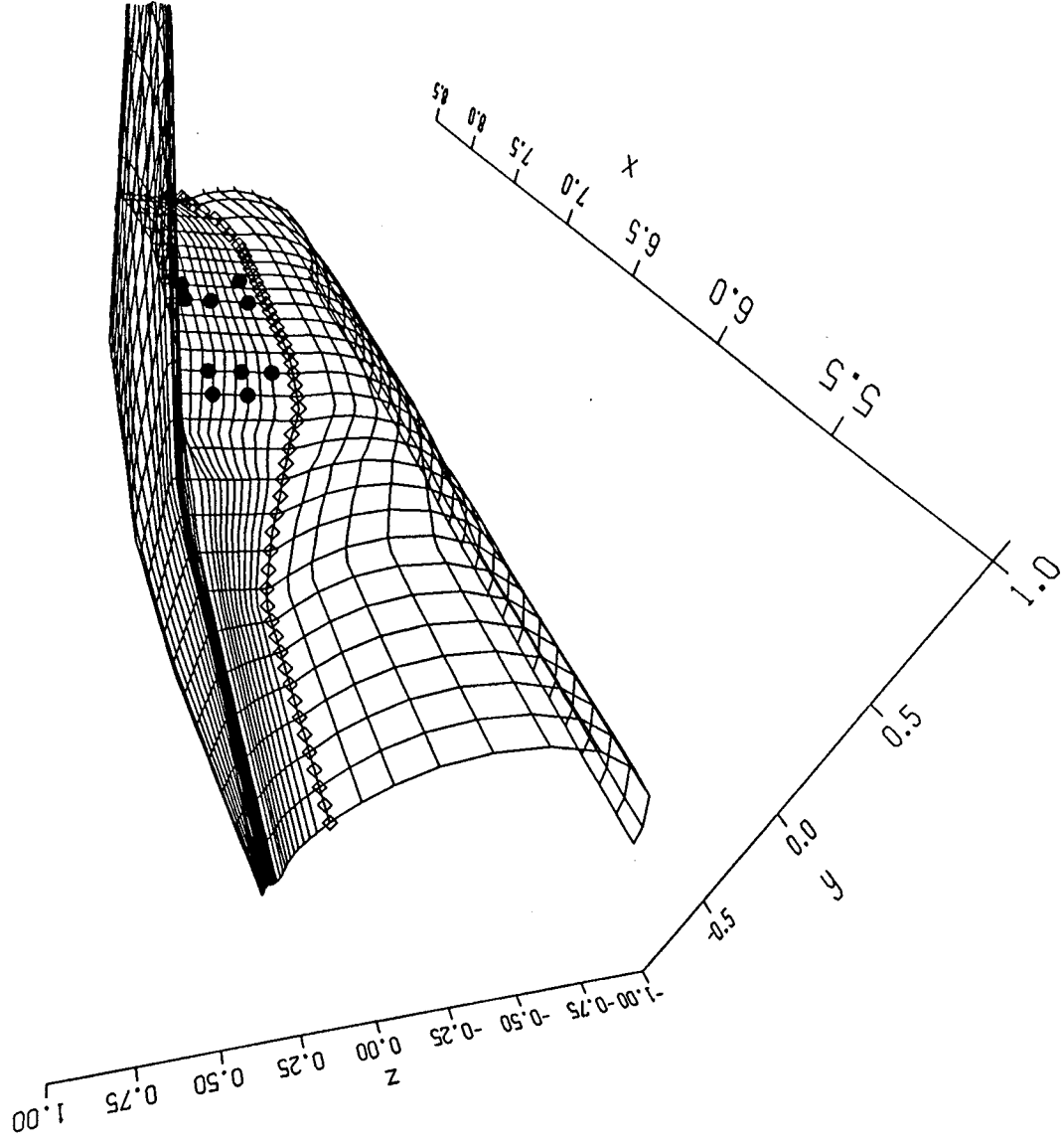
(b) Close-up perspective view of wing and fillet.

Figure 3. Continued.
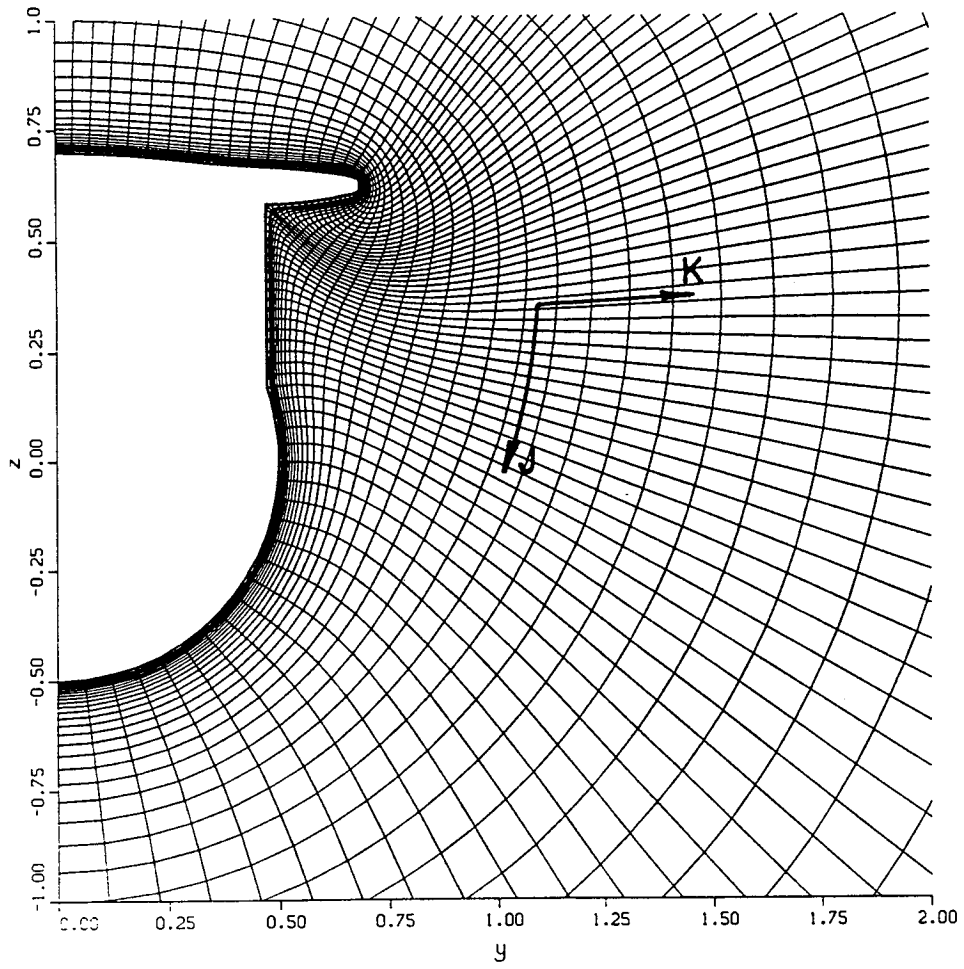
(c) Cross section at X/D = 6.25.

Figure 3. Continued.
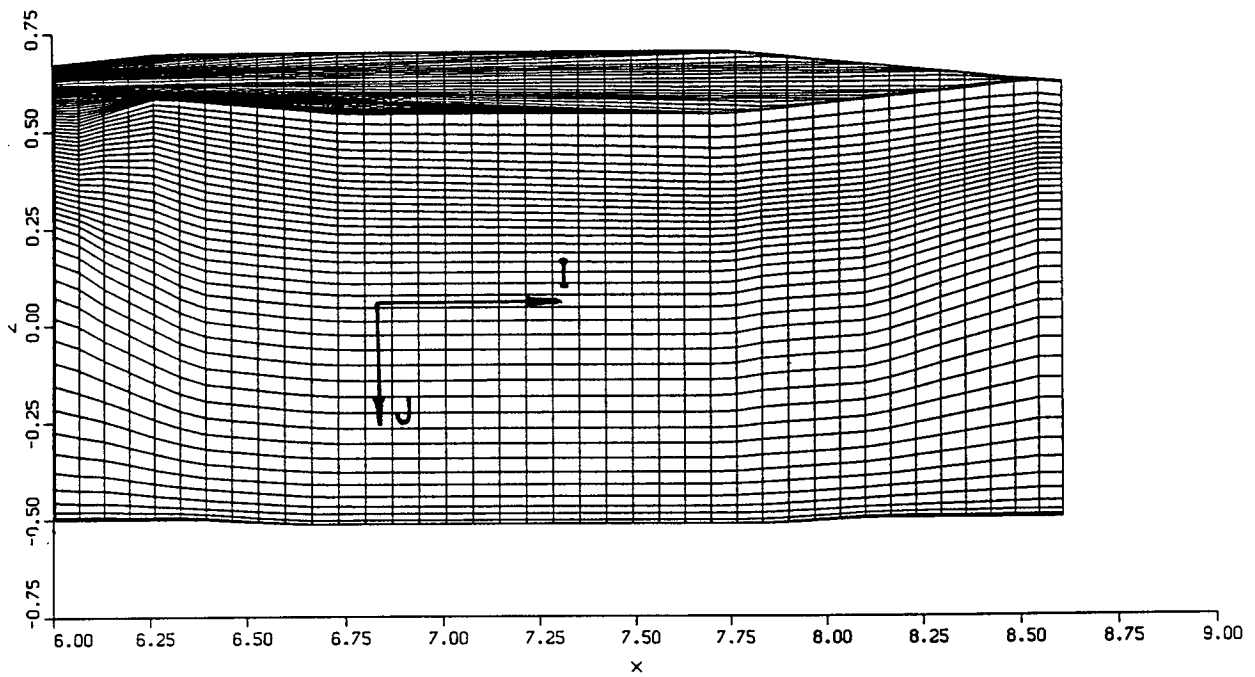
(d) Side view of wing and fillet.

Figure 3. Concluded.
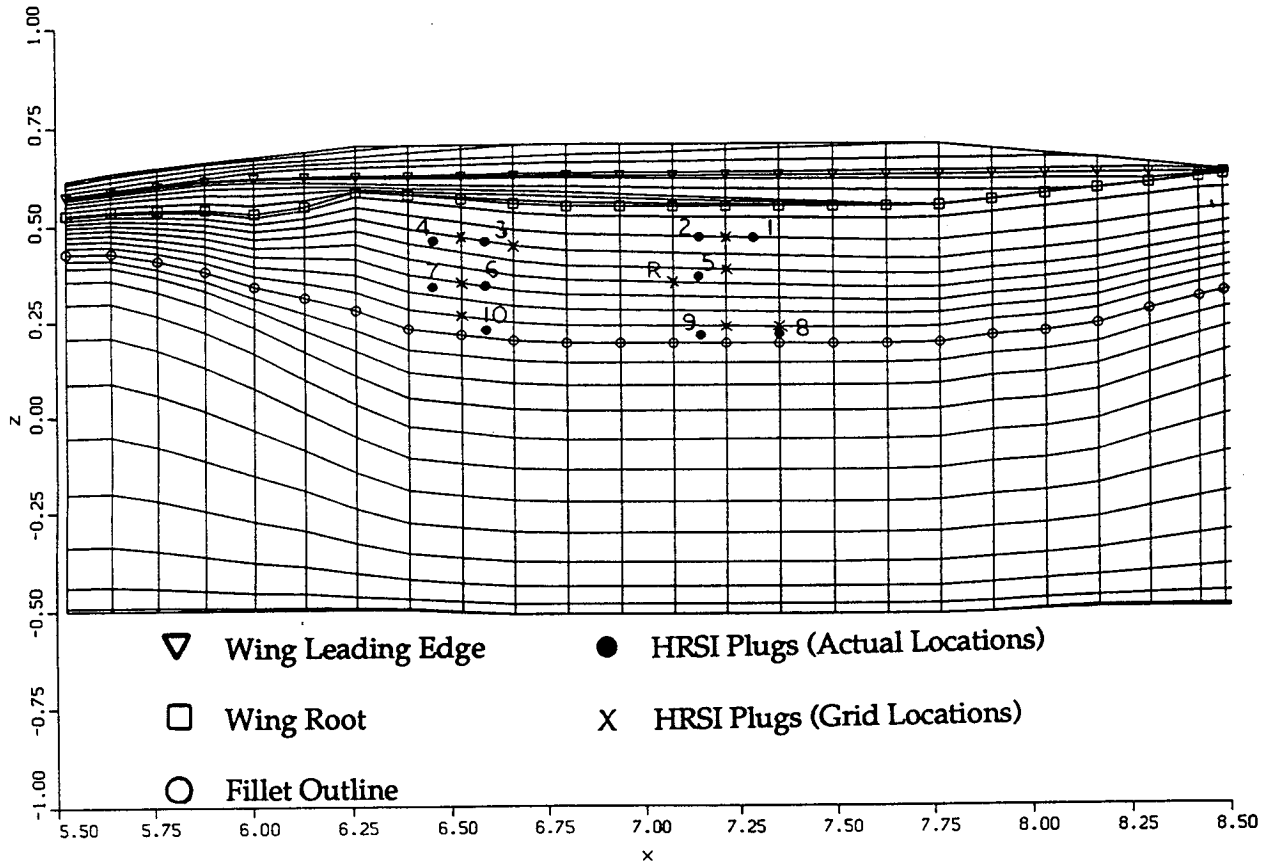
(a) Side view of wing and fillet.

Figure 4. First coarse grid subset of fine grid (sml grid).
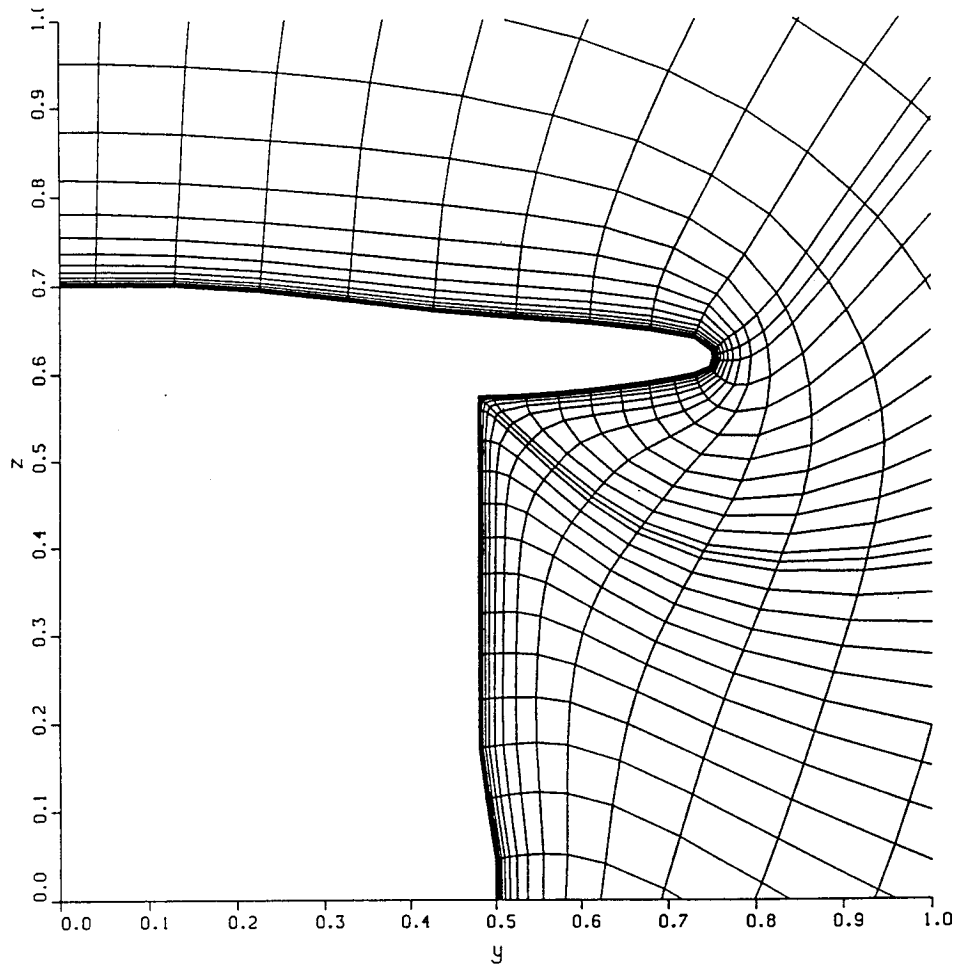
(b) Cross section at X/D = 6.25.

Figure 4. Concluded.
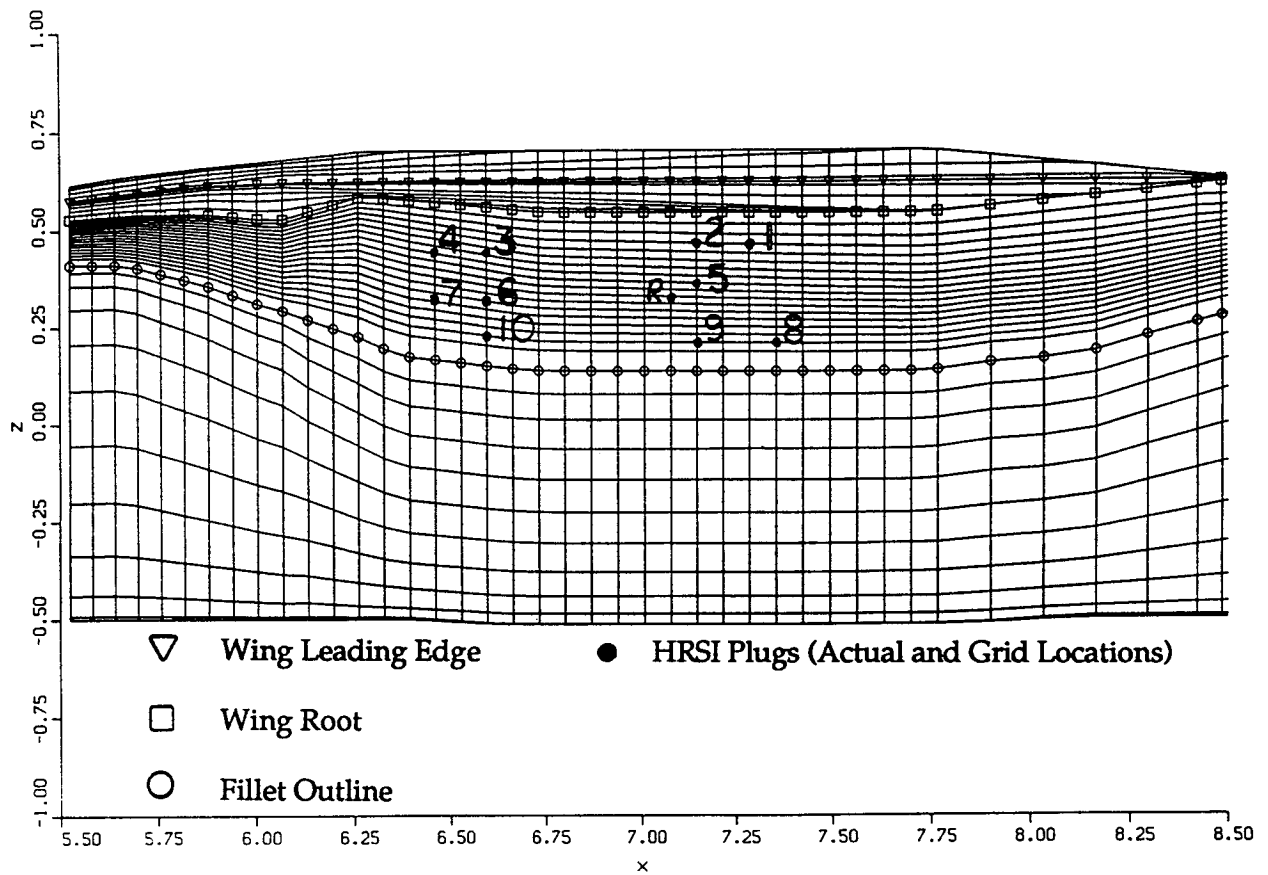
(a) Side view of wing and fillet.

Figure 5. Intermediate grid (mm grid).
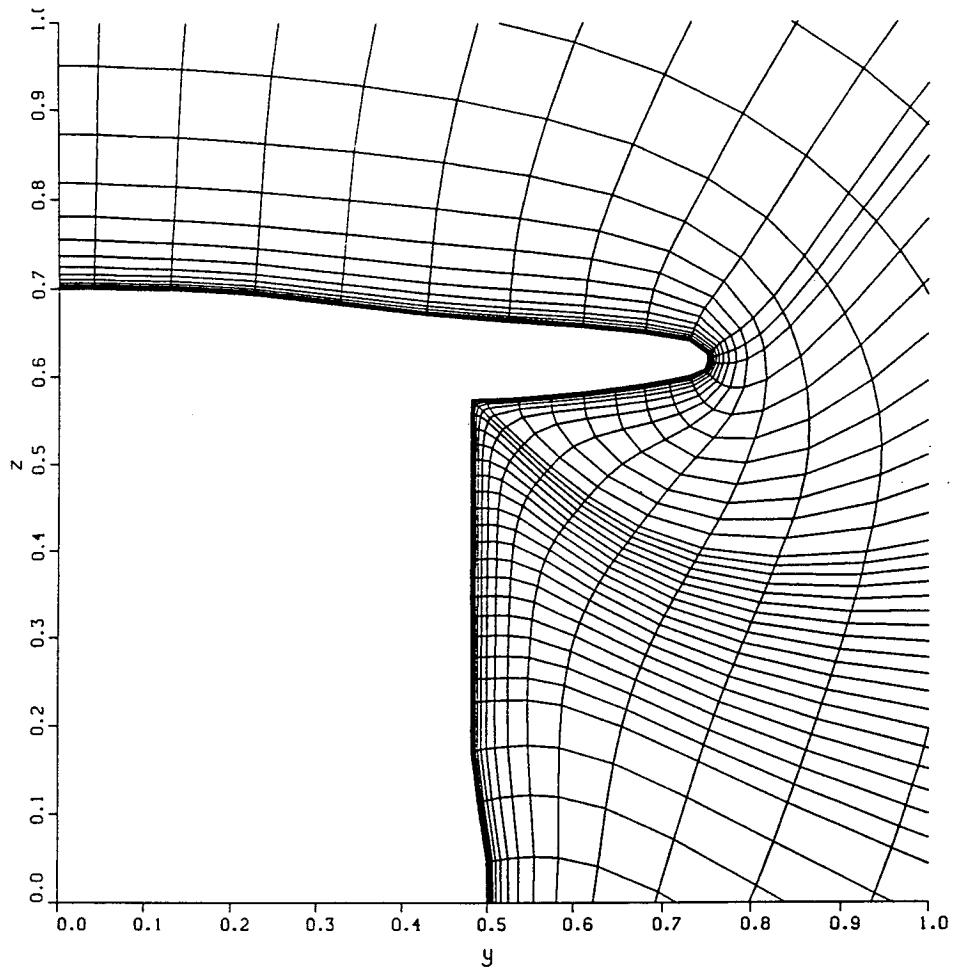
(b) Cross section at X/D = 6.25.

Figure 5. Concluded.
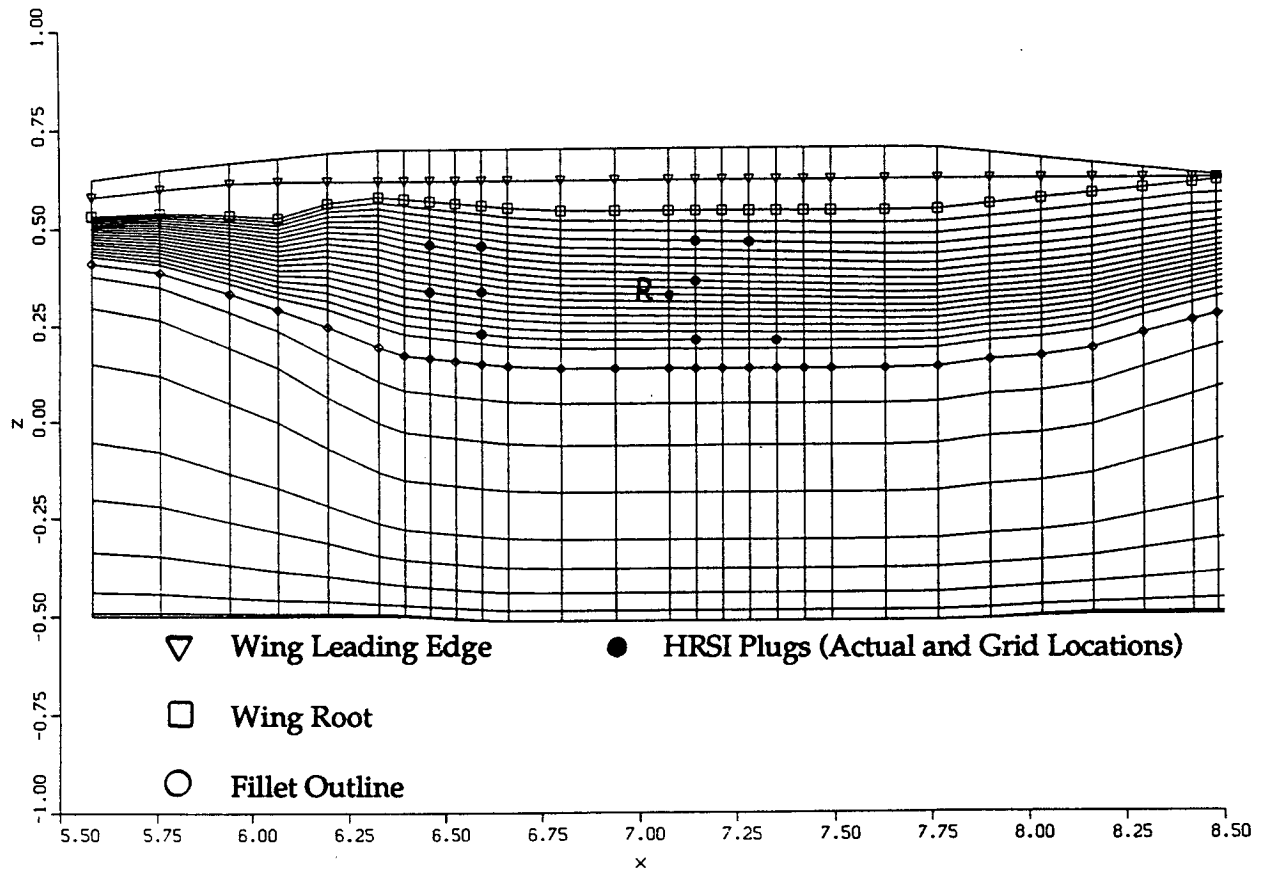
(a) Side view of wing and fillet.

Figure 6. Second coarse grid (sm2 grid).
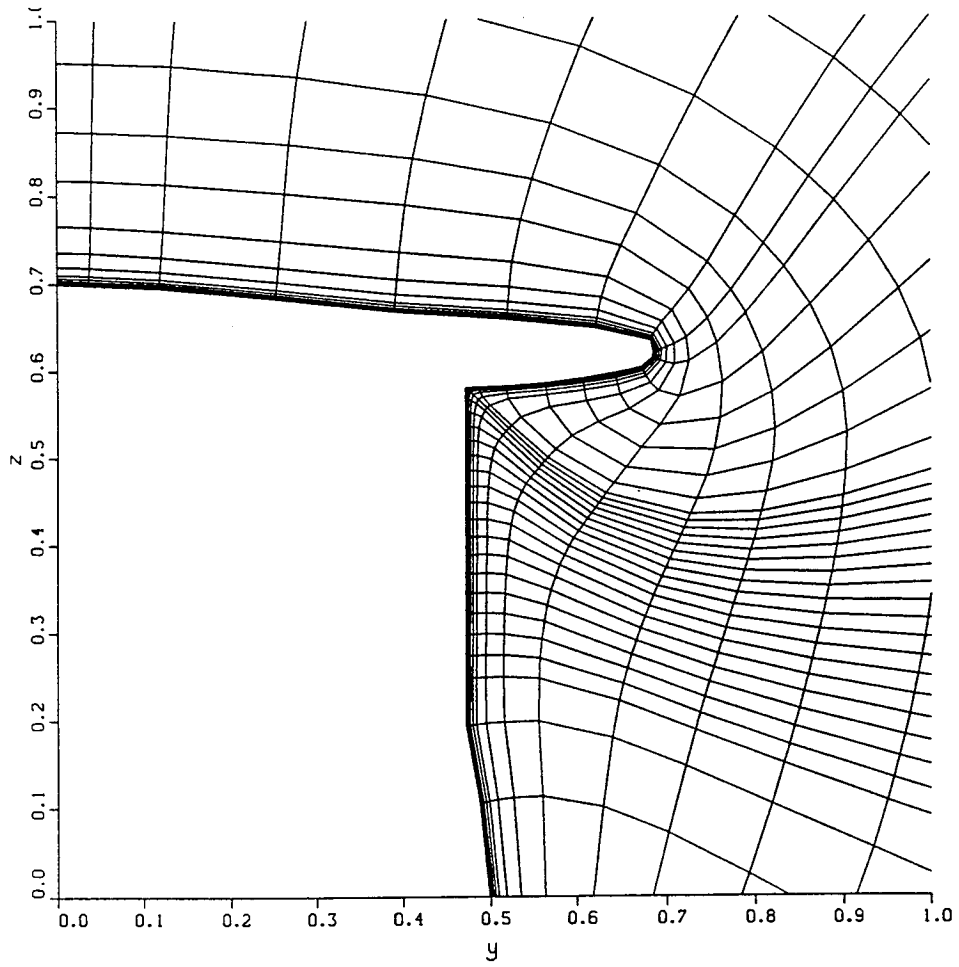
(b) Cross section at X/D = 6.25.

Figure 6. Concluded.

34

PEGASUS FLIGHT 1
FIRST STAGE FREESTREAM AIRDATA
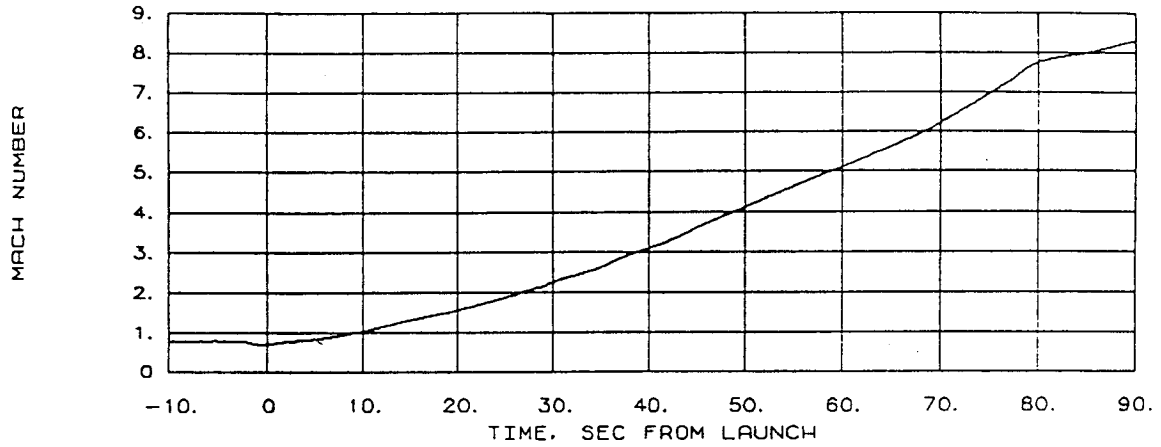
(a) Free-stream Mach number.
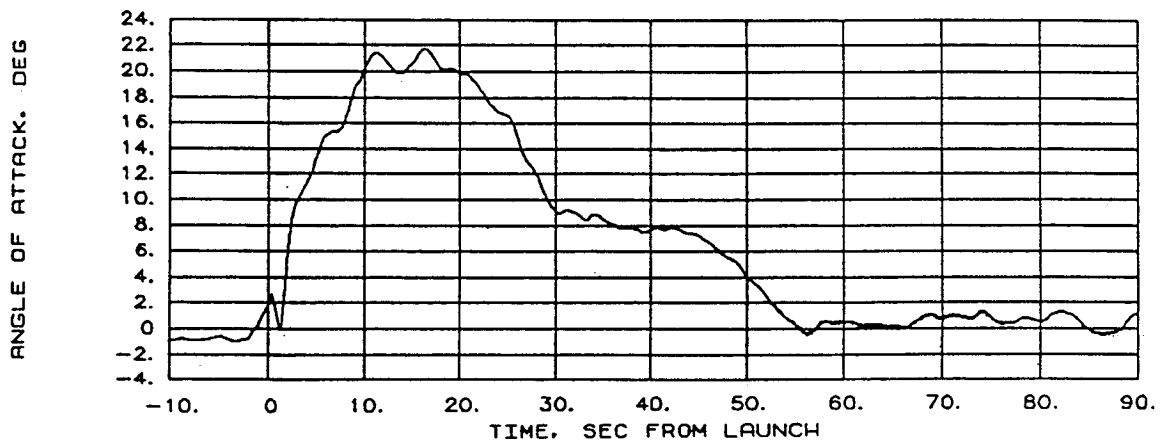
(b) Angle of attack.

Figure 7. Mach number, angle of attack, and surface temperature from flight data.

35

X/D = 6.8006

X/D = 6.9384
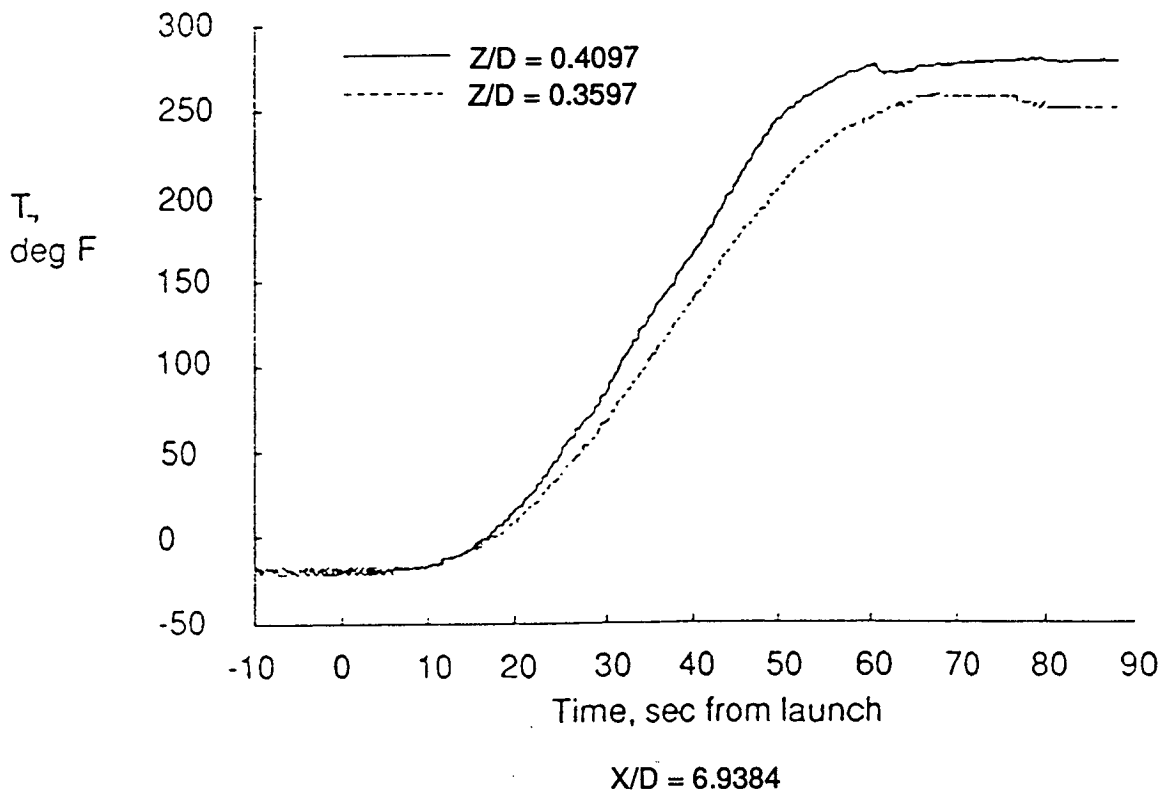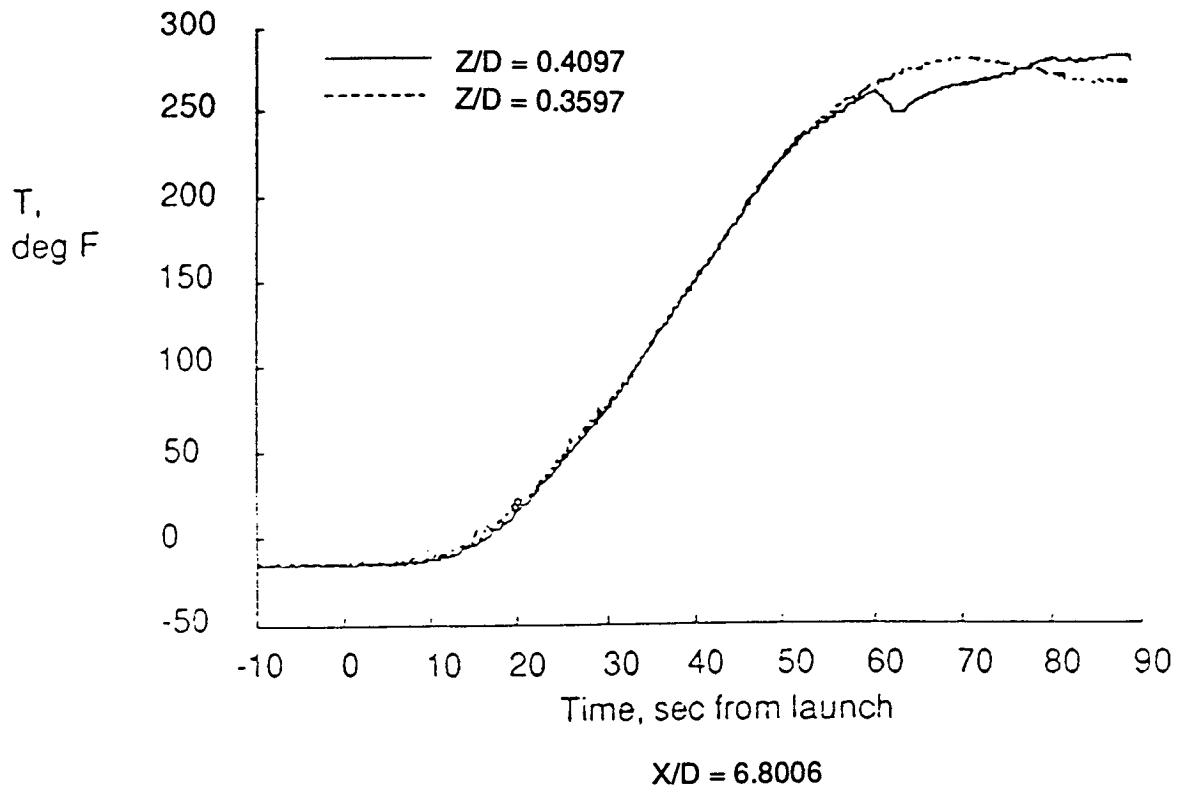
(c) Fillet sidewall temperature at the Thermolag/cork interface.

Figure 7. Concluded.
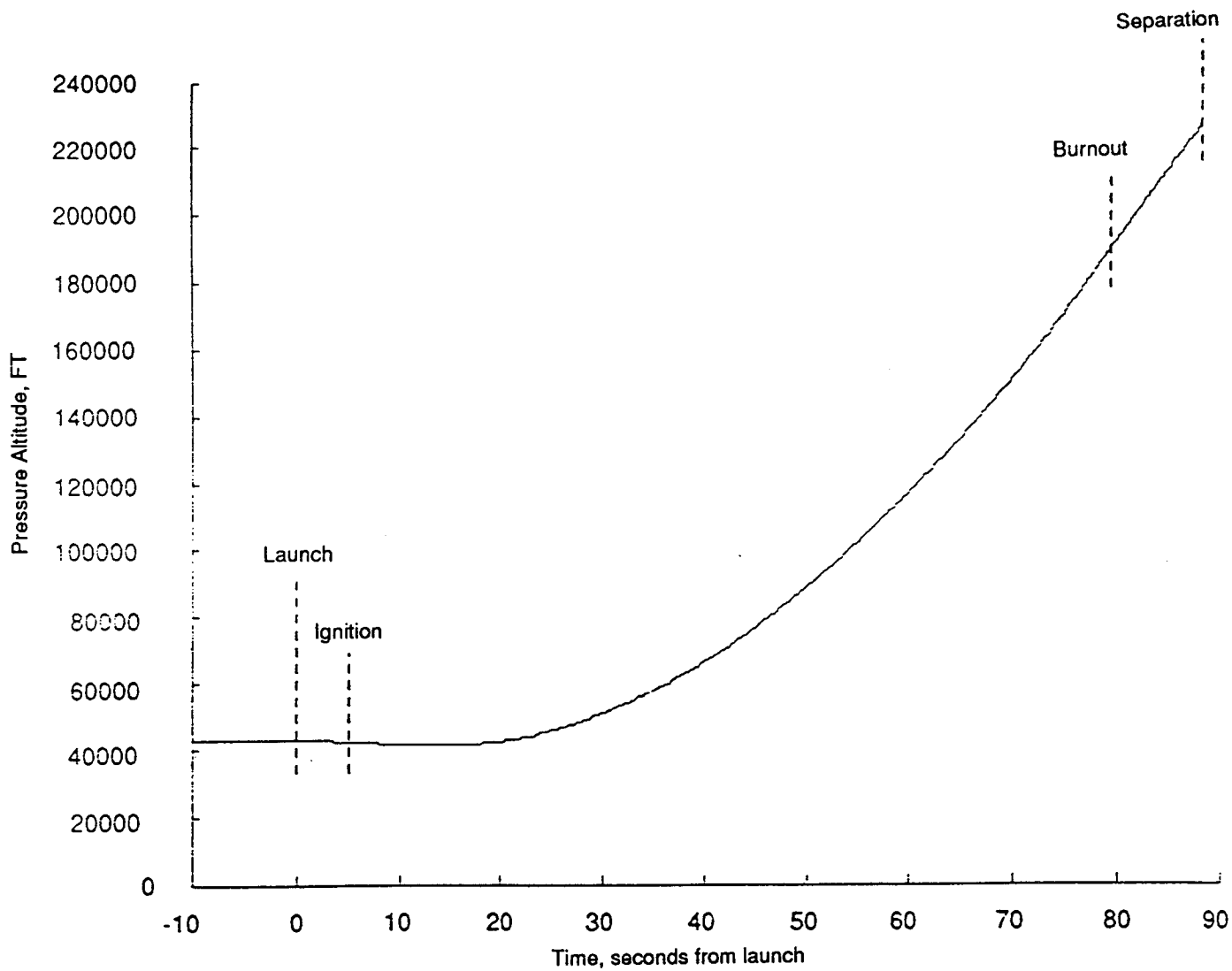
Figure 8. Pressure altitude from flight data.
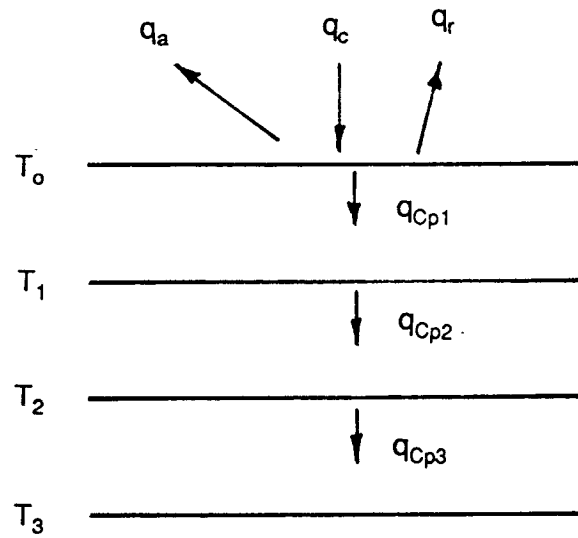
Figure 9. Heat transfer model of TPS.
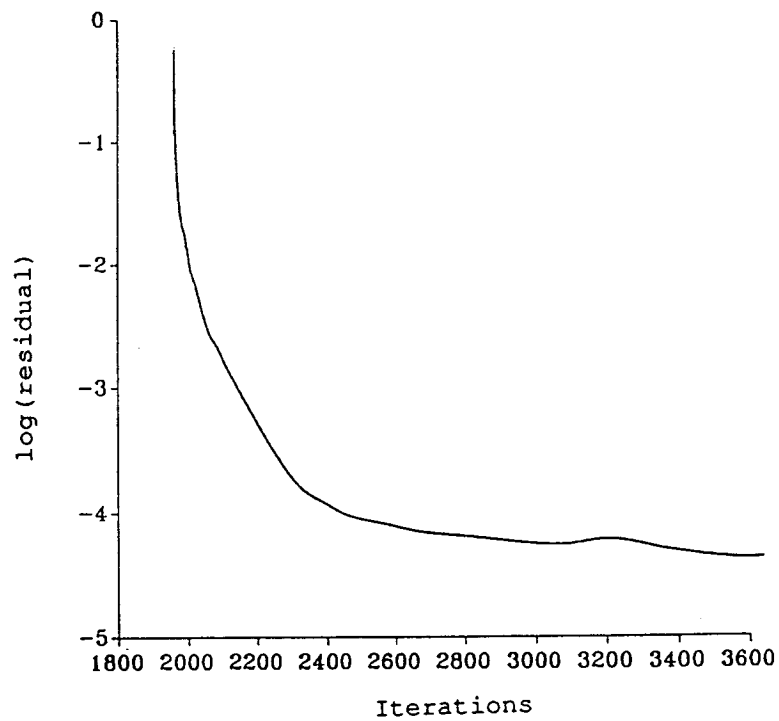
(a) $M_\infty = 4.0$, $\alpha = 4.0°$
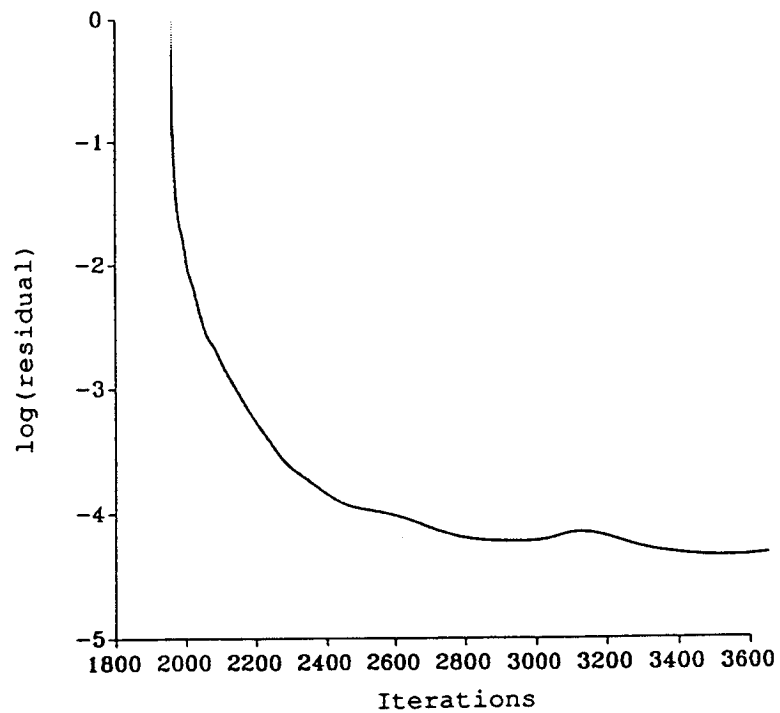
(b) $M_\infty = 5.0$, $\alpha = 0.5°$

Figure 10. History of solution residuals for constant T_w during initial phase of calculations after restart from $M_\infty = 5.0$, $\alpha = 5.0°$ (warm start).
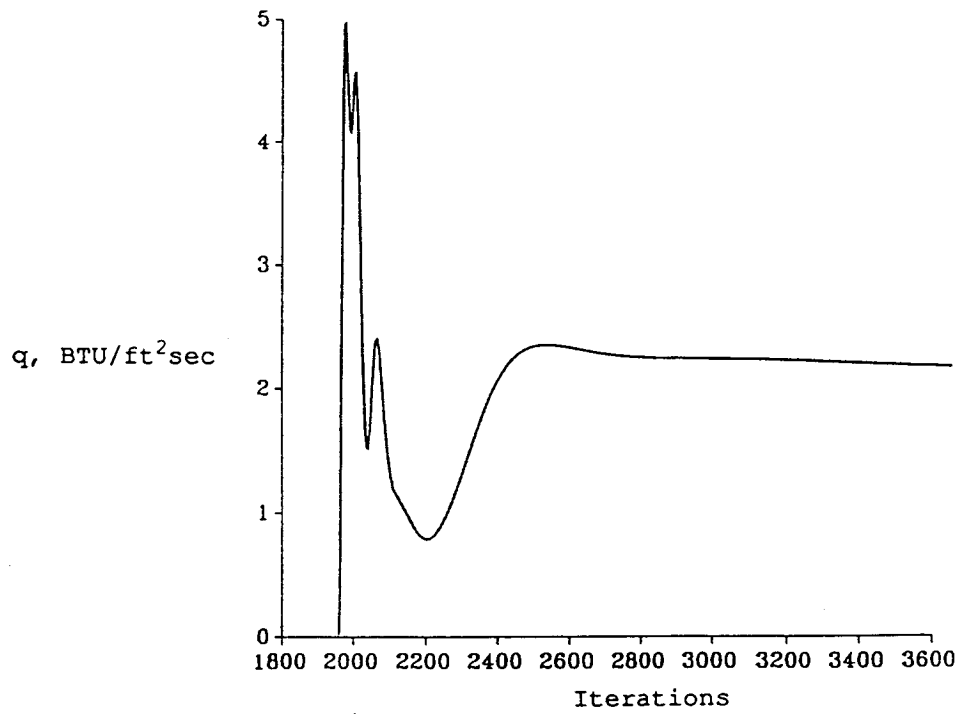
(a) $M_\infty = 4.0$, $\alpha = 4.0°$
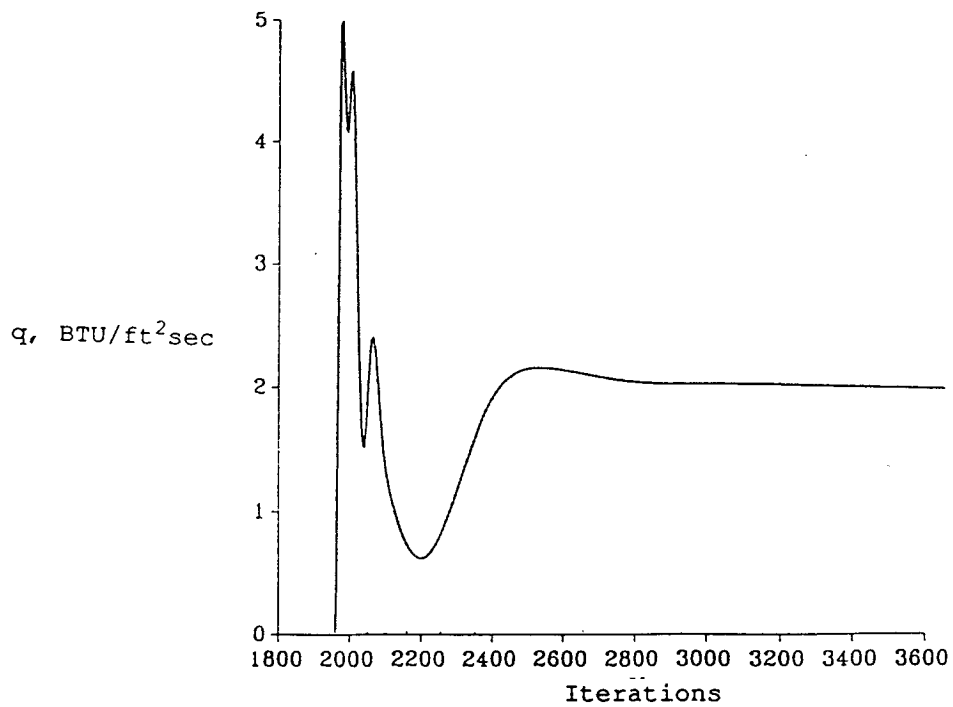
(b) $M_\infty = 5.0$, $\alpha = 0.5°$

Figure 11. Heat flux at the reference point for constant T_w and initial part of warm start calculation.
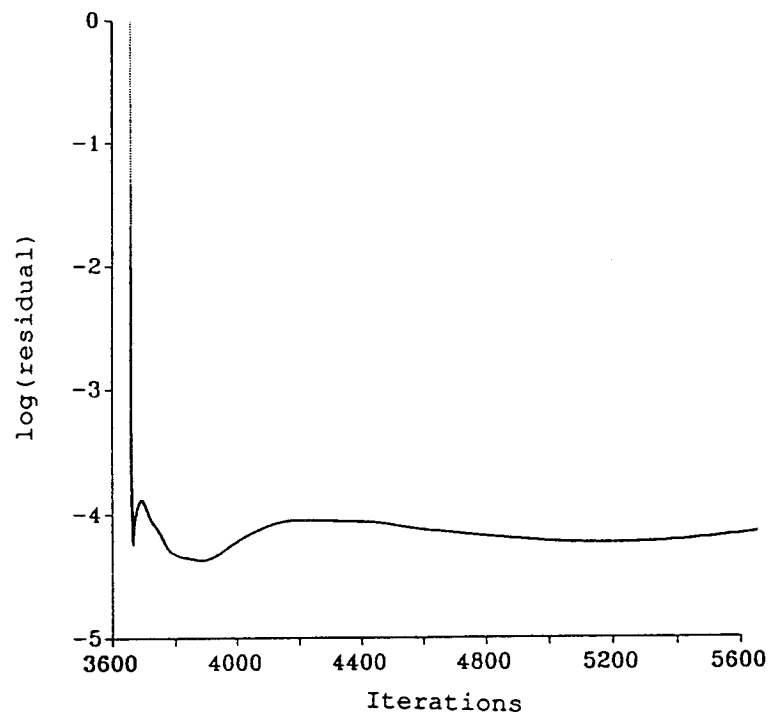
(a) $M_\infty = 4.0$, $\alpha = 4.0°$
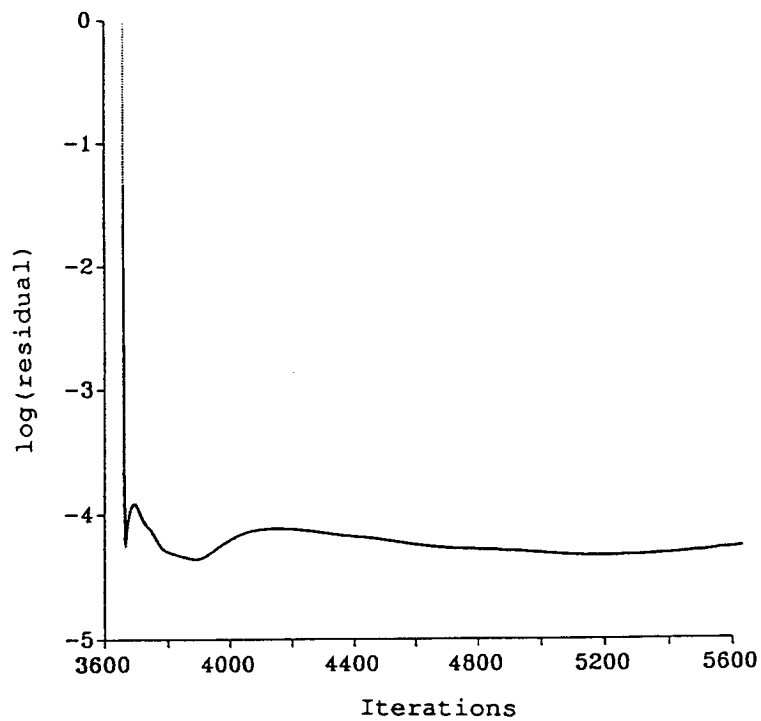
(b) $M_\infty = 5.0$, $\alpha = 0.5°$

Figure 12. History of solution residuals for restarted solution during second phase of calculations after changing surface temperature to 250 °F with $T = 500$ °F at HRSI plug locations.
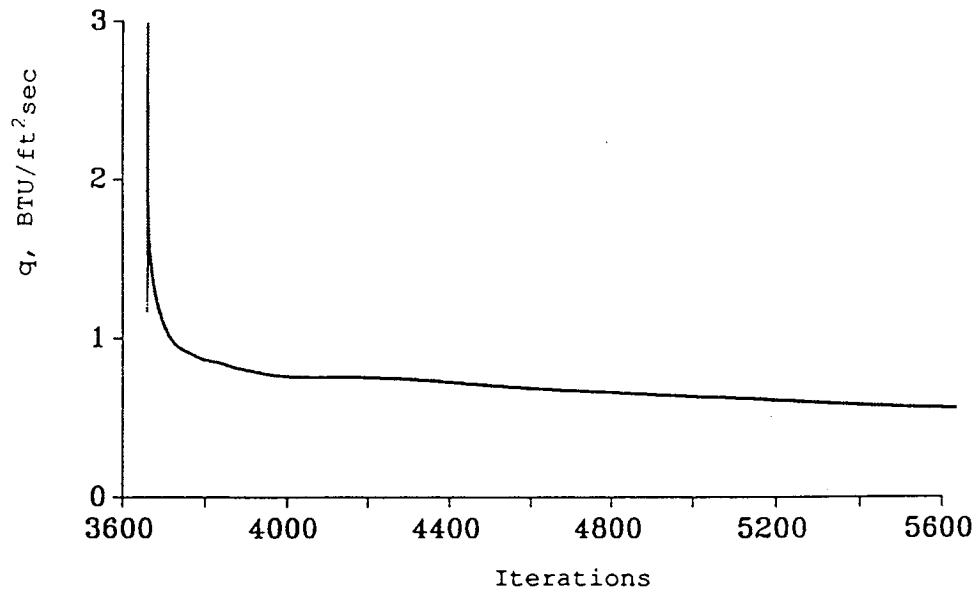
(a) $M_\infty = 4.0$, $\alpha = 4.0°$
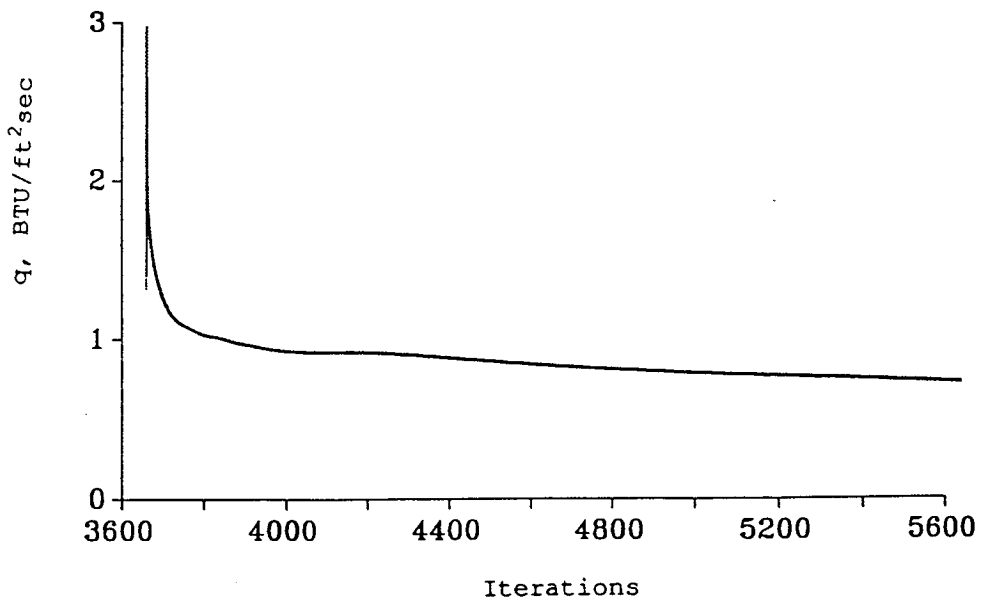
(b) $M_\infty = 5.0$, $\alpha = 0.5°$

Figure 13. History of heat flux at the reference point for restarted solution during second phase of calculations after changing surface temperature to 250 °F with $T = 500$ °F at HRSI plug locations.
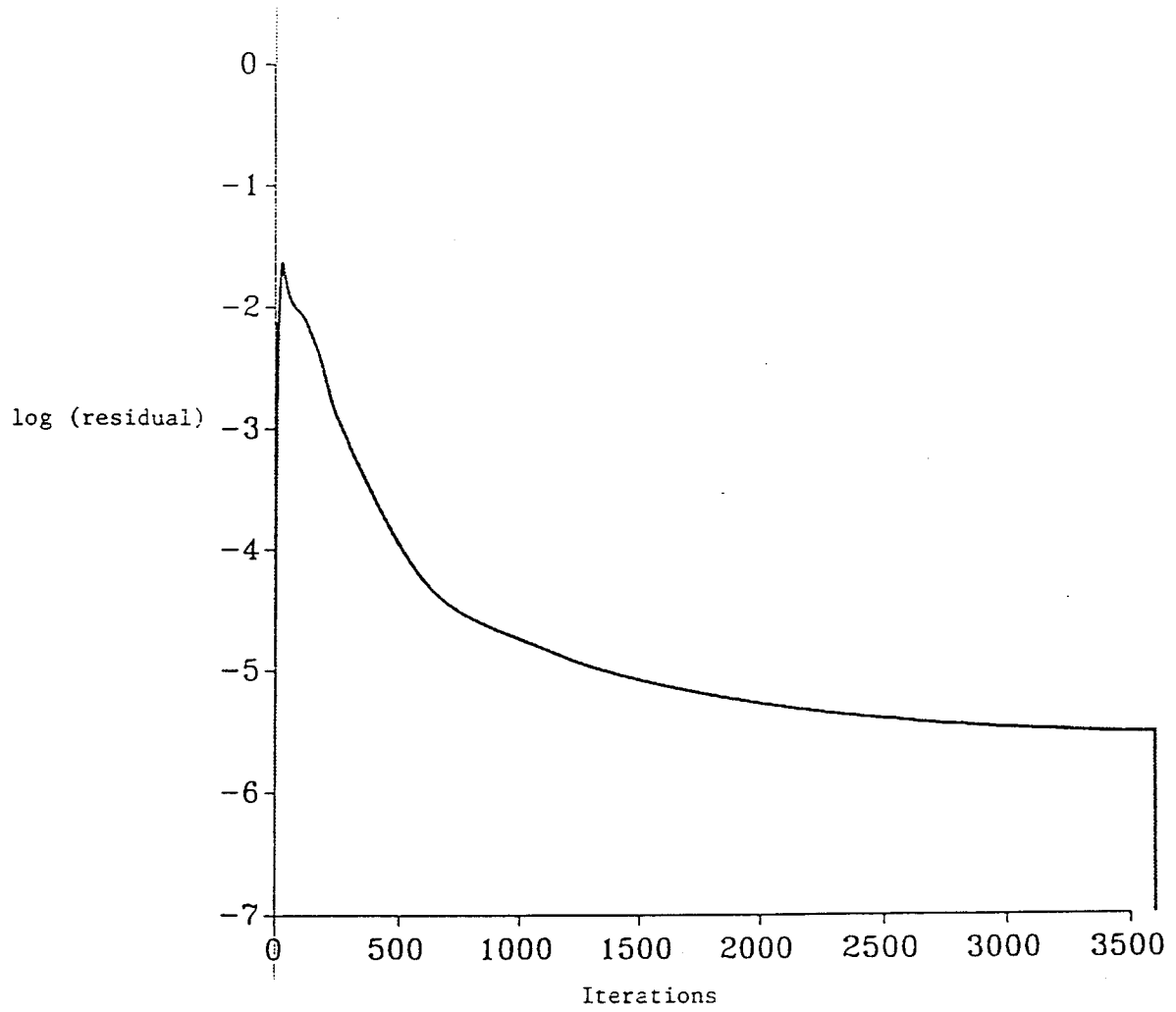
Figure 14. History of solution residuals, $M_\infty = 5.0, \alpha = 0.5°$, cold start.
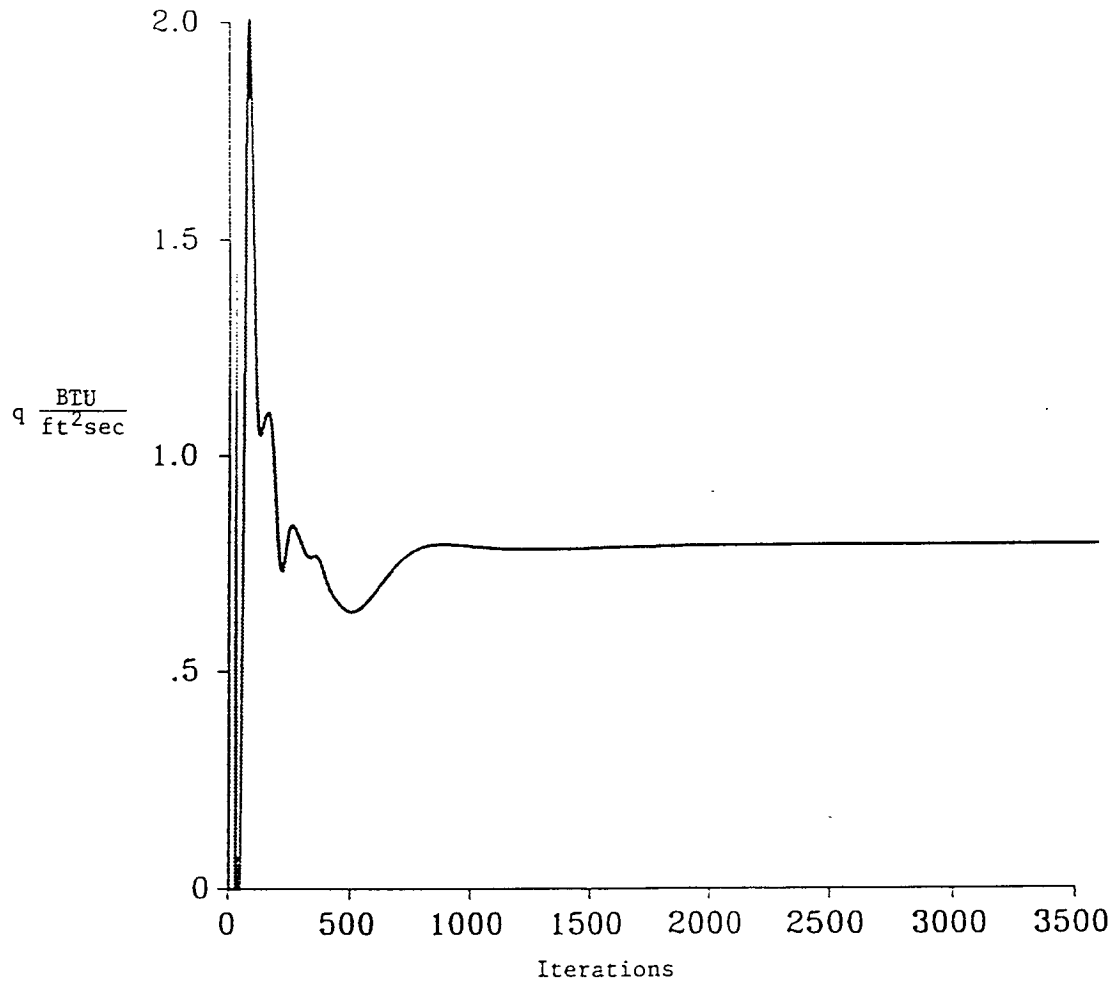
Figure 15. History of convective heat flux at reference point on fillet, $M_\infty = 5.0, \alpha = 0.5°$, cold start.
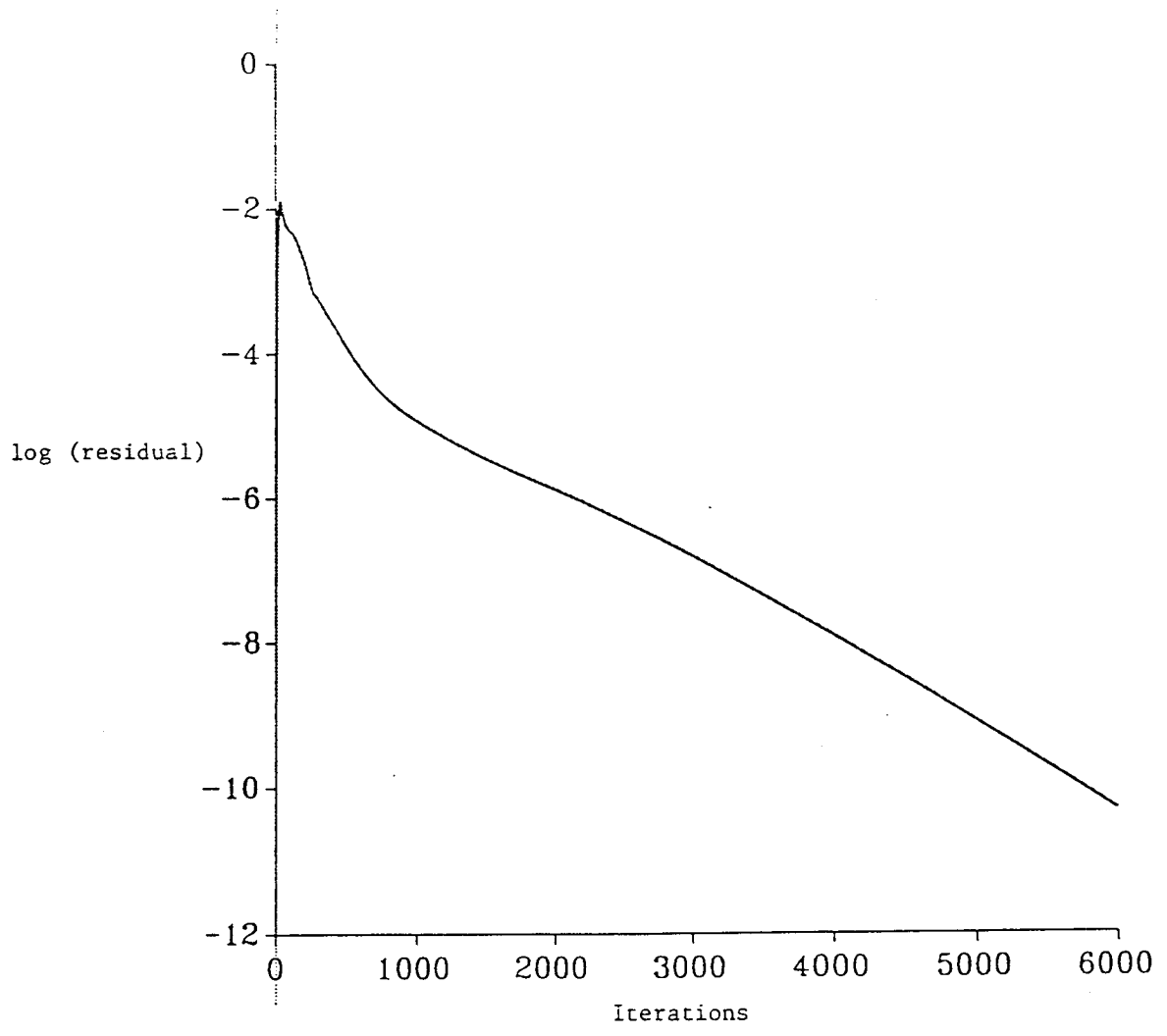
Figure 16. History of solution residuals, $M_\infty = 4.0, \alpha = 4.0°$, cold start.
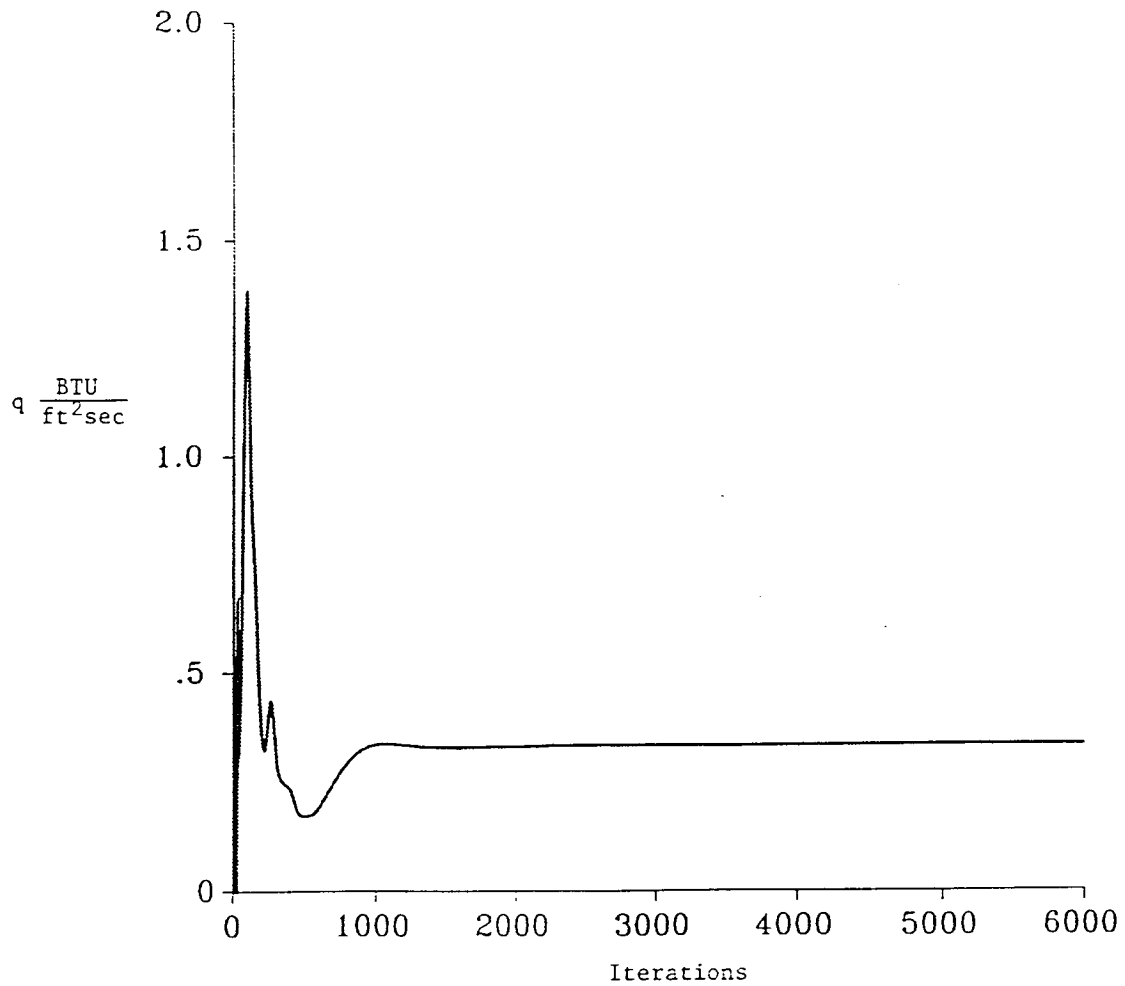
Figure 17. History of convective heat flux at reference point on fillet, $M_\infty = 4.0, \alpha = 4.0°$, cold start.
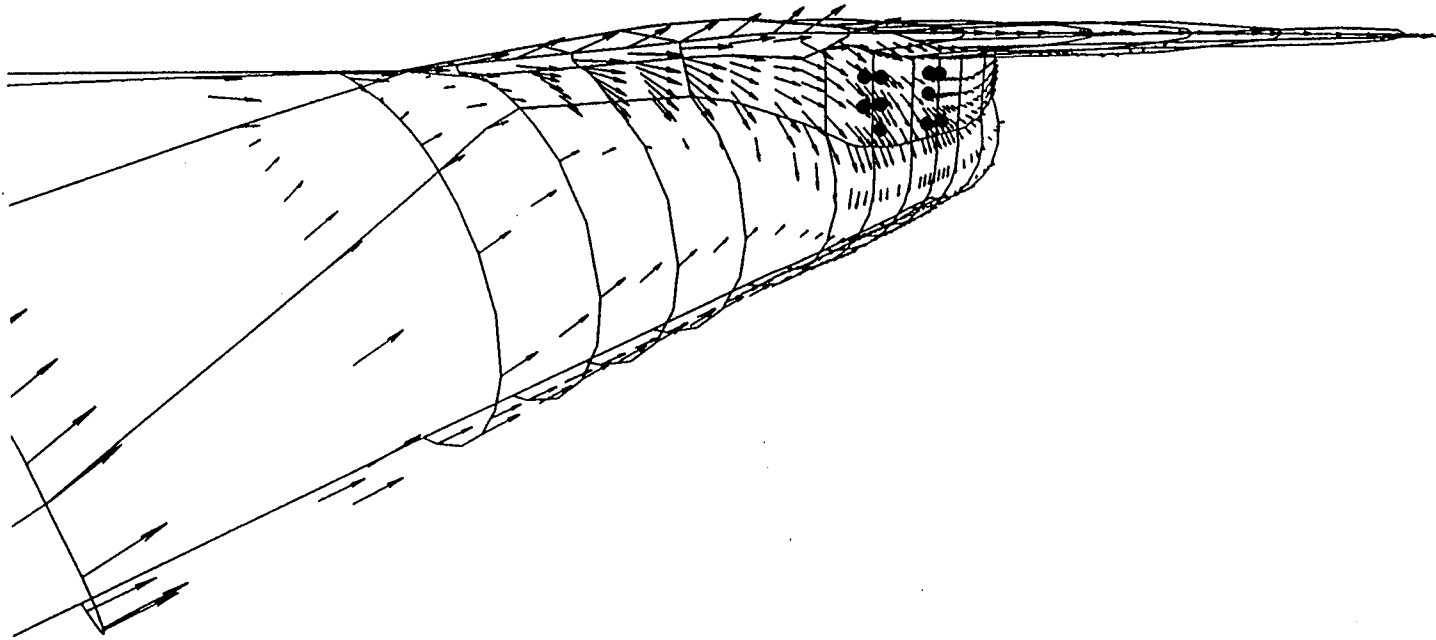
(a) $K = 2$.

Figure 18. Velocity vectors on body and wing for $M_\infty = 4.0, \alpha = 4.0°$.
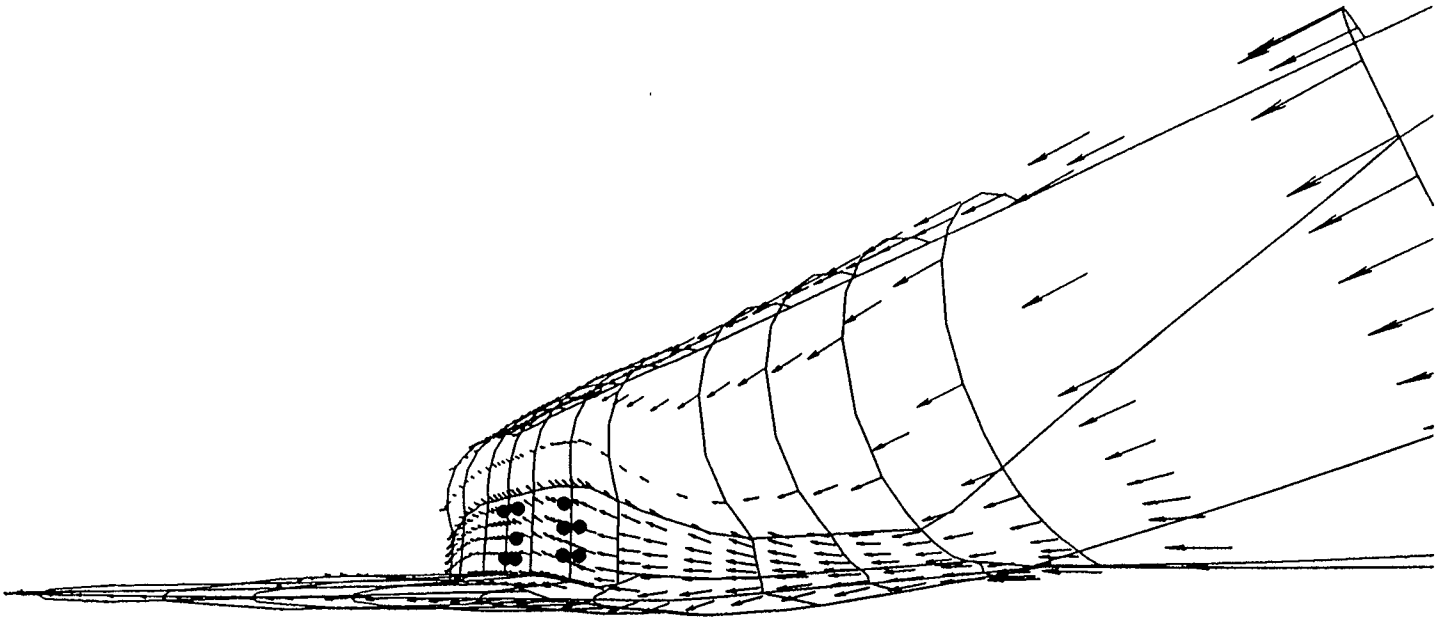
(b) $K = 7$.

Figure 18. Continued.
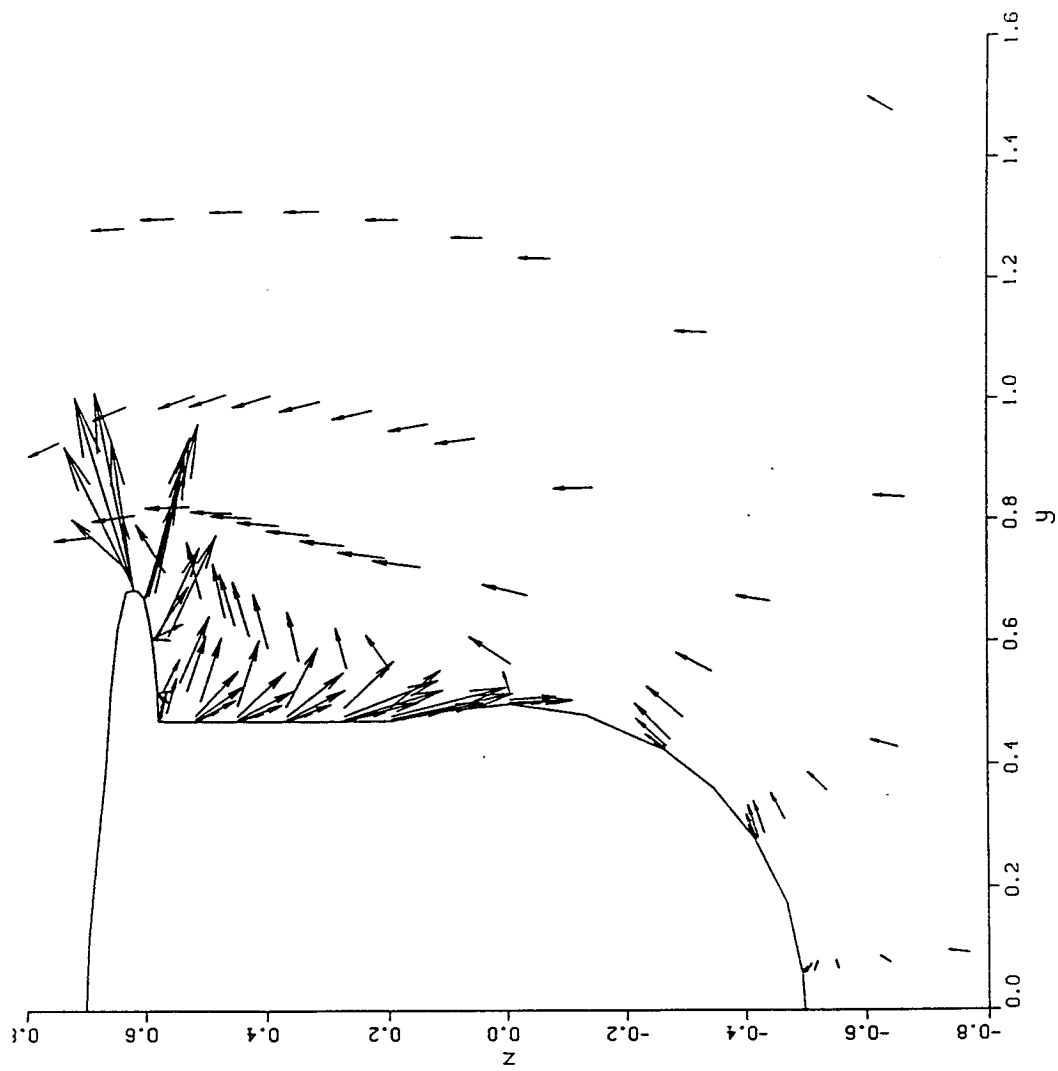
(c) Cross section at X/D = 6.25.

Figure 18. Concluded.

49
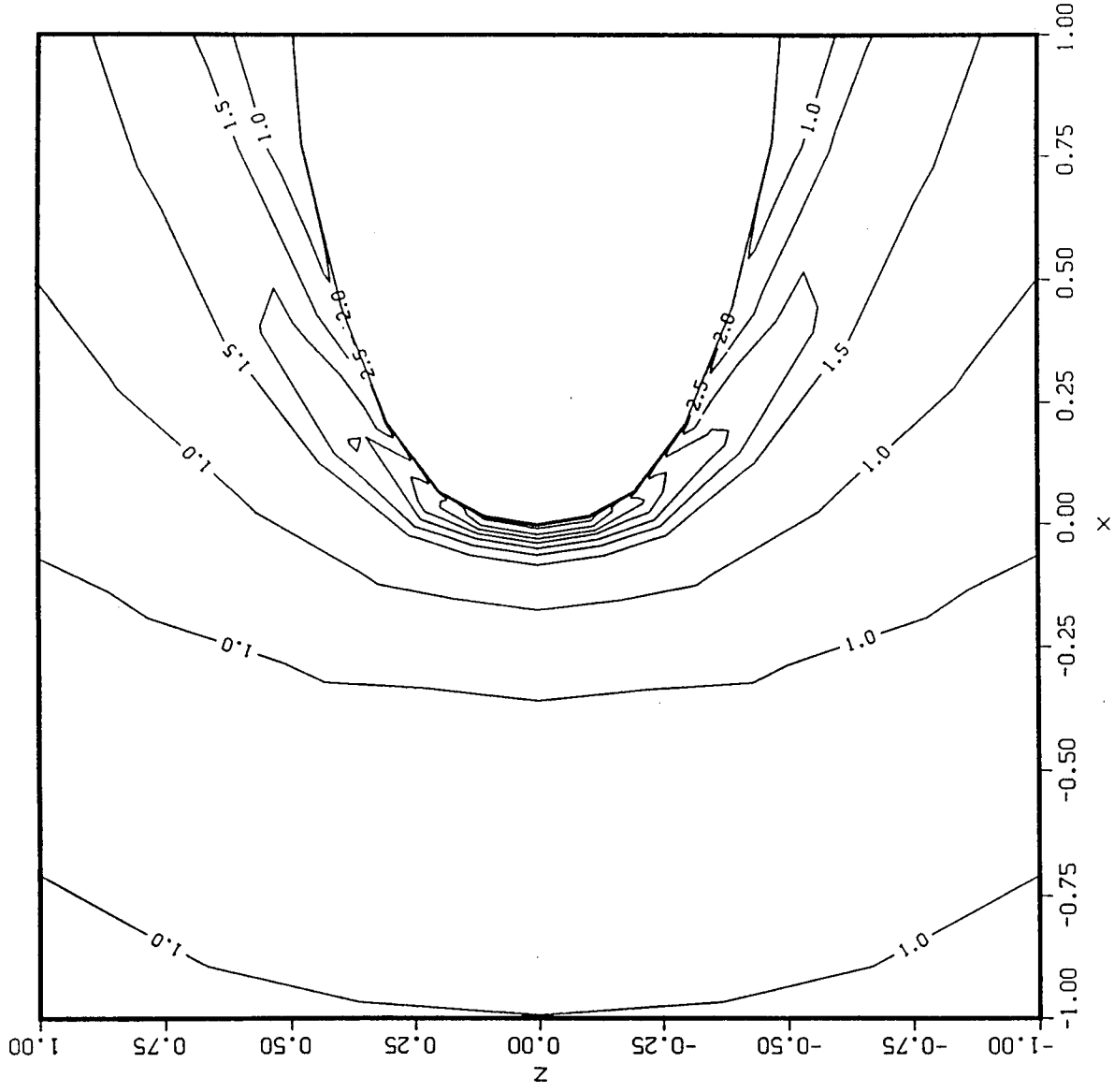
(a) Density contours.

Figure 19. Solution at the nose.
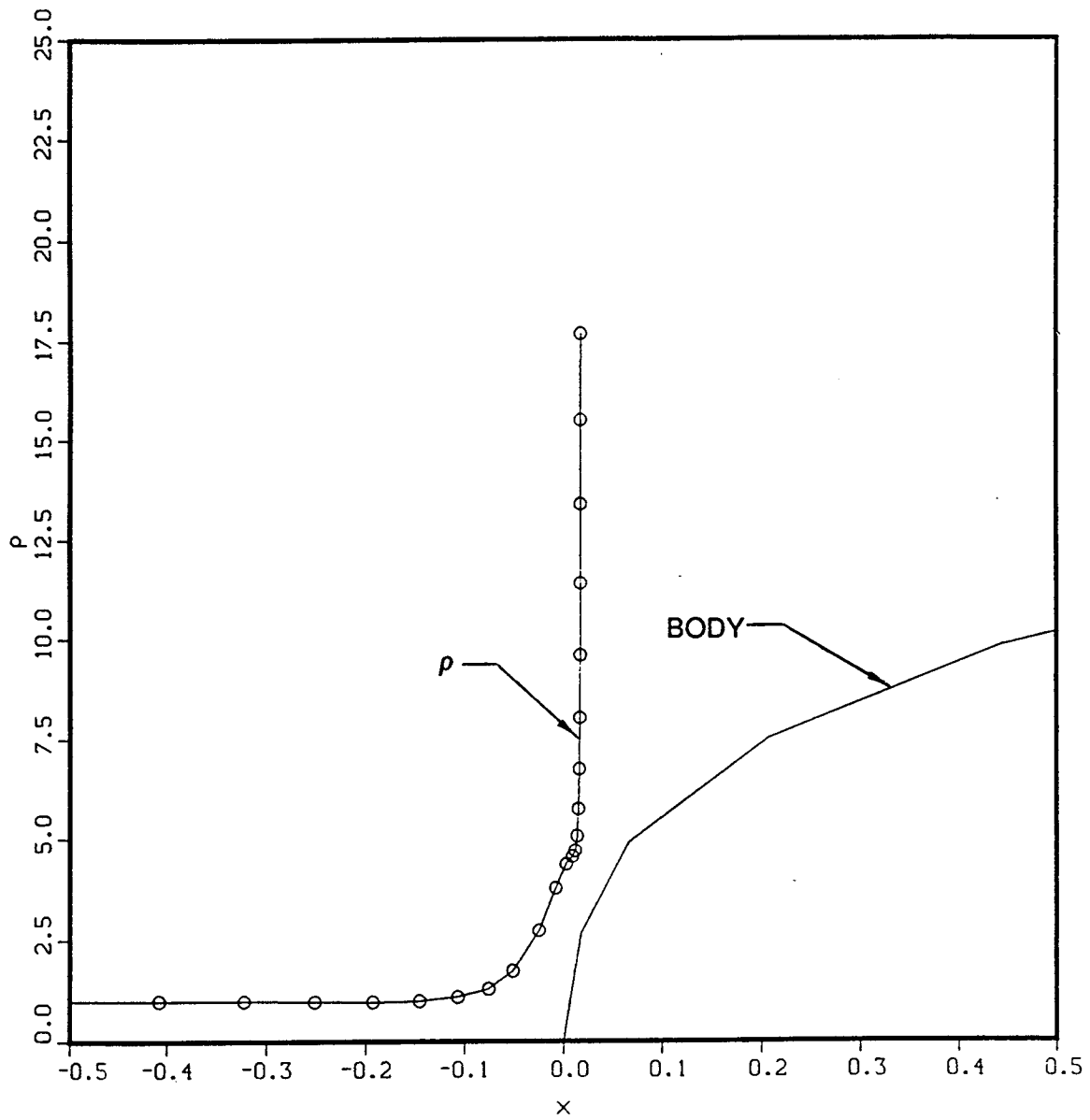
(b) Density profile along a grid line at the stagnation point.

Figure 19. Continued.
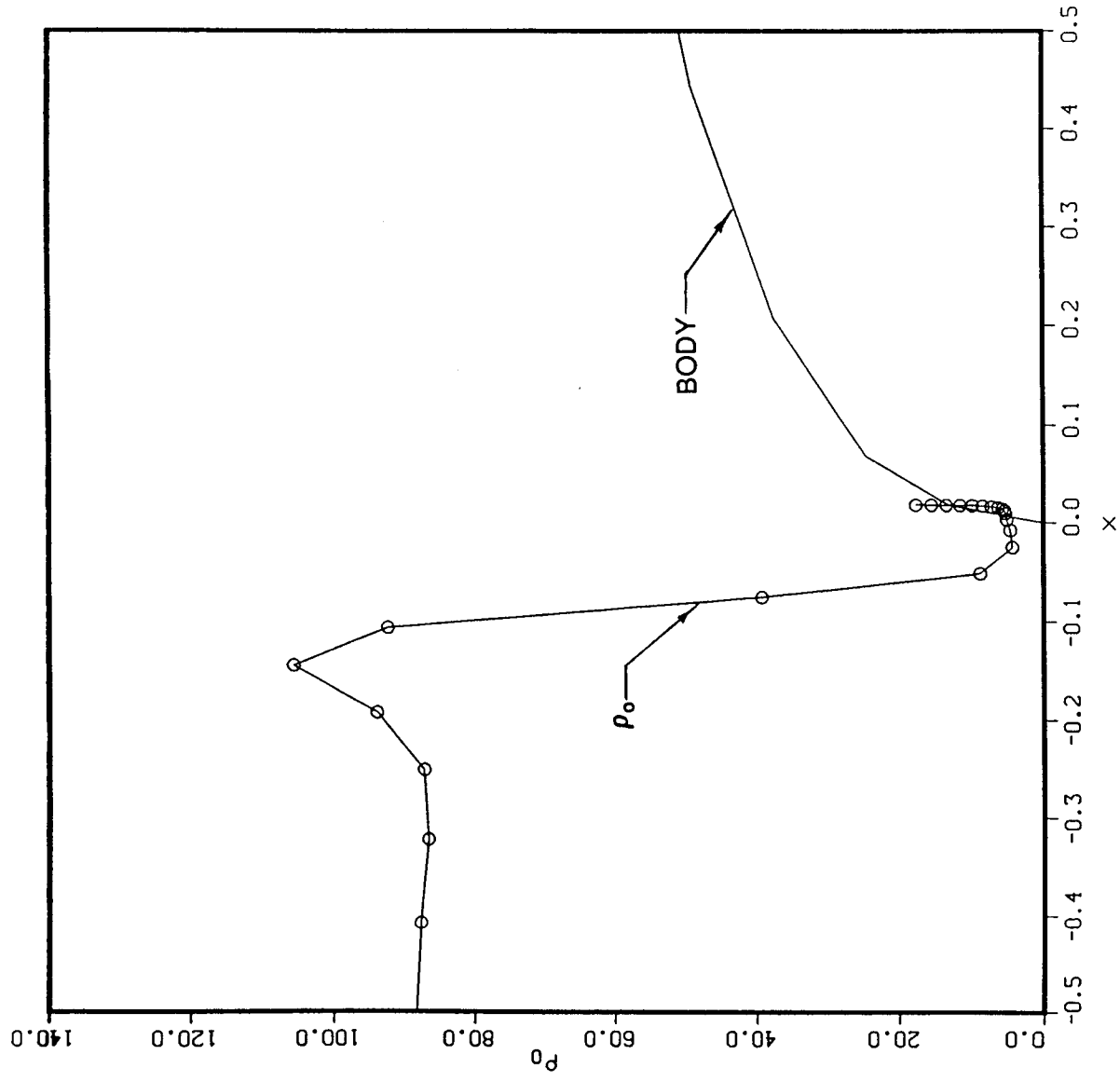
(c) Stagnation density profile along a grid line at the stagnation point.

Figure 19. Concluded.

52
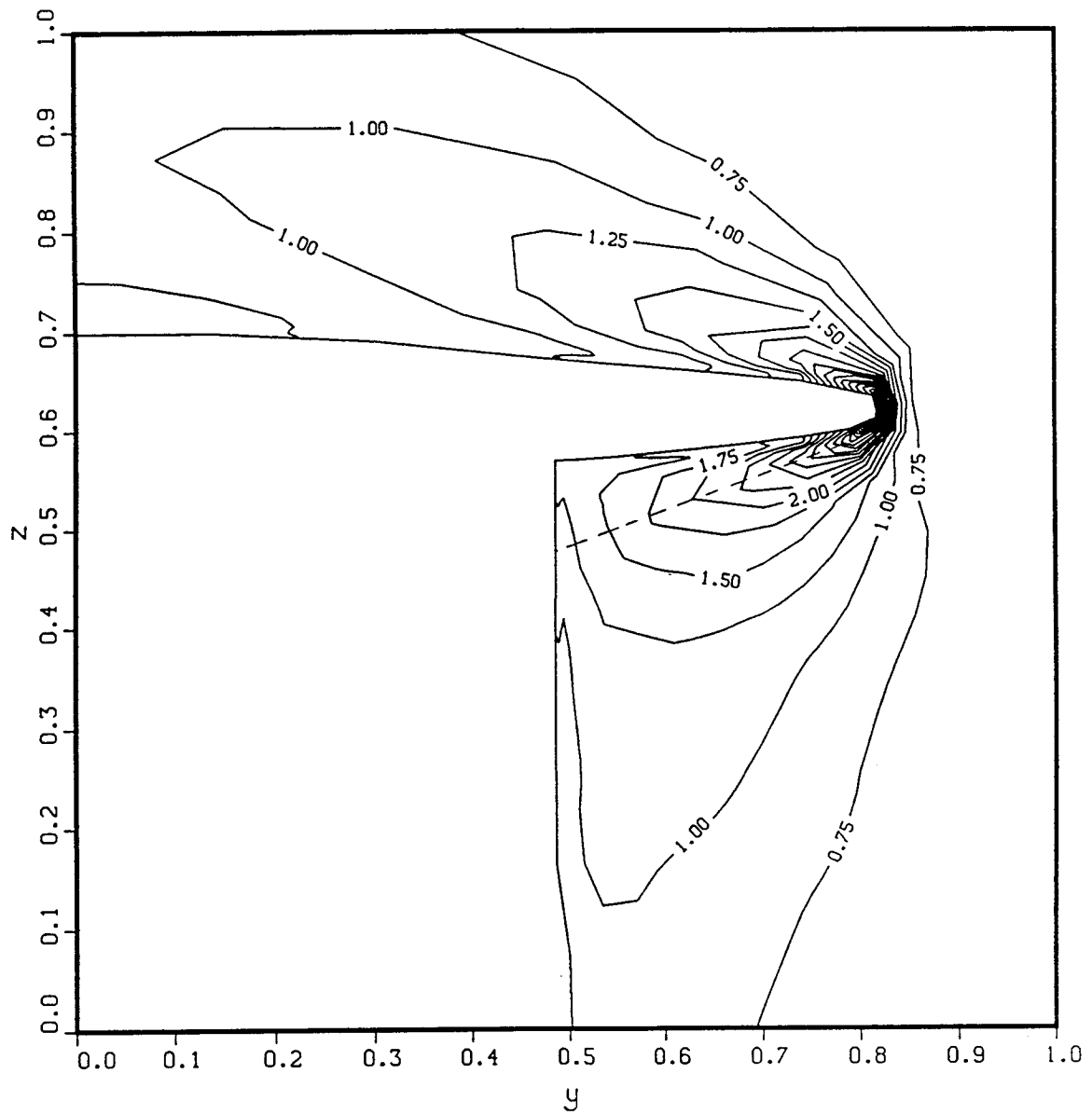
(a) Pressure contours in cross section at X/D = 6.5.

Figure 20. Flow contours showing wing leading-edge shock wave.
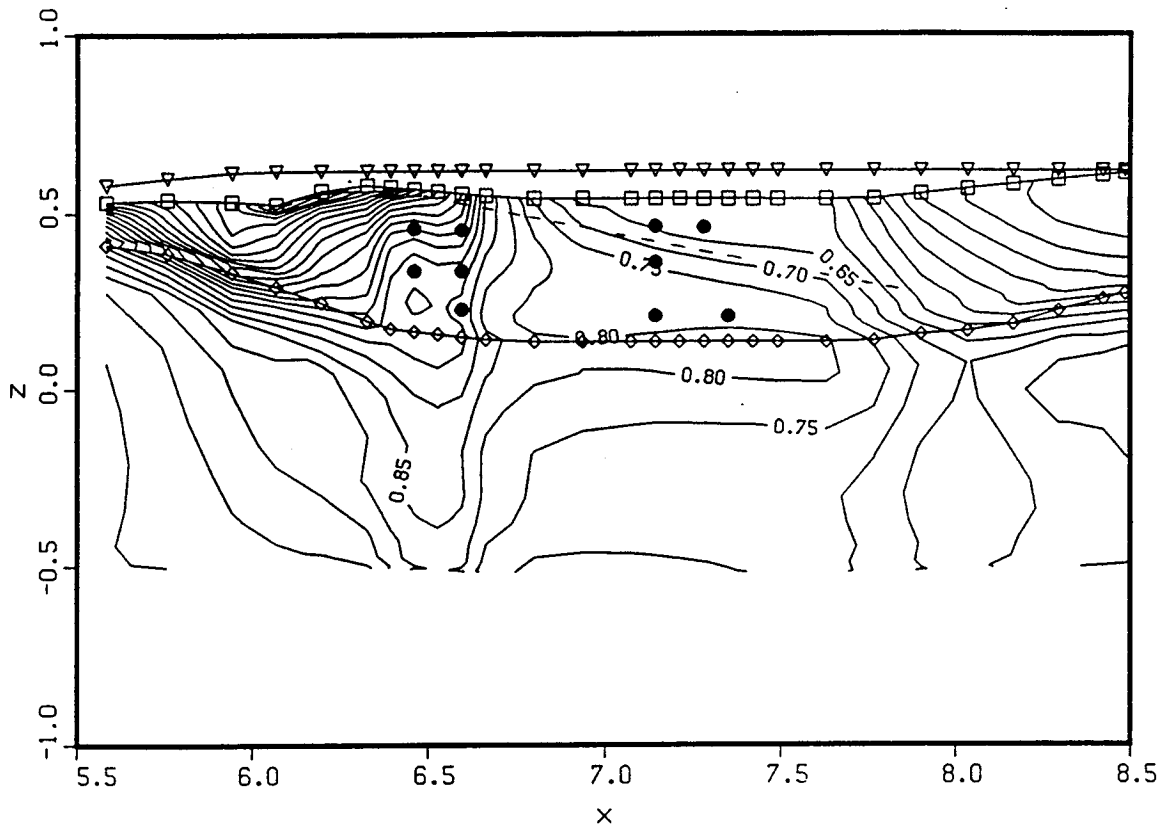
(b) Pressure contours on fillet sidewall.

Figure 20. Continued.
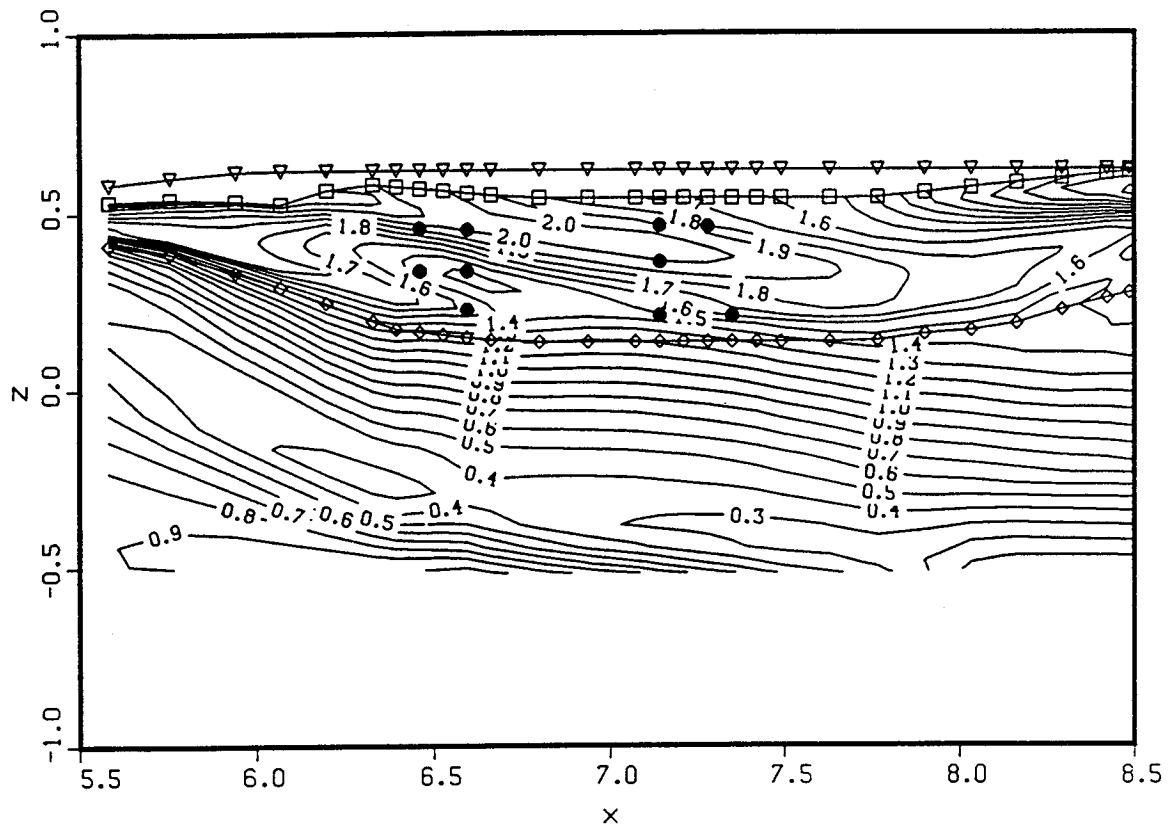
(c) Velocity magnitude on fillet sidewall on $K = 7$ surface.

Figure 20. Continued.
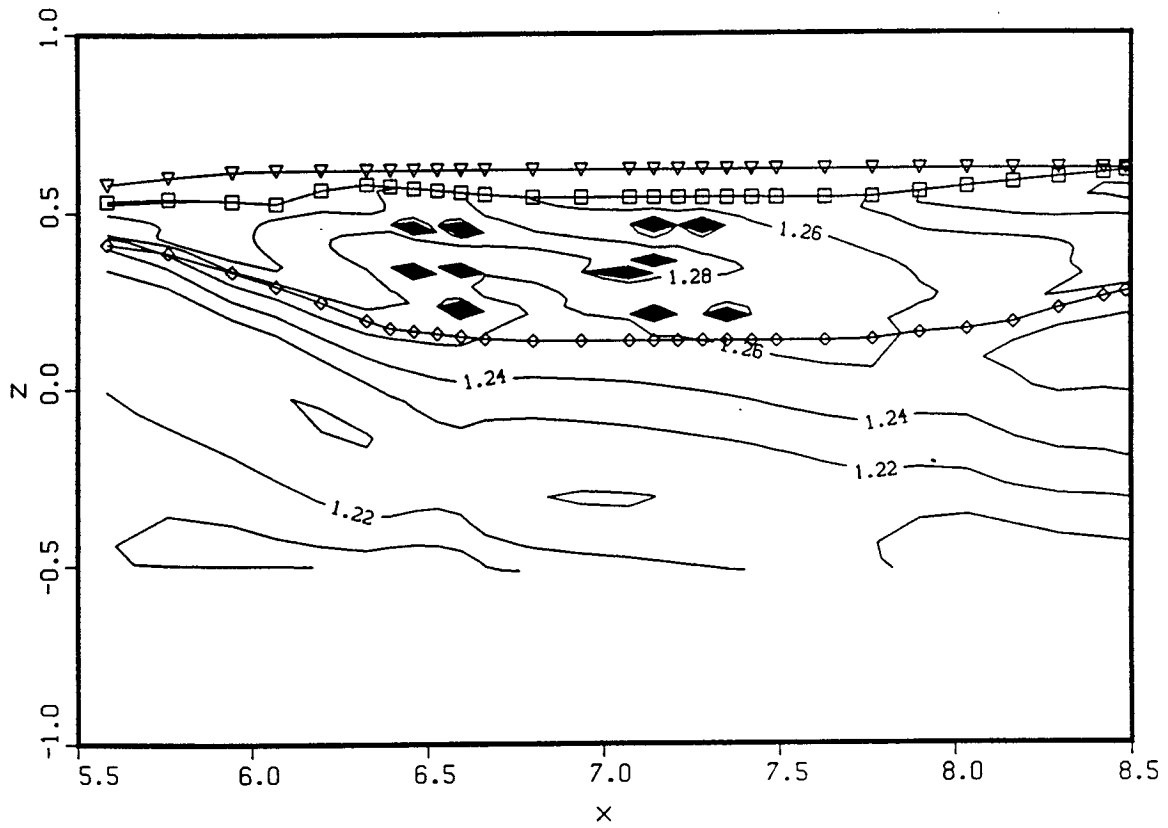
(d) Temperature contours on fillet sidewall on $K = 2$ surface.

Figure 20. Concluded.
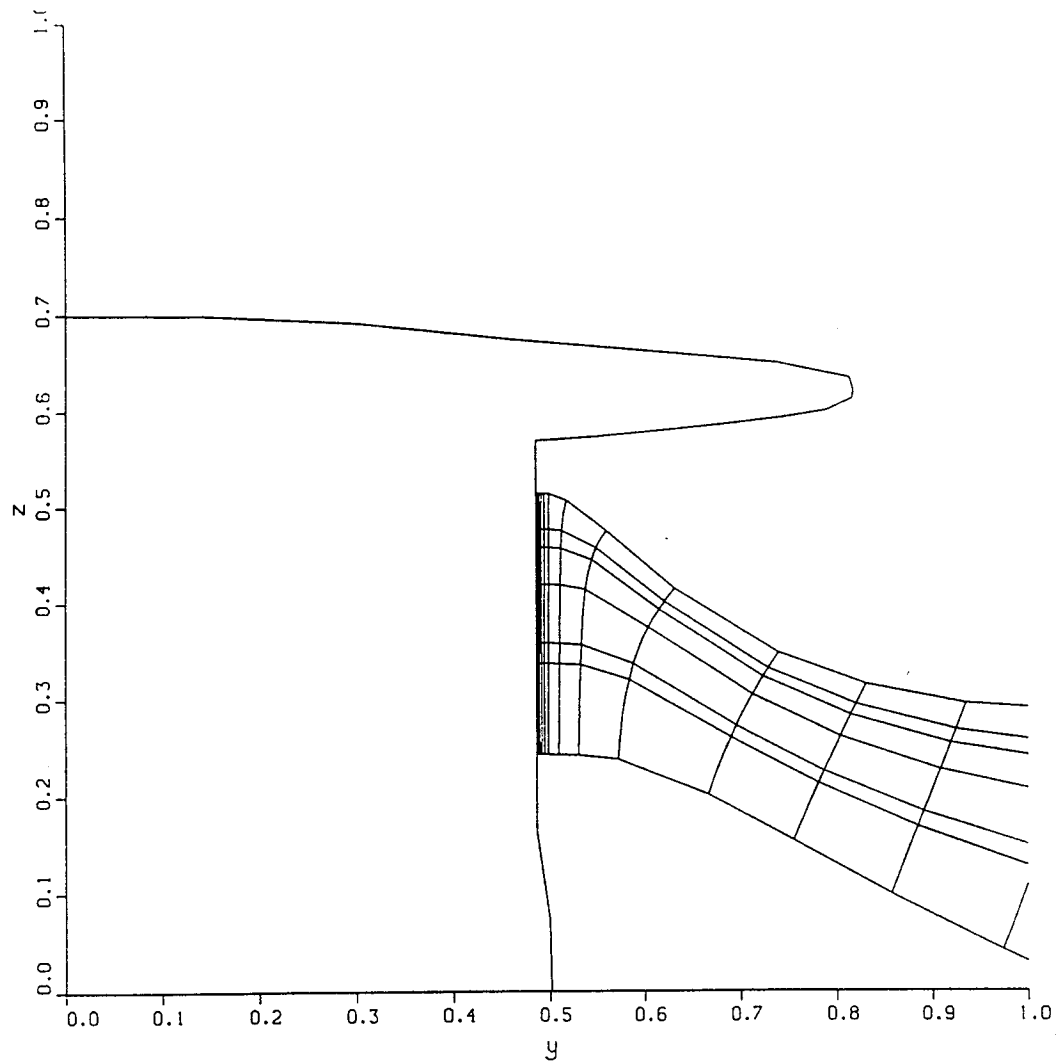
(a) Grid normal to fillet sidewall at X/D = 6.5.

Figure 21. Temperature profiles normal to the fillet sidewall.
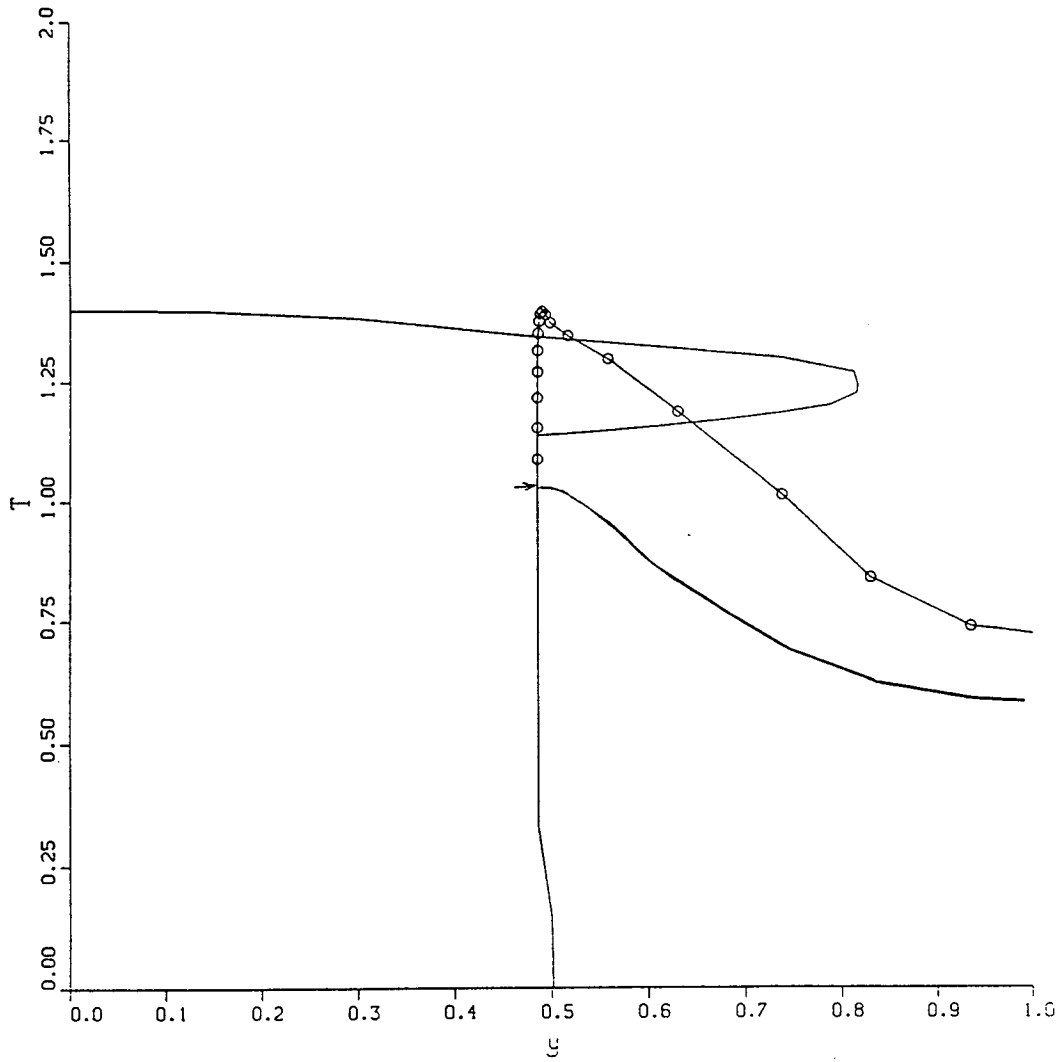
(b) Temperature profile at top of fillet grid.

Figure 21. Continued.
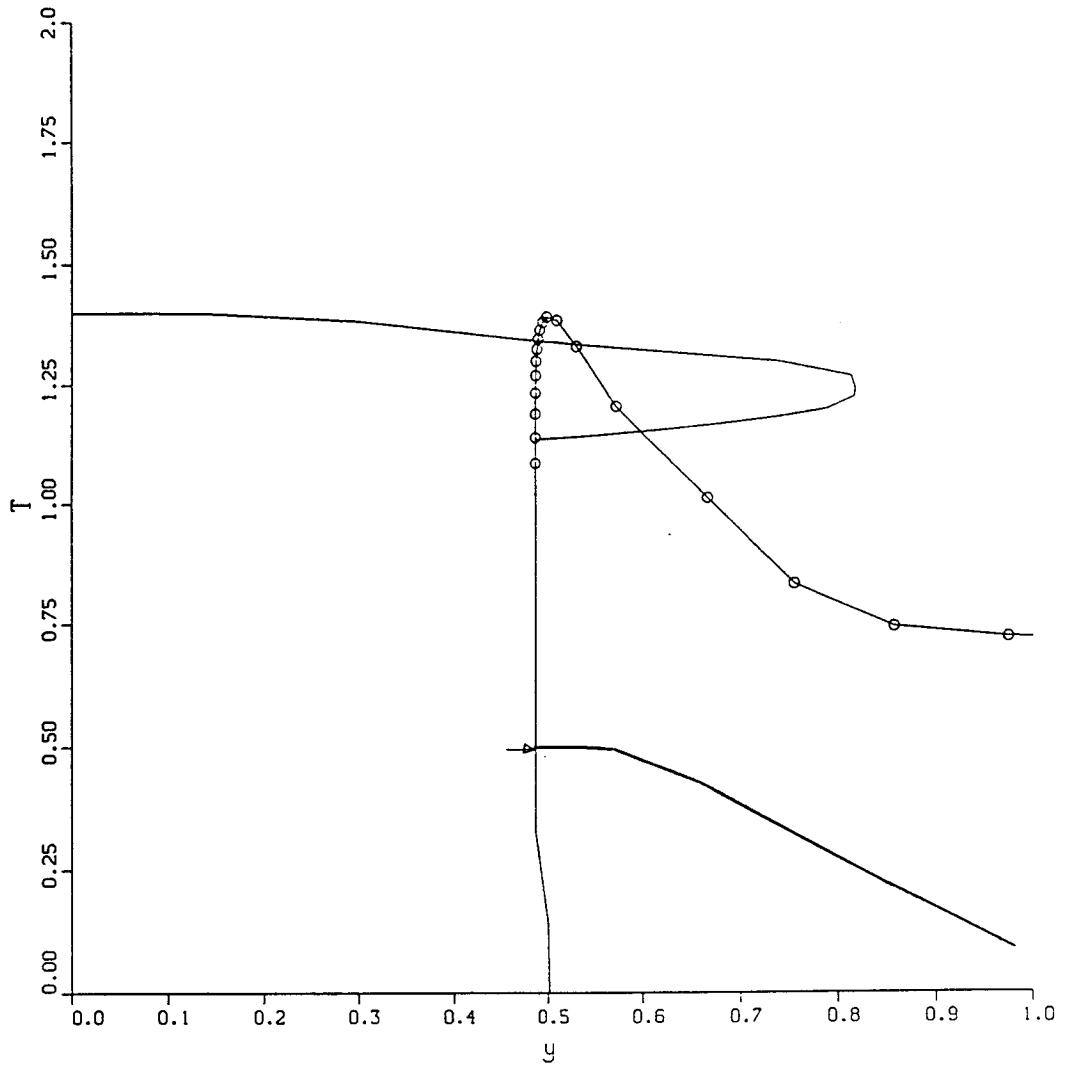
(c) Temperature profile at bottom of fillet grid.

Figure 21. Continued.
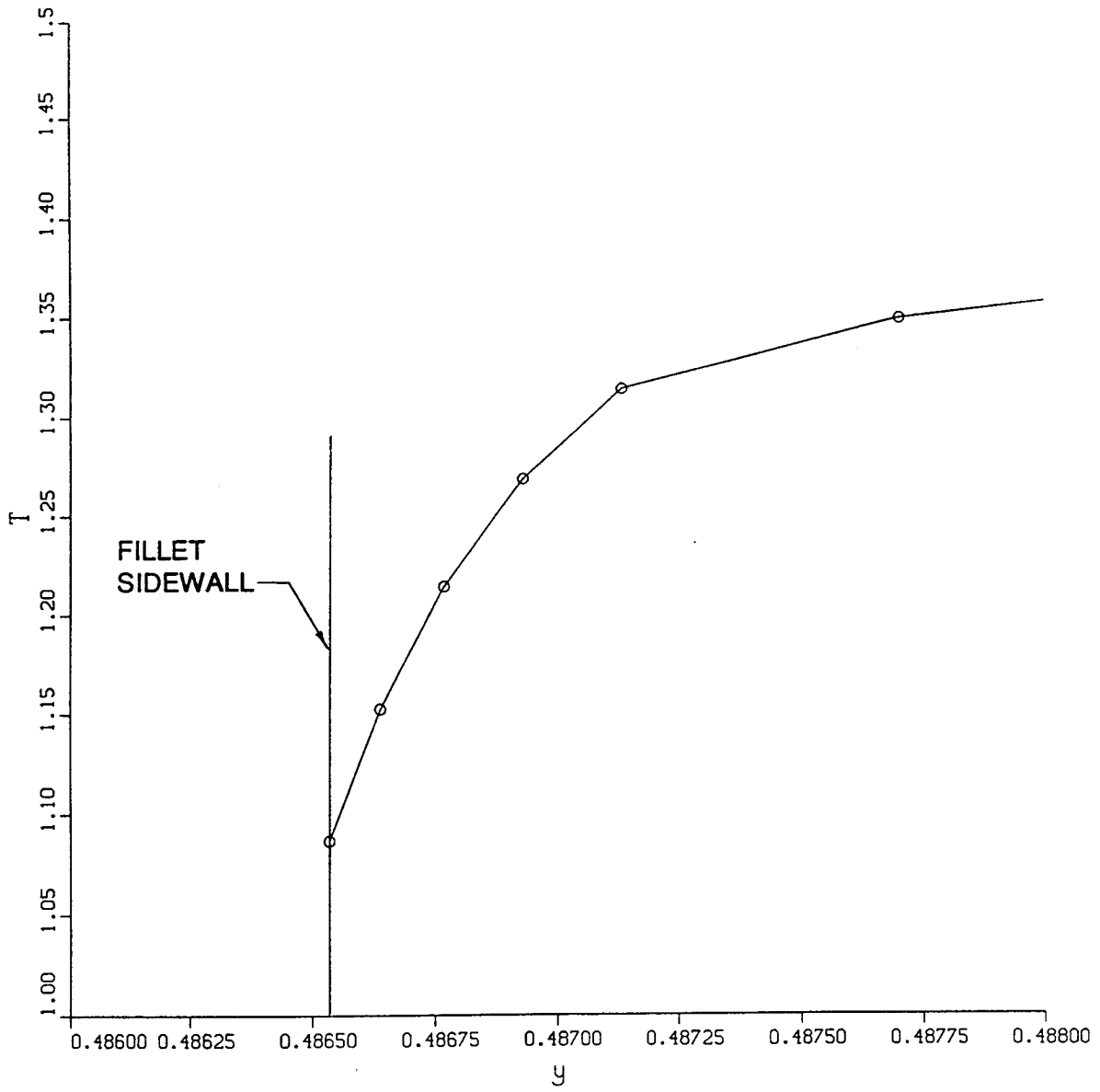
(d) Detail of temperature profile at top of fillet grid.

Figure 21. Concluded.
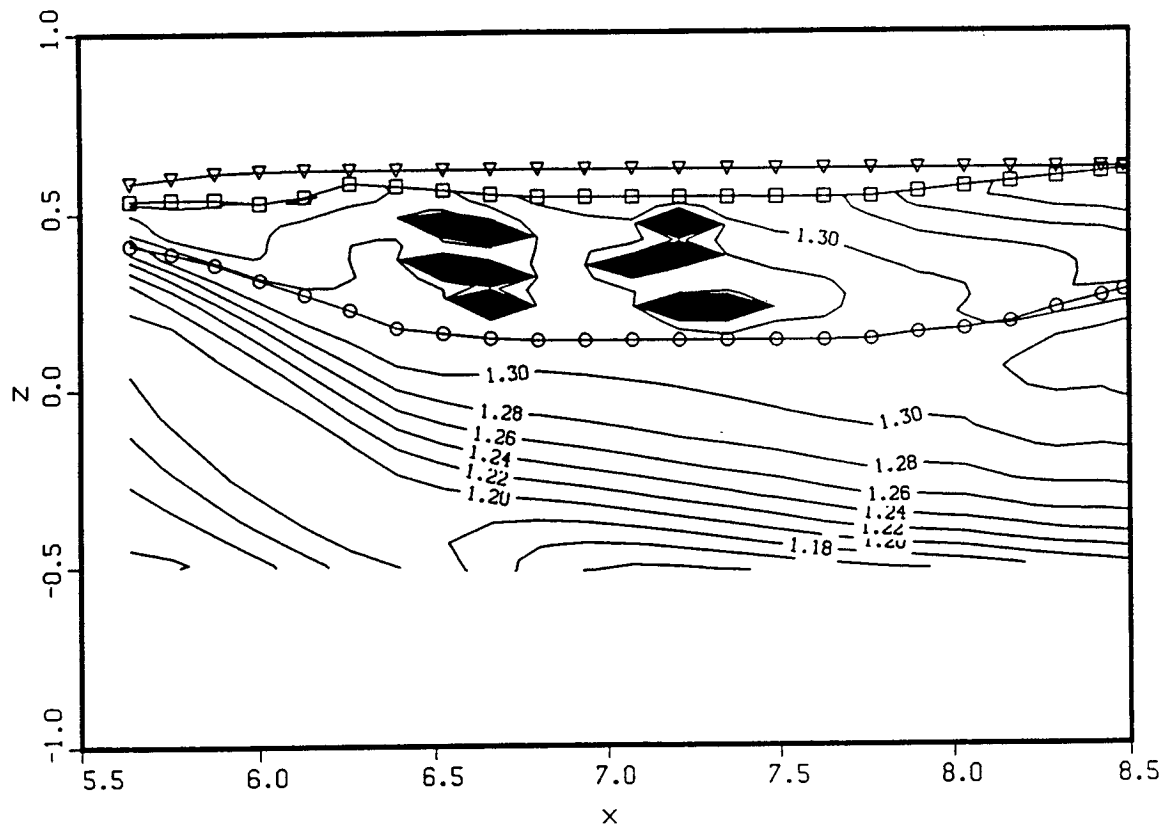
(a) $\alpha = 0.5°$.

Figure 22. Effect of angle-of-attack perturbation on temperature at $K = 2$ for $M_\infty = 5.0$ on sm1 and sm2 grids.
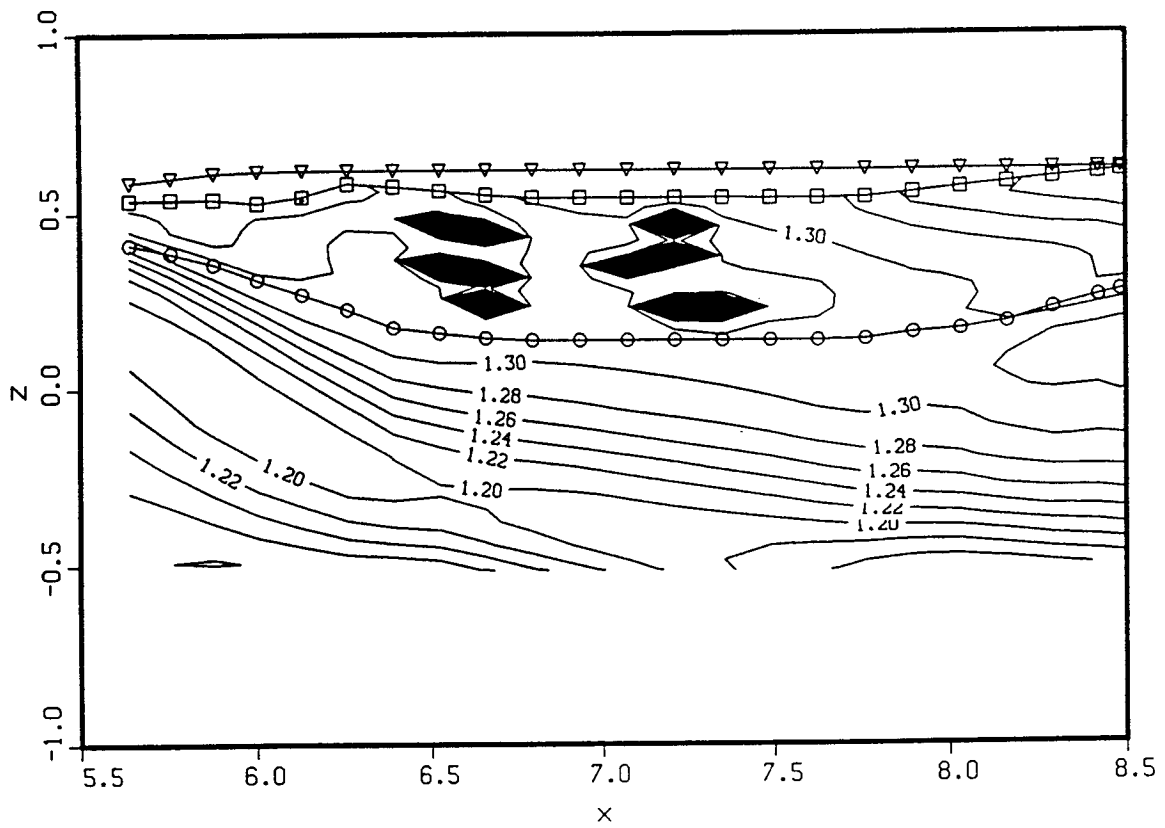
(b) $\alpha = 1.5°$.

Figure 22. Concluded.
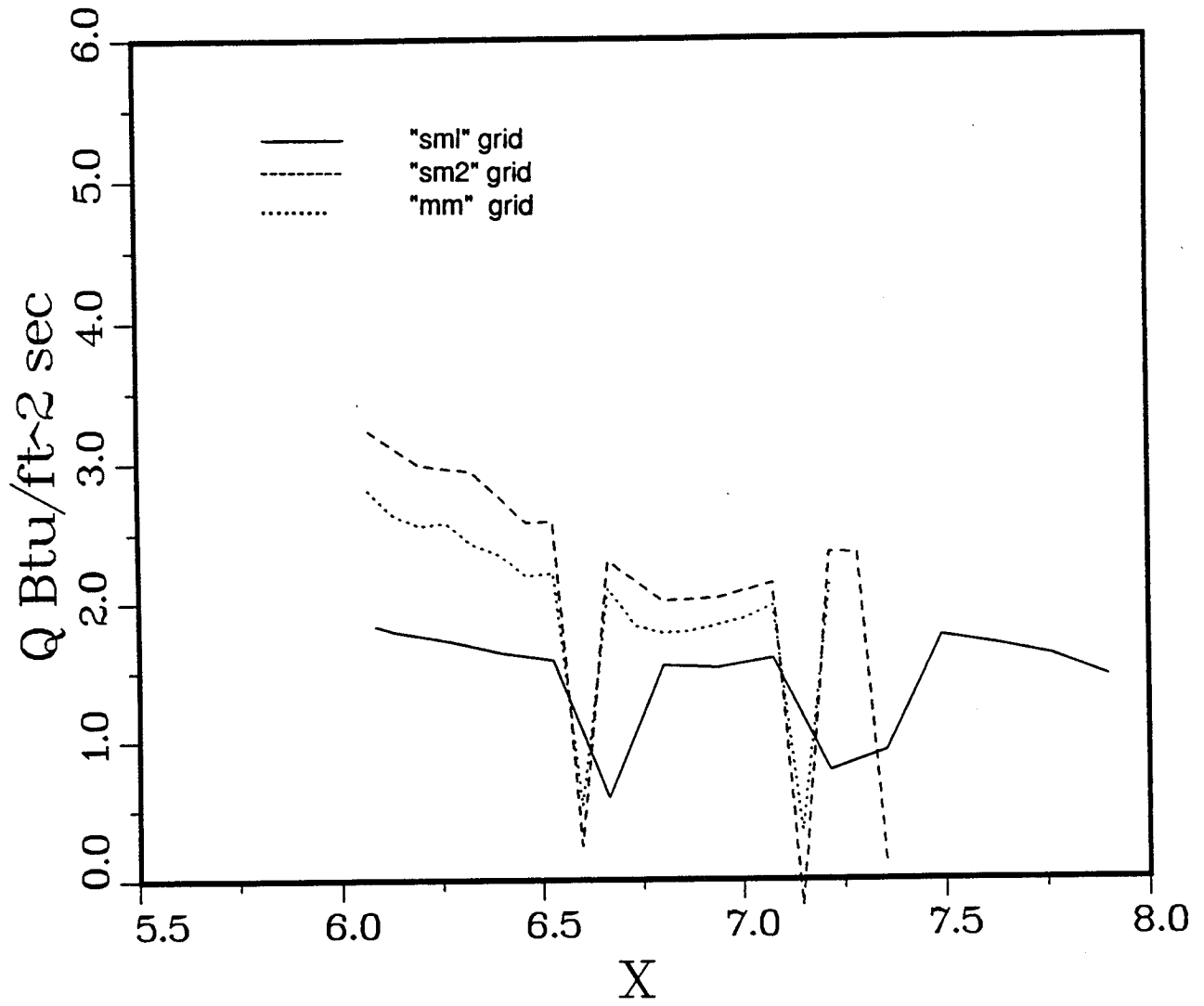
(a) sml grid.

Figure 23. Heat flux along grid lines for sml, sm2, and mm grids.
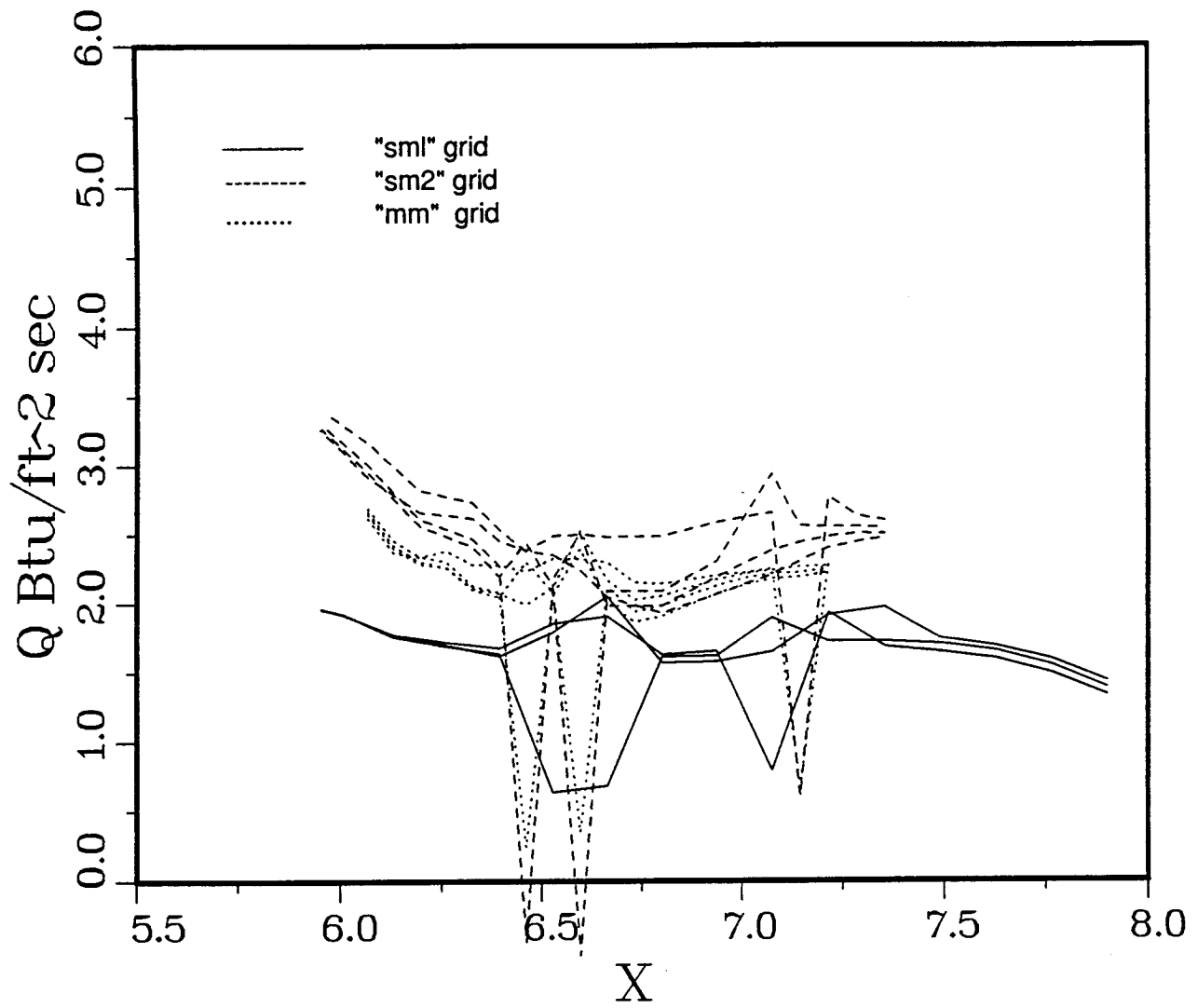
(b) sm2 grid.

Figure 23. Continued.
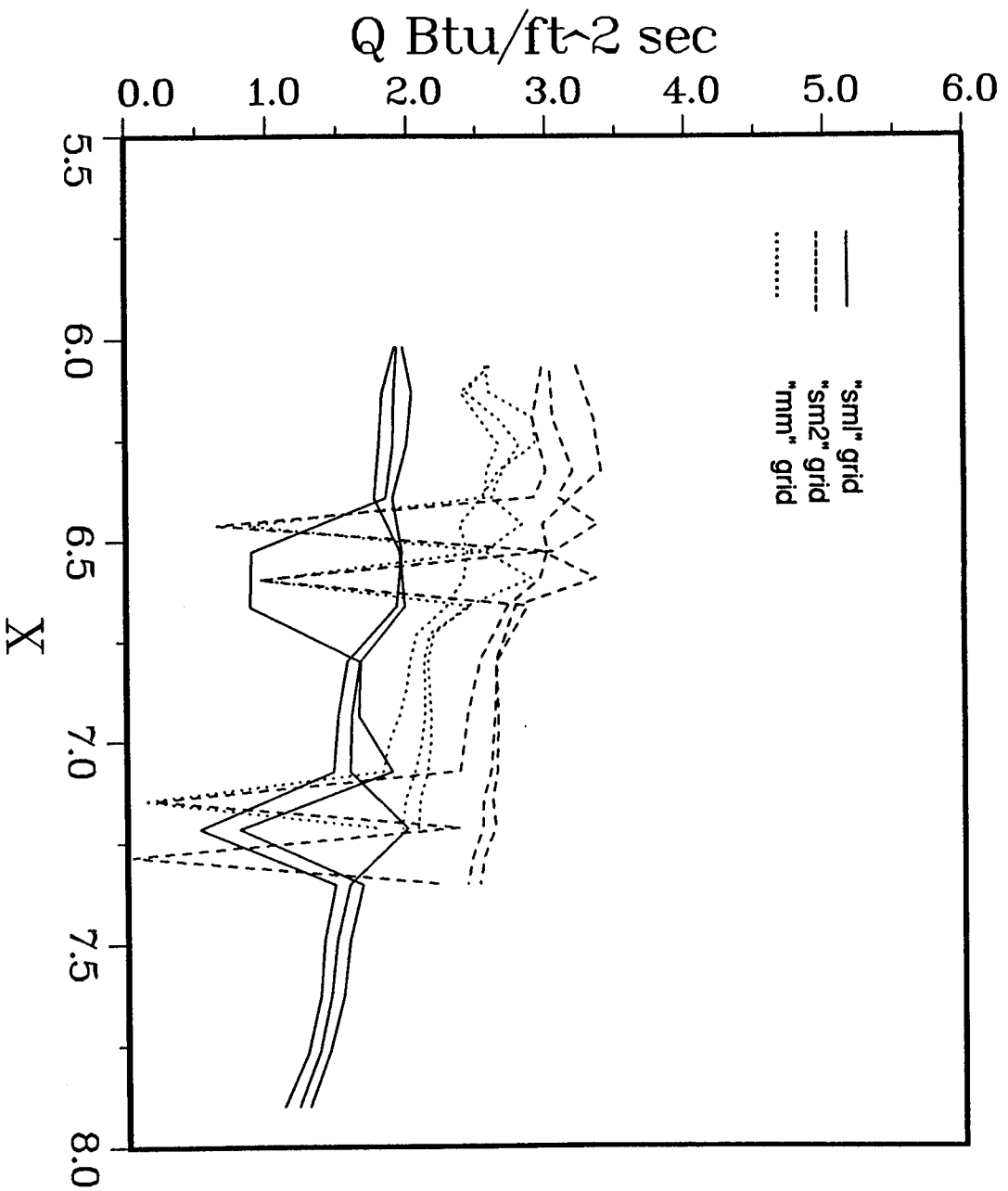
(c) mm grid.
Figure 23. Concluded.
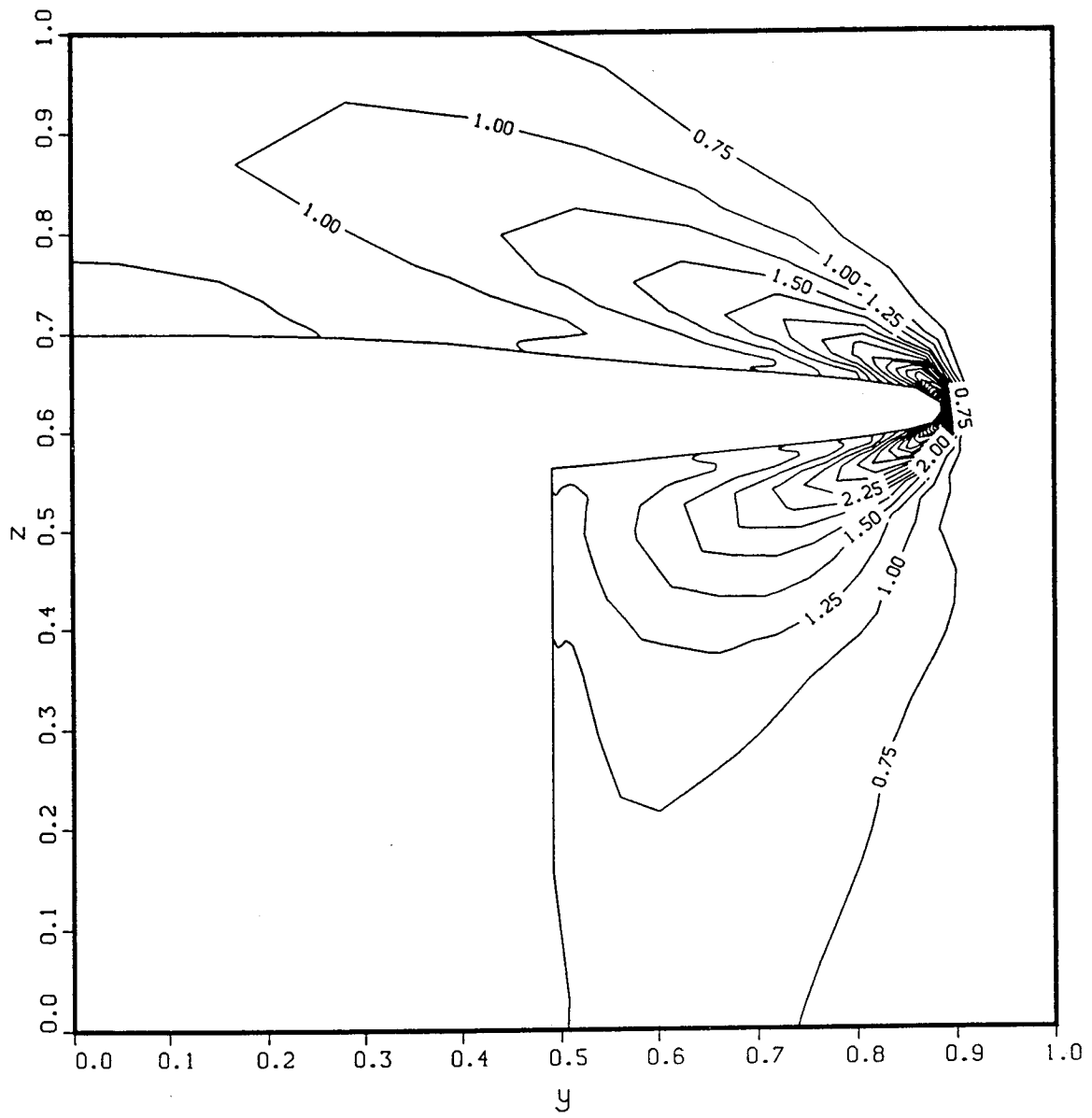
(a) sml grid.

Figure 24. Pressure contours for sml, sm2, and mm grids.
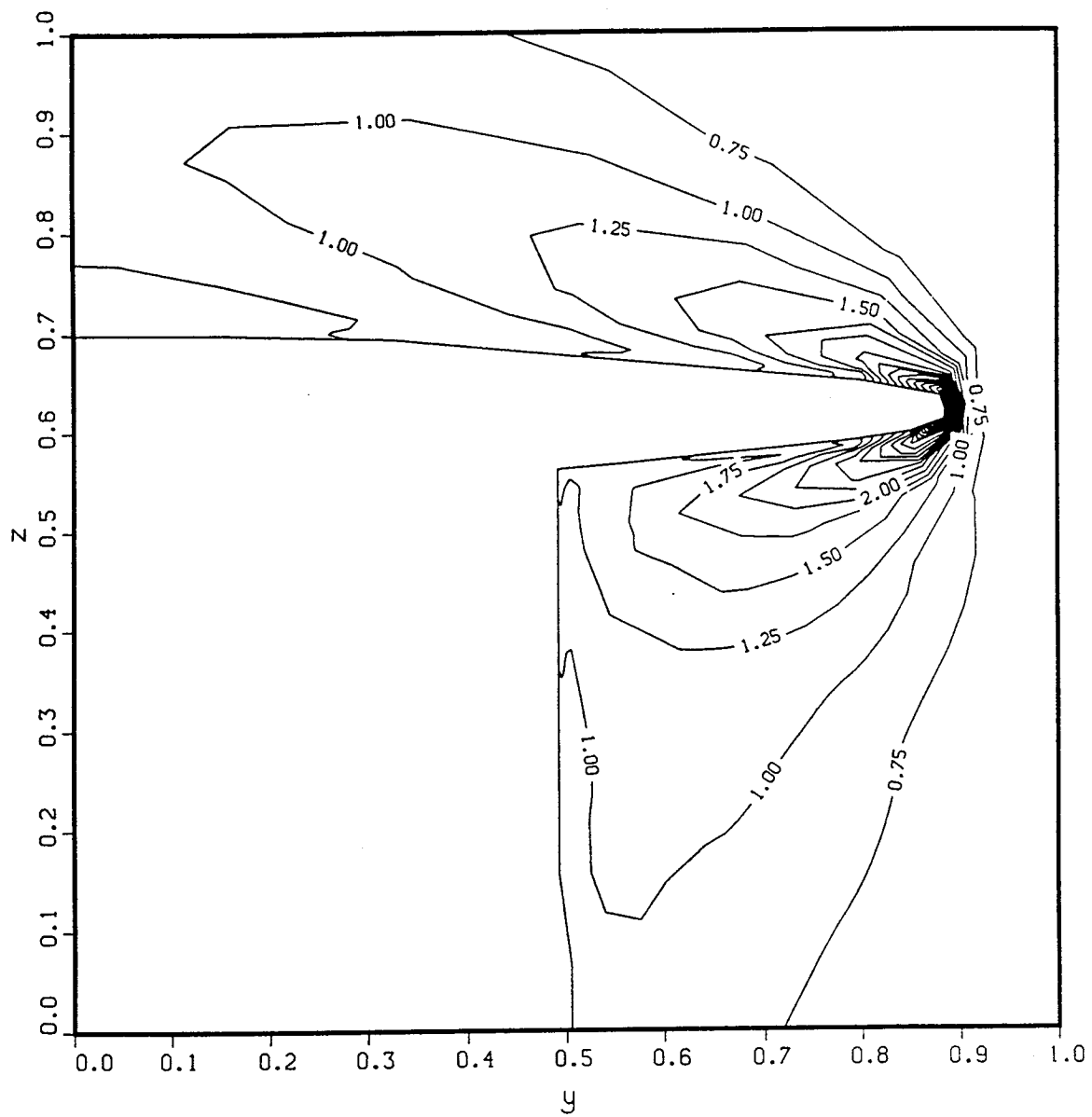
(b) sm2 grid.

Figure 24. Continued.
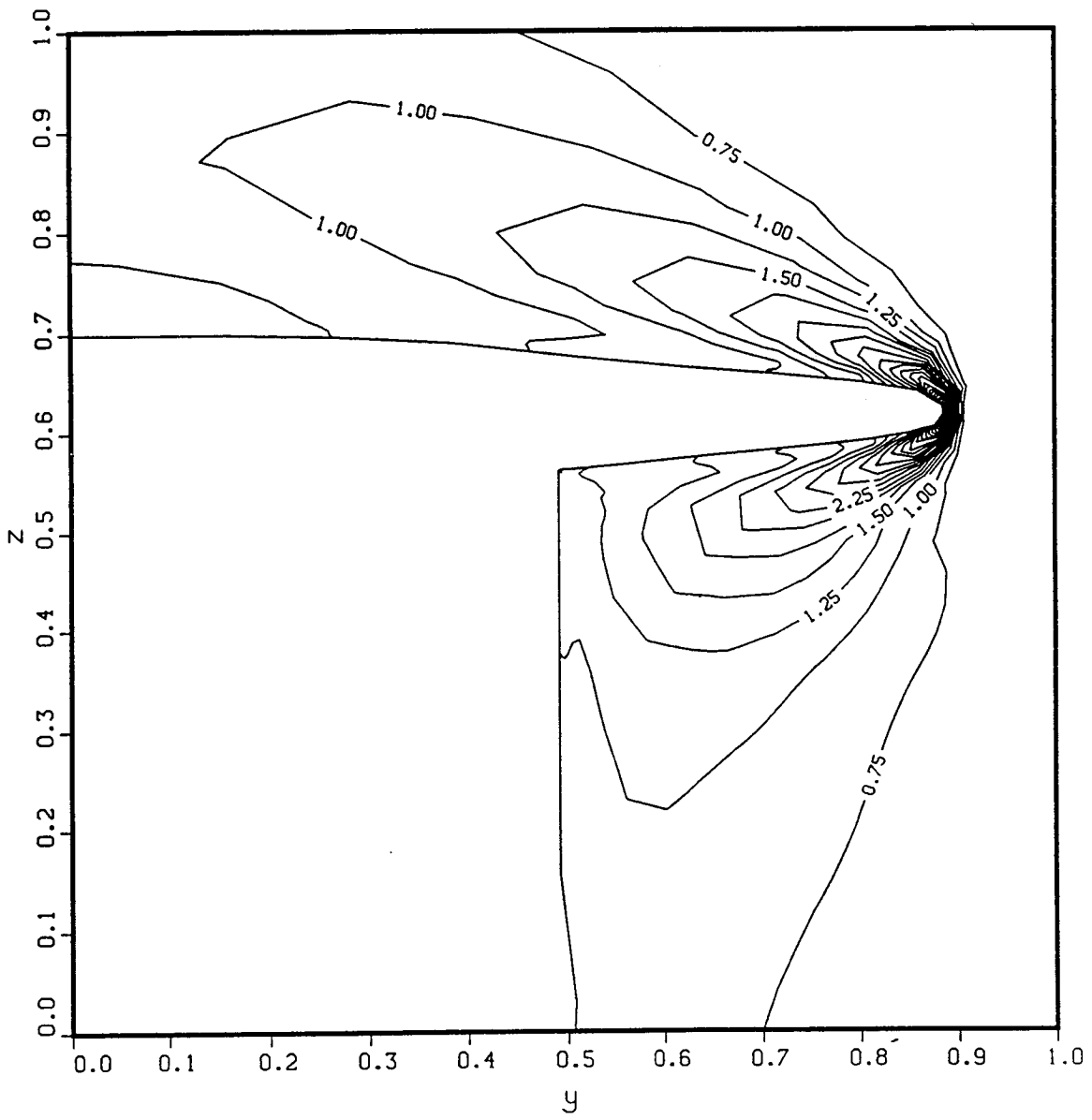
(c) mm grid.

Figure 24. Concluded.
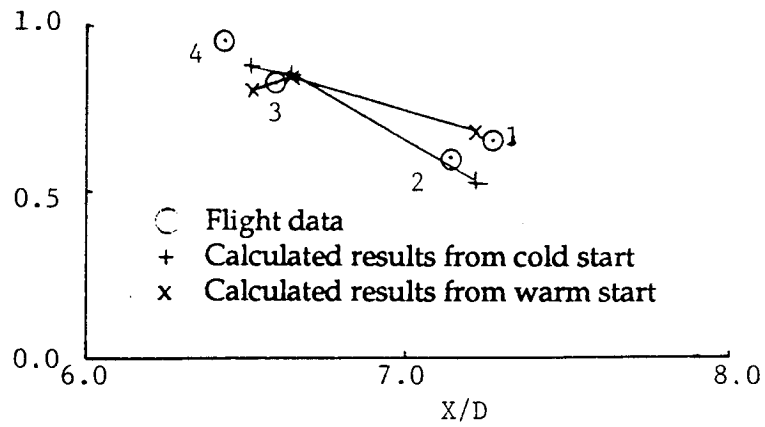
(a) Top row.
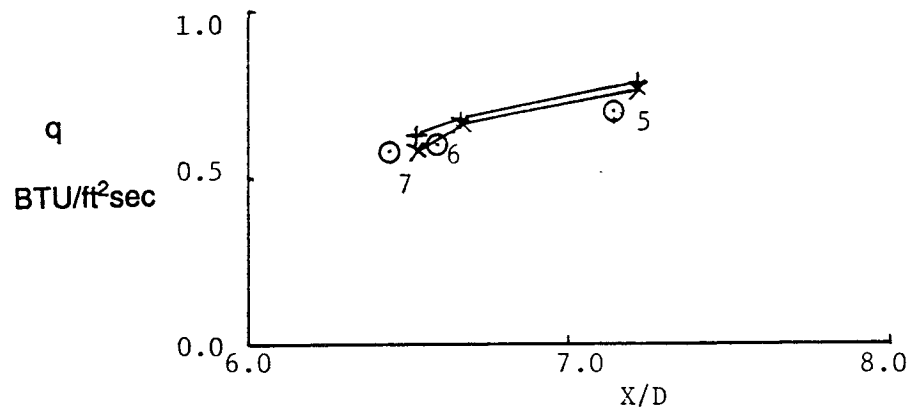
(b) Middle row.
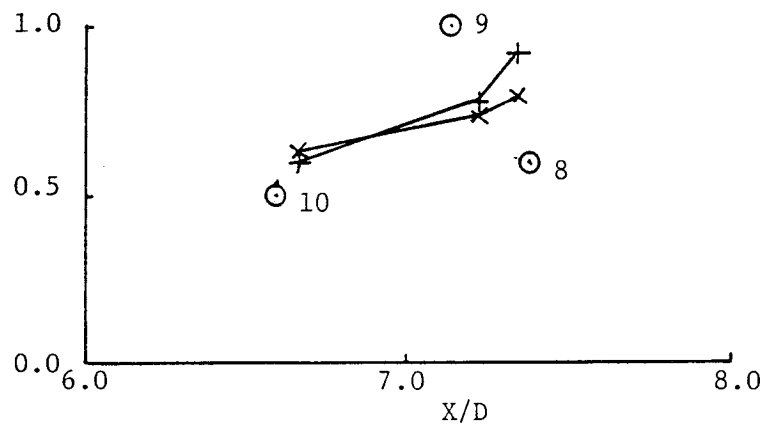
(c) Bottom row.

Figure 25. Heat flux on HRSI plugs and sml grid, $M_\infty = 5.0$, $\alpha = 0.5°$.
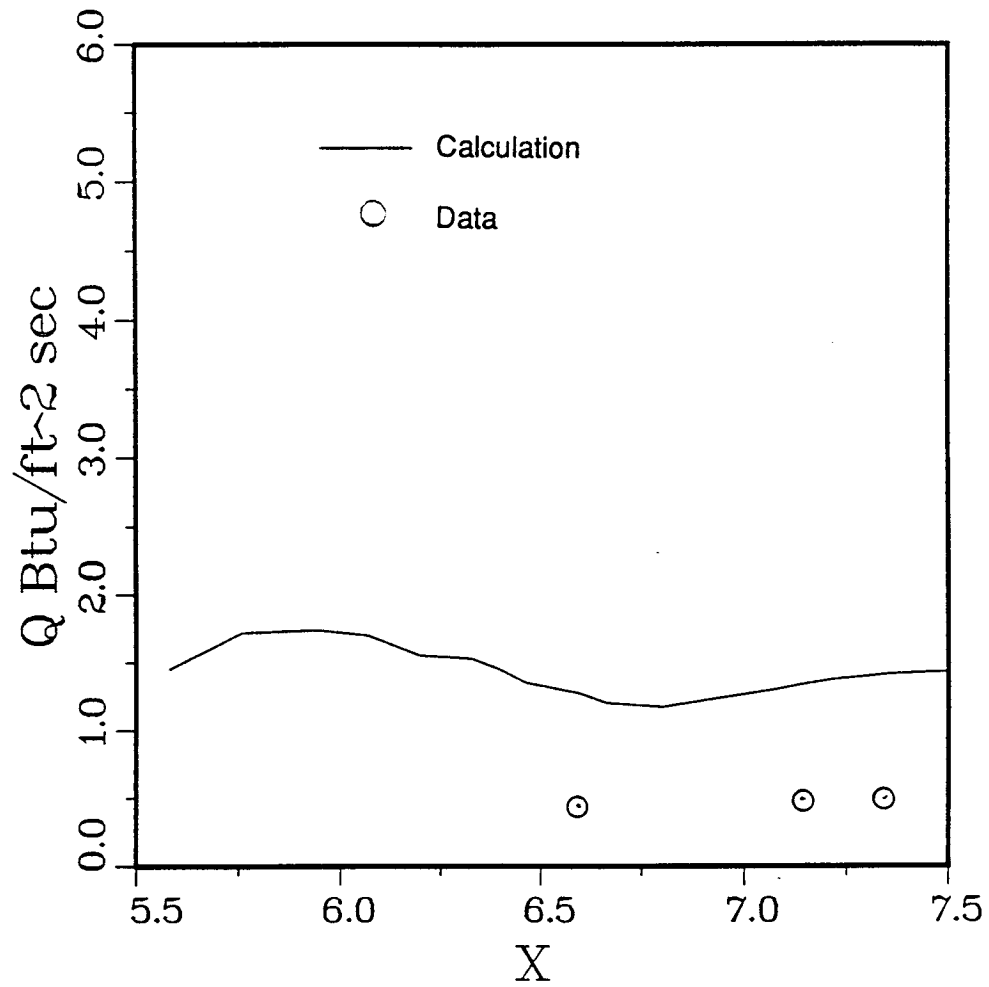
(a) $M_\infty = 3.1$, $\alpha = 7.5°$.

Figure 26. Heat flux along grid lines through bottom row of HRSI plugs for $M_\infty = 3.1$, 4.0, and 5.0 on sm2 grid.
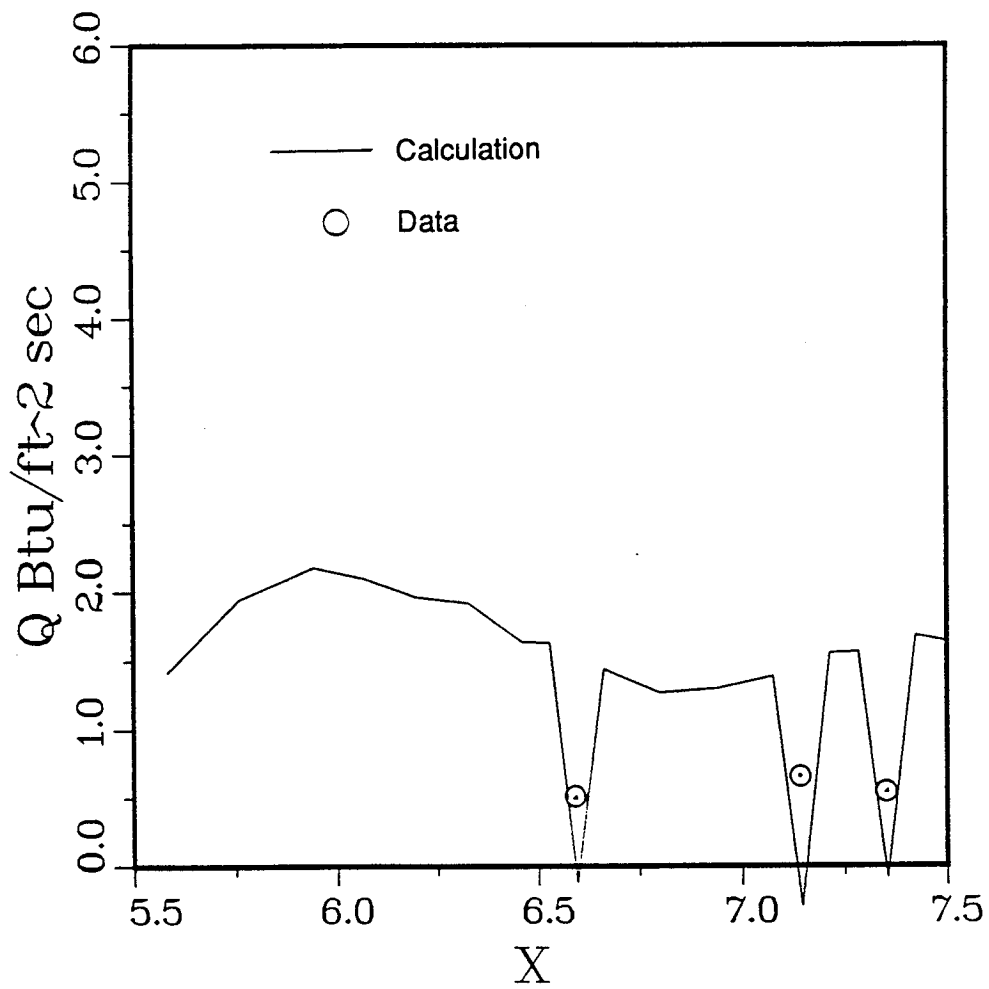
(b) $M_\infty = 4.0$, $\alpha = 4.0°$.

Figure 26. Continued.
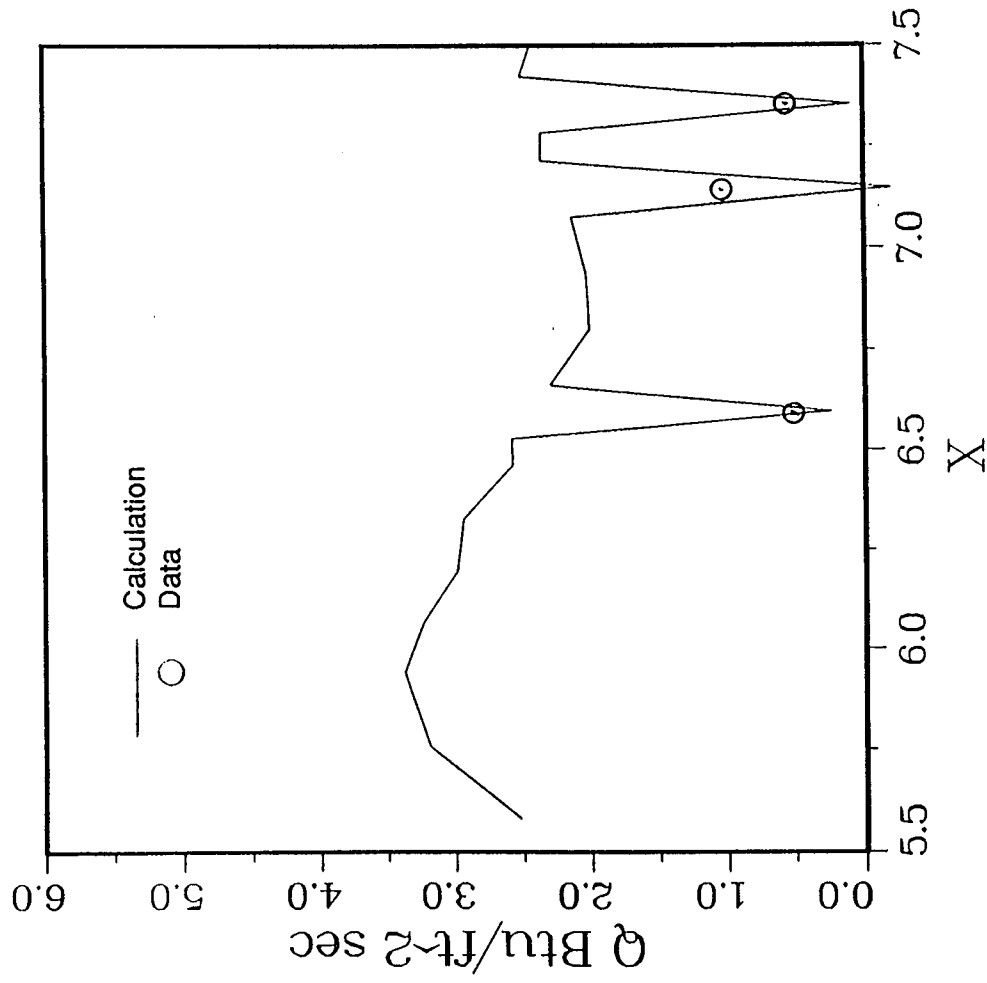
(c) $M_\infty = 5.0$, $\alpha = 0.5°$.

Figure 26. Concluded.

72
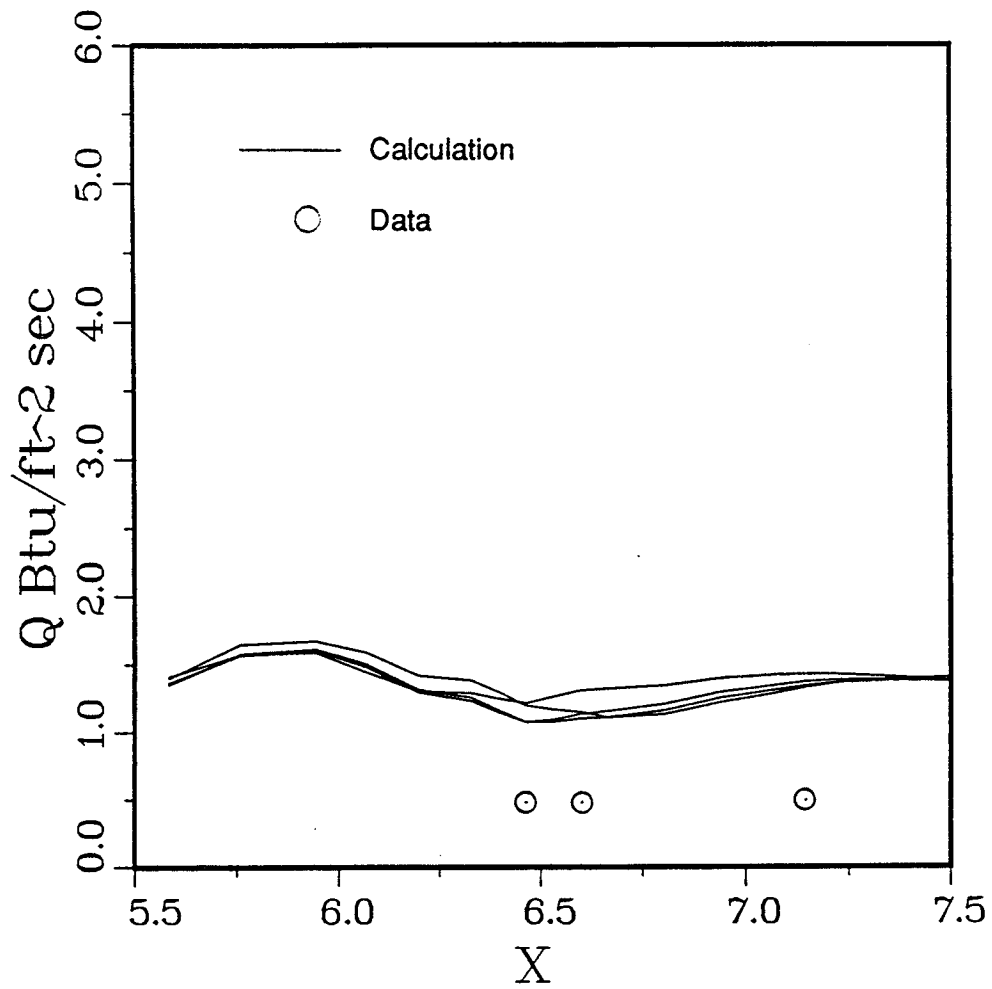
(a) $M_\infty = 3.1$, $\alpha = 7.5°$.

Figure 27. Heat flux along grid lines through middle row of HRSI plugs for $M_\infty = 3.1$, 4.0, and 5.0 on sm2 grid.
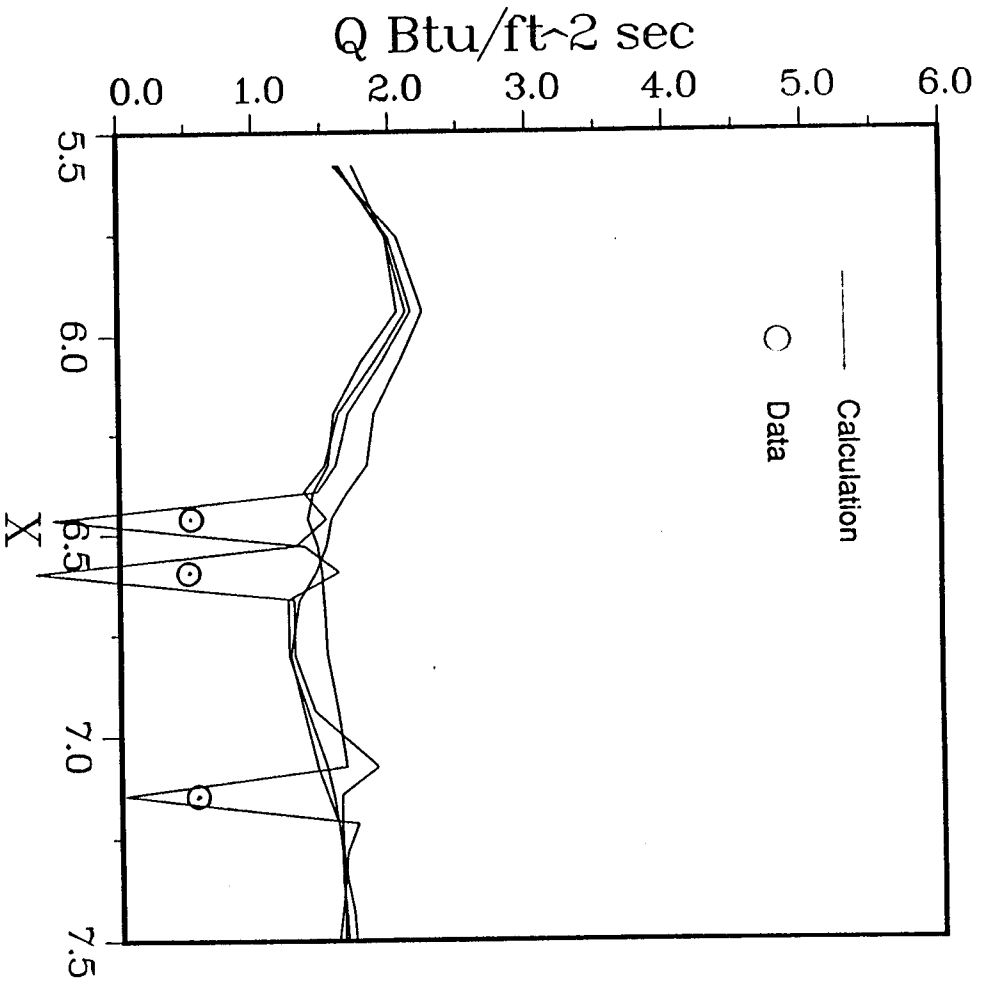
(b) $M_\infty = 4.0$, $\alpha = 4.0°$.

Figure 27. Continued.
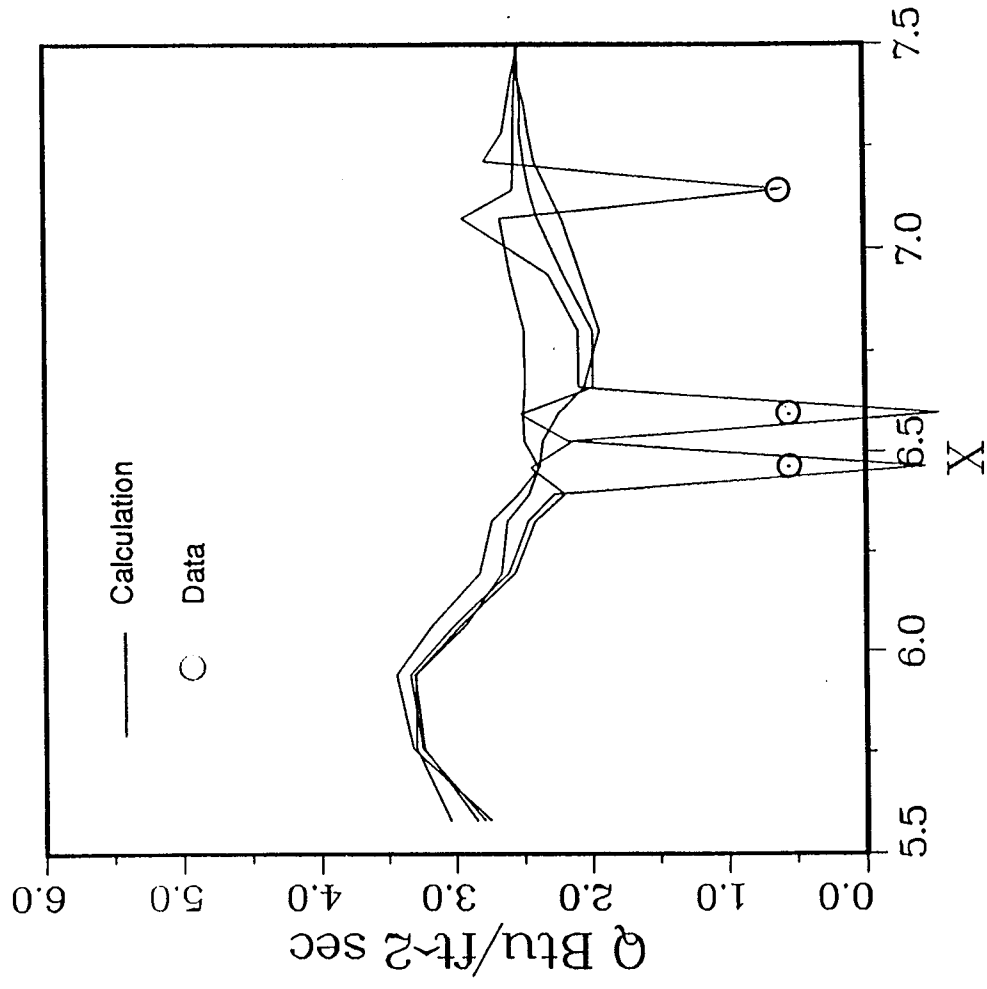
(c) $M_\infty = 5.0$, $\alpha = 0.5°$.

Figure 27. Concluded.
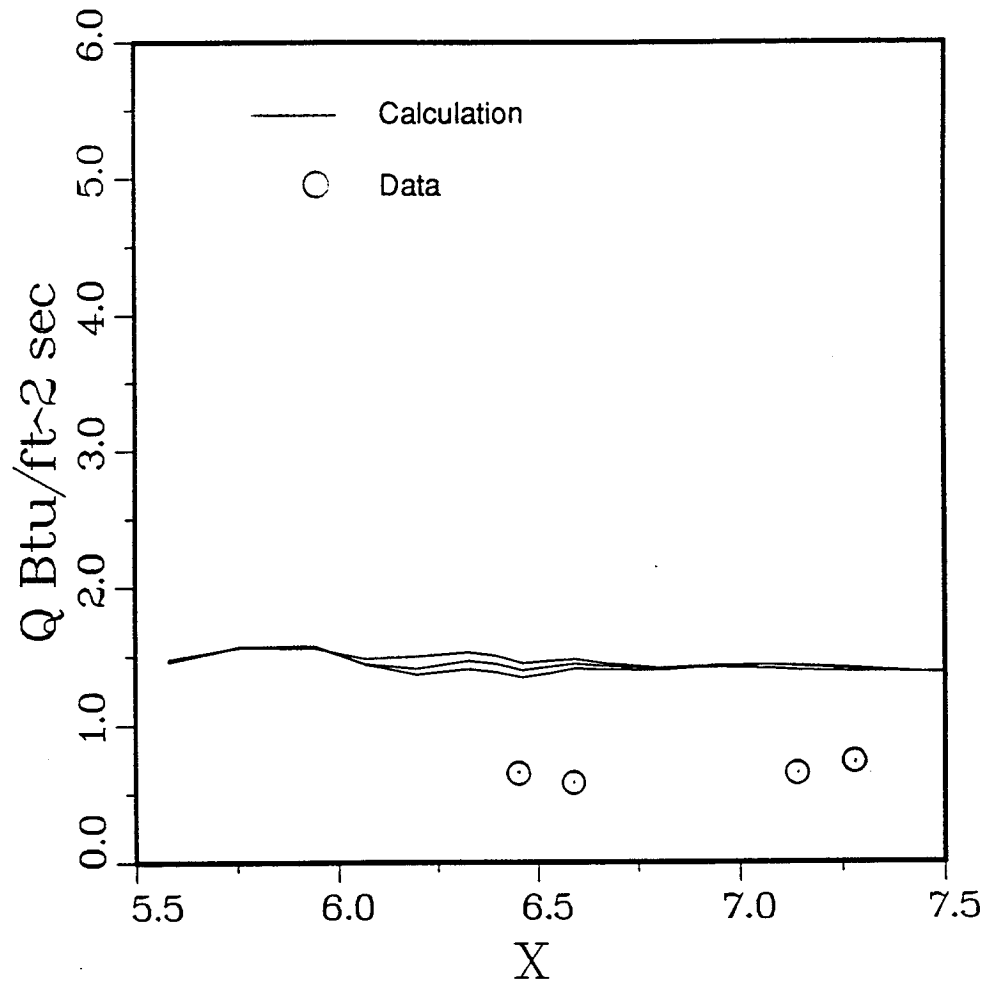
(a) $M_\infty = 3.1$, $\alpha = 7.5°$.

Figure 28. Heat flux along grid lines through top row of HRSI plugs for M_∞ = 3.1, 4.0, and 5.0 on sm2 grid.
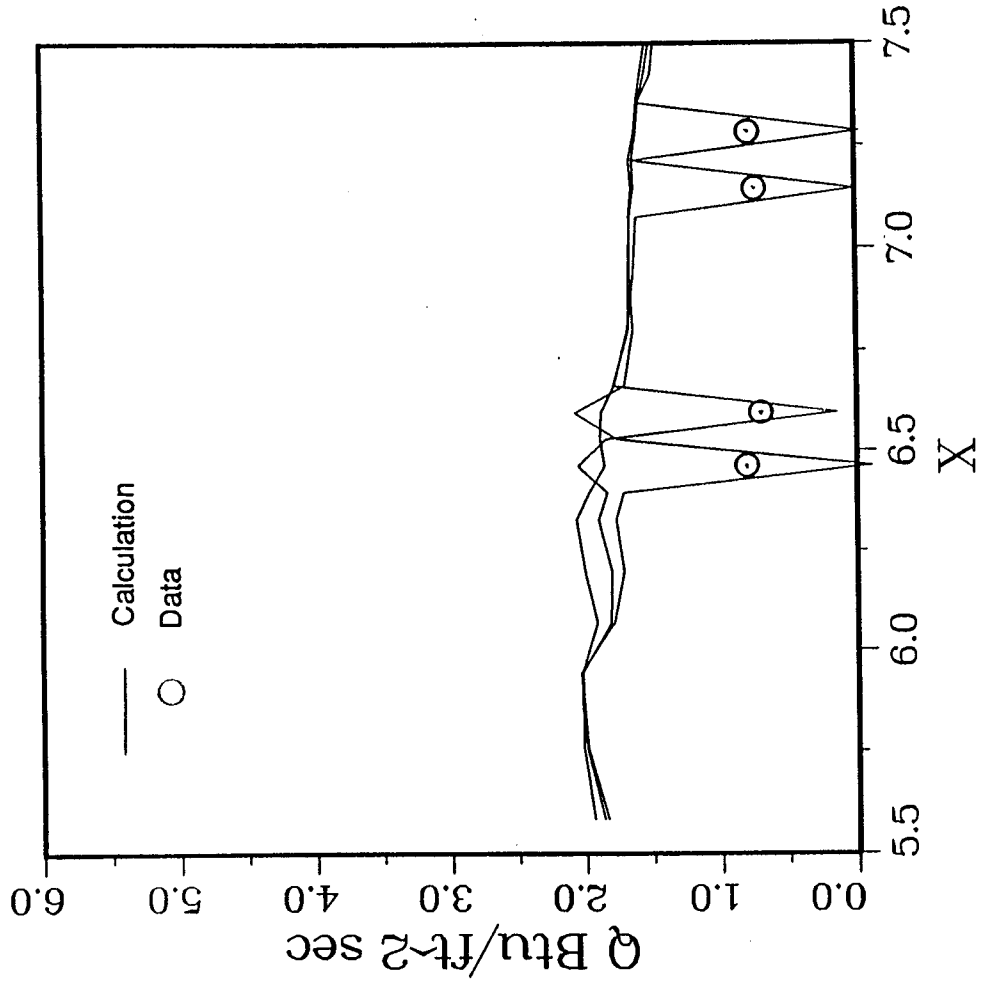
(b) $M_\infty = 4.0$, $\alpha = 4.0°$.

Figure 28. Continued.
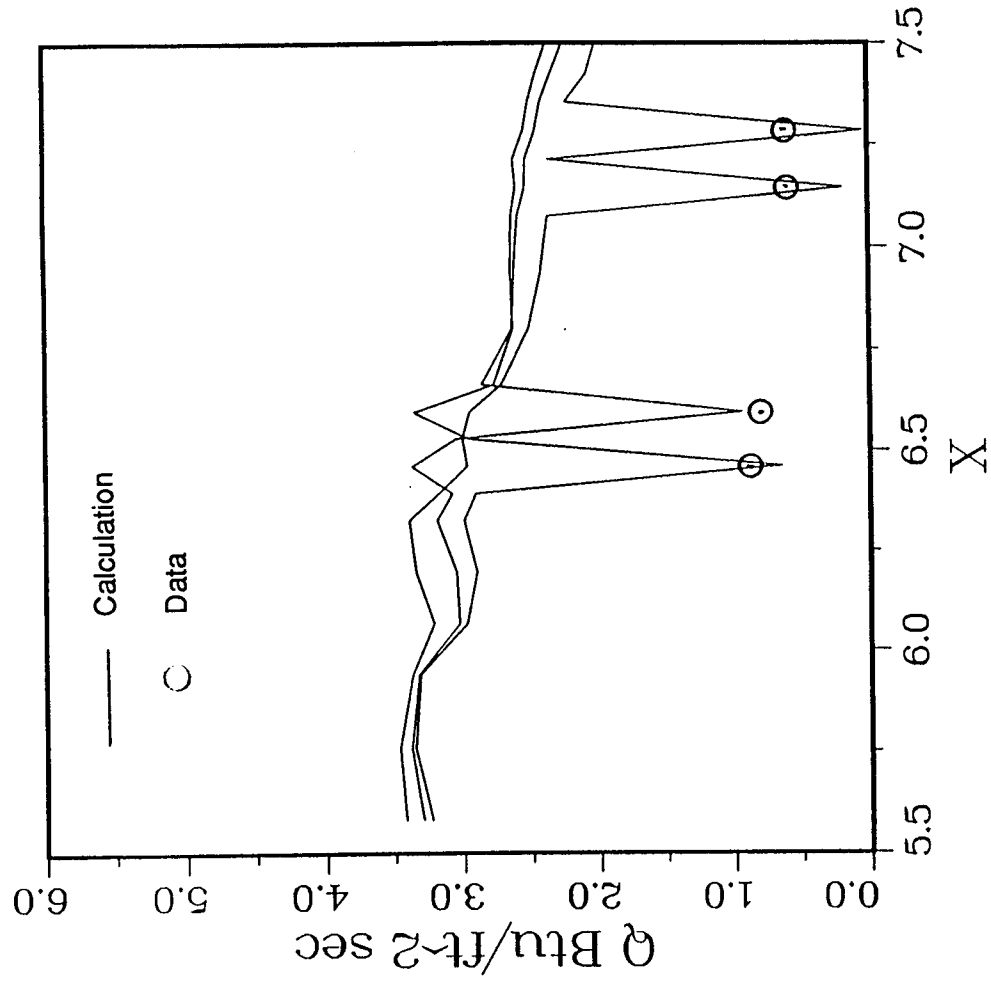
(c) $M_\infty = 5.0$, $\alpha = 0.5°$.

Figure 28. Concluded.

78
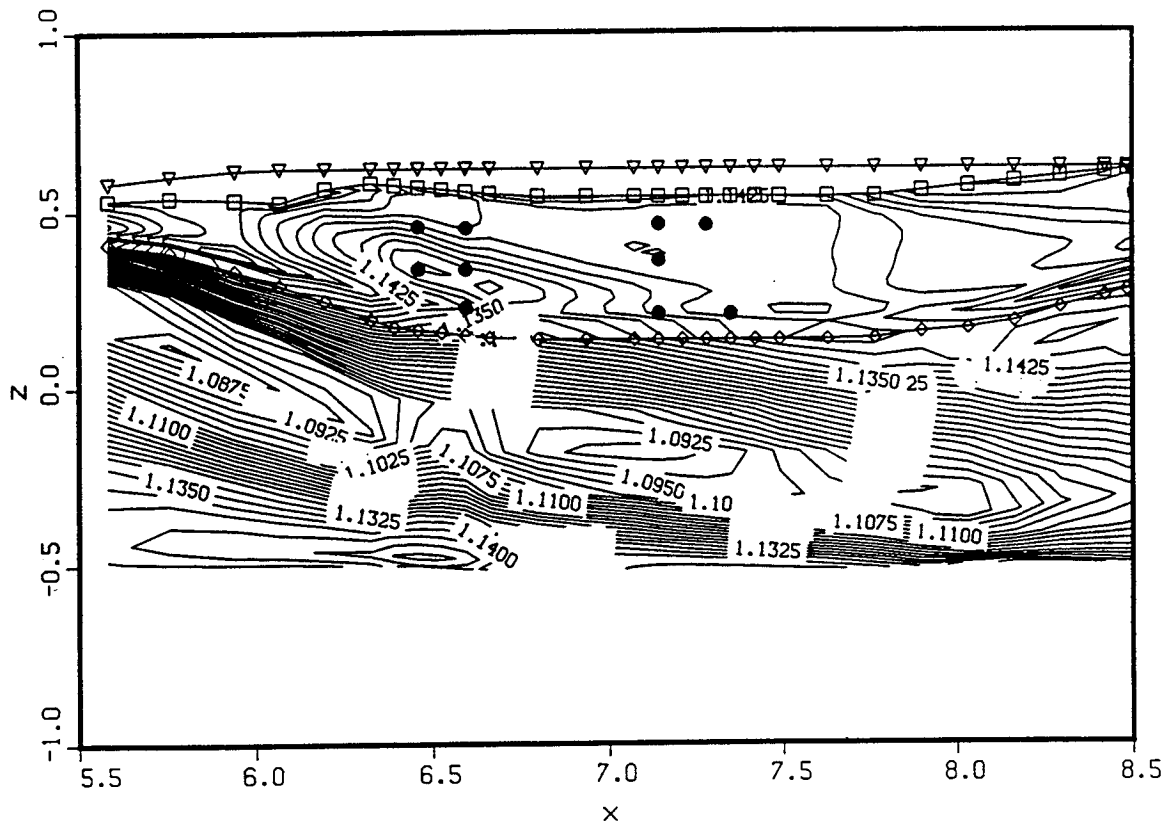
(a) $M_\infty = 3.1$, $\alpha = 7.5°$.

Figure 29. Temperature at $K=2$ on fillet sidewall for $M_\infty = 3.1$, 4.0, and 5.0 on sm2 grid.
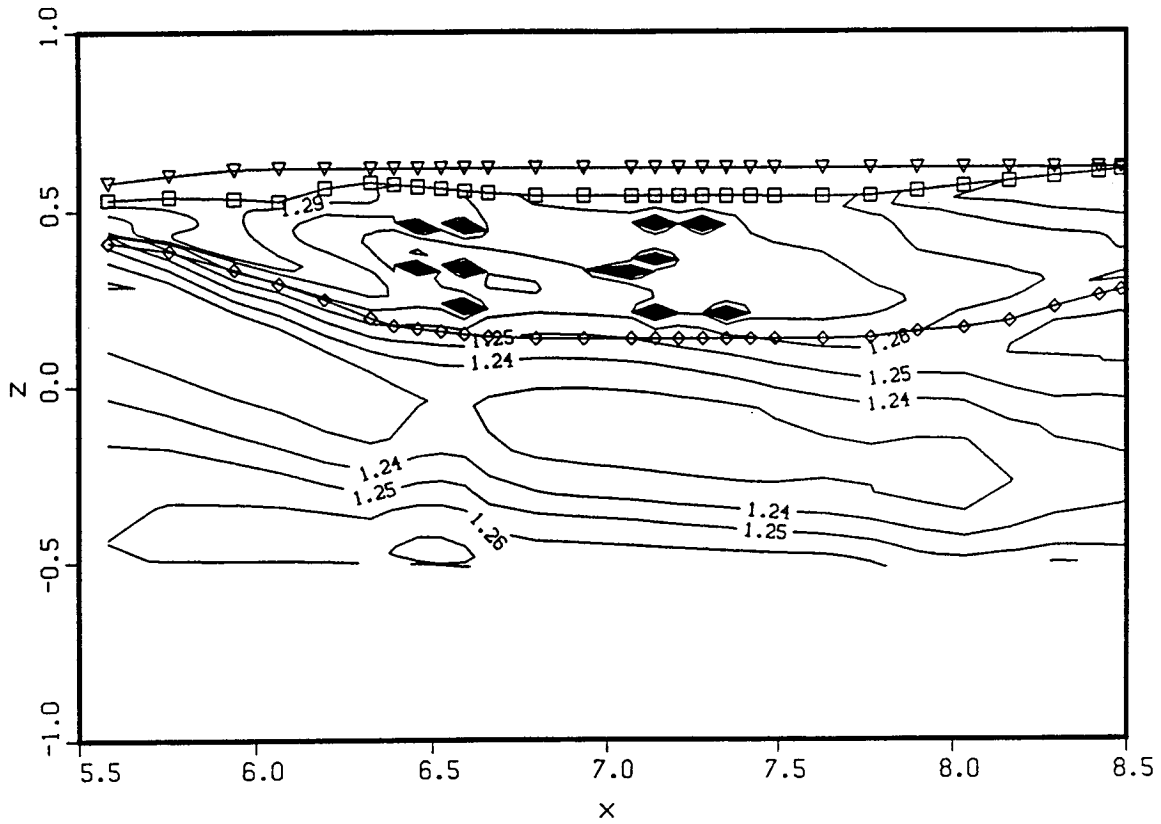
(b) $M_\infty = 4.0$, $\alpha = 4.0°$.

Figure 29. Continued.
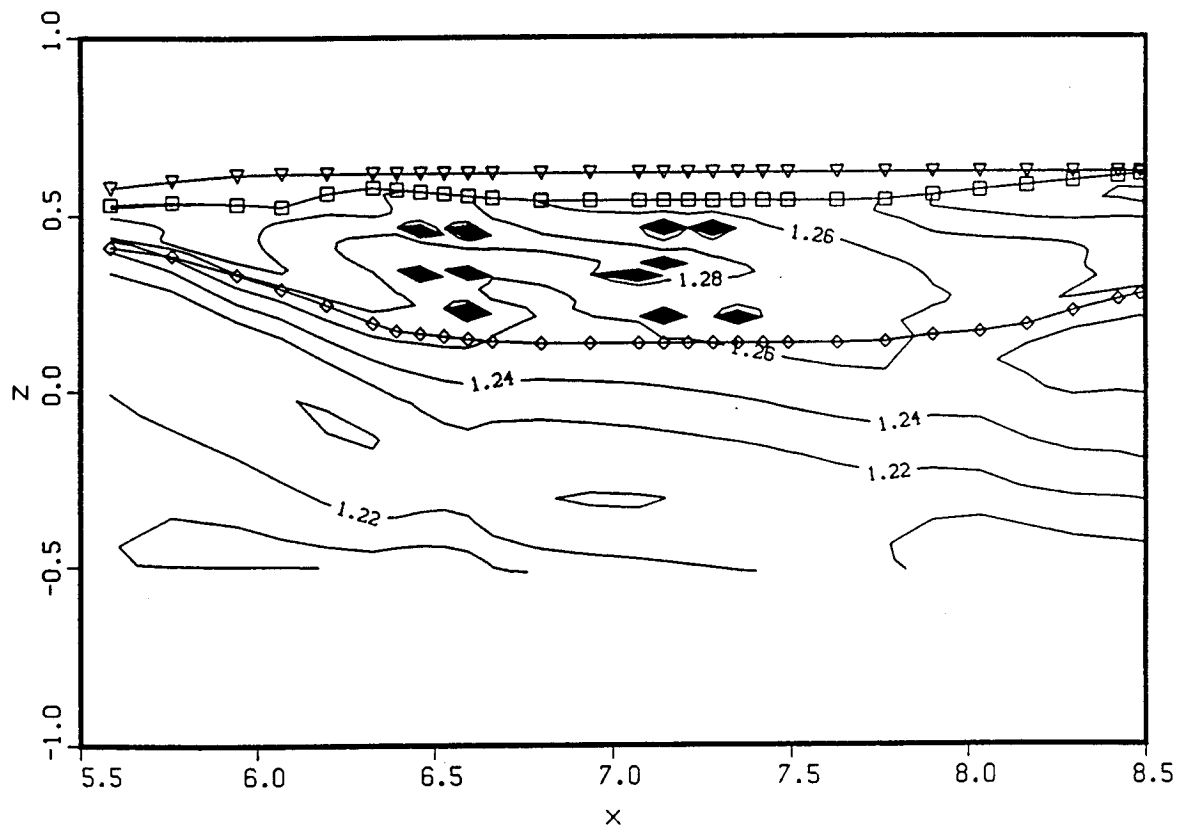
(c) $M_\infty = 5.0$, $\alpha = 0.5°$.

Figure 29. Concluded.
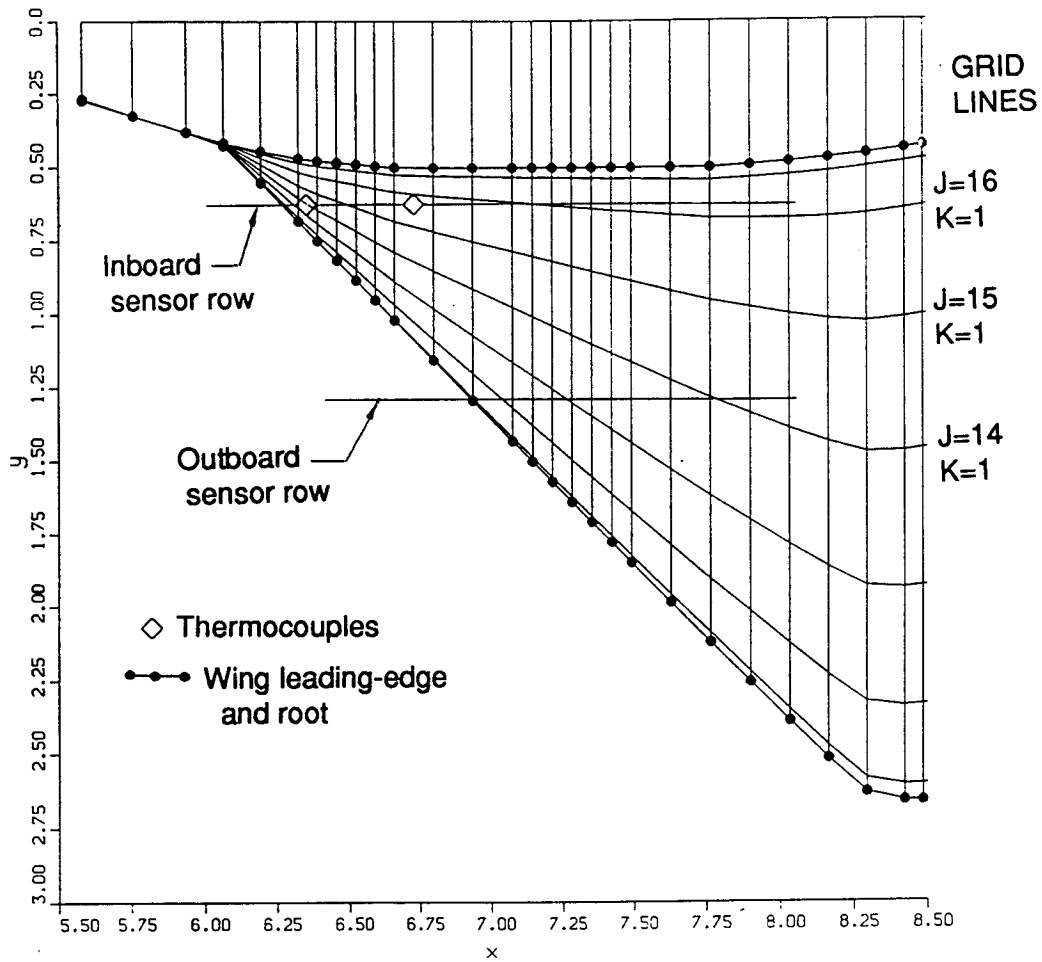
(a) Wing and lower surface grid planform.

Figure 30. Convective heat-flux studies on the wing.
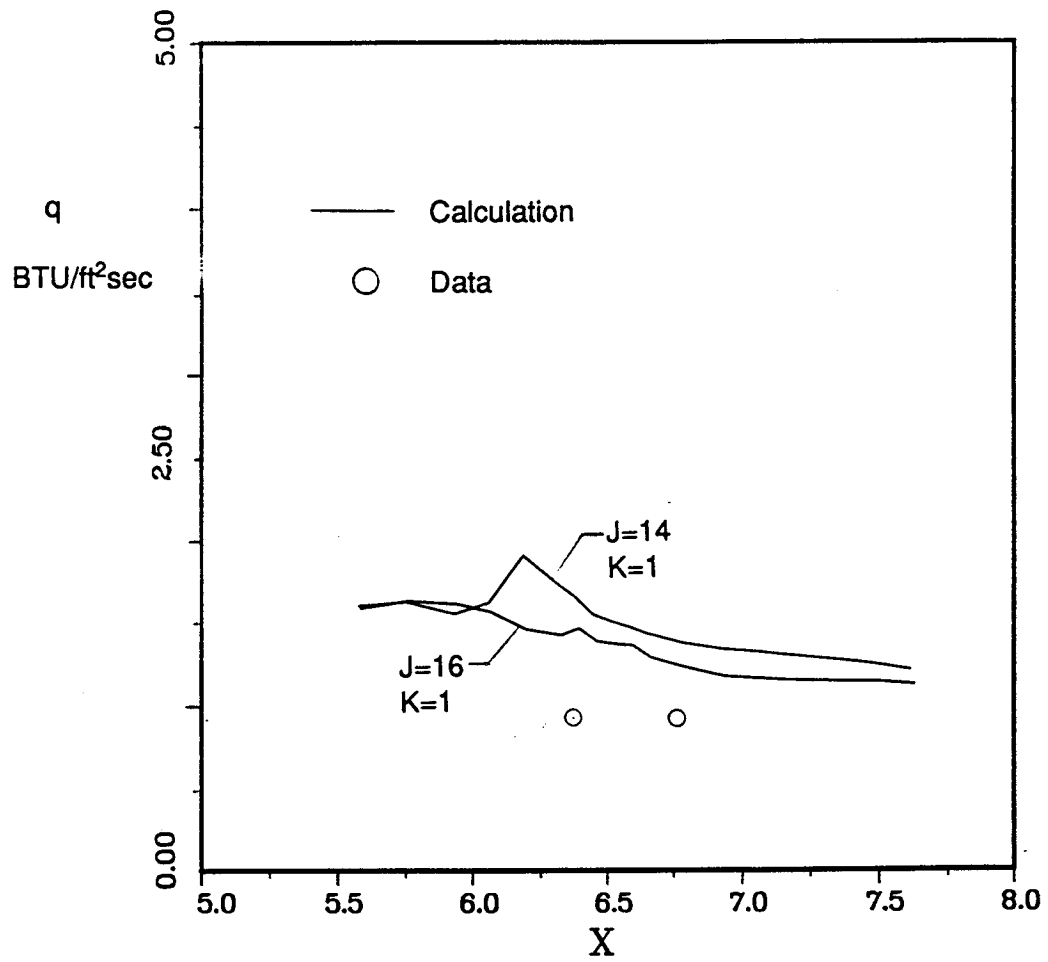
(b) Surface heat flux along grid lines J = 16 compared with data from inboard sensor row.

Figure 30. Concluded.

REPORT DOCUMENTATION PAGE

Public reporting burden for this collection of information is estimated to average 1 hour per response, including the time for reviewing instructions, searching existing data sources, gathering and maintaining the data needed, and completing and reviewing the collection of information. Send comments regarding this burden estimate or any other aspect of this collection of information, including suggestions for reducing this burden, to Washington Headquarters Services, Directorate for Information Operations and Reports, 1215 Jefferson Davis Highway, Suite 1204, Arlington, VA 22202-4302, and to the Office of Management and Budget, Paperwork Reduction Project (0704-0188), Washington, DC 20503.

1. AGENCY USE ONLY *(Leave blank)*	2. REPORT DATE March 1992	3. REPORT TYPE AND DATES COVERED Contractor Report-Final

4. TITLE AND SUBTITLE

Postflight Aerothermodynamic Analysis of Pegasus® Using Computational Fluid Dynamic Techniques

5. FUNDING NUMBERS

WU-505-66-71
NAS2-12722

6. AUTHOR(S)

Gary D. Kuhn

7. PERFORMING ORGANIZATION NAME(S) AND ADDRESS(ES)

Nielsen Engineering & Research, Inc.
510 Clyde Avenue
Mountain View, CA 94043-2287

8. PERFORMING ORGANIZATION REPORT NUMBER

H-1765

9. SPONSORING/MONITORING AGENCY NAME(S) AND ADDRESS(ES)

National Aeronautics and Space Administration
Washington, DC 20546-0001

10. SPONSORING/MONITORING AGENCY REPORT NUMBER

NASA CR-186017

11. SUPPLEMENTARY NOTES

This report was prepared for PRC Inc., P.O. Box 273, Edwards, California 93523-0273 by Nielsen Engineering & Research, Inc., under subcontract ATD-90-NER-6801. NASA Technical Monitor was Robert E. Curry, NASA Dryden Flight Research Facility, P.O. Box 273, Edwards, California 93523-0273. NASA Contracting Officer's Technical Representative for PRC Inc.: Donald C. Bacon, Jr., 805-258-3484.

12a. DISTRIBUTION/AVAILABILITY STATEMENT

Unclassified — Unlimited
Subject Category 02

12b. DISTRIBUTION CODE

13. ABSTRACT *(Maximum 200 words)*

The objective of this effort was to validate the computational capability of the NASA Ames Research Center's Navier-Stokes code, F3D, for flows at high Mach numbers using comparison flight test data from the Pegasus® air-launched, winged space booster. Comparisons were made with temperature and heat fluxes estimated from measurements on the wing surfaces and wing-fuselage fairing. Tests were conducted for solution convergence, sensitivity to grid density, and effects of distributing grid points to provide high density near temperature and heat-flux sensors. The measured temperatures were from sensors embedded in the ablating thermal protection system. Surface heat fluxes were from plugs fabricated of highly insulative, nonablating material, and mounted level with the surface of the surrounding ablative material. As a preflight-design tool, the F3D code produces accurate predictions of heat transfer and other aerodynamic properties, and it can provide detailed data for assessment of boundary layer separation, shock waves, and vortex formation. As a postflight-analysis tool, the code provides a way to clarify and interpret the measured results.

®Pegasus is a registered trademark of Orbital Sciences Corp., Fairfax, Virginia.

14. SUBJECT TERMS

Computational fluid dynamics; Pegasus; Hypersonics; Aerothermodynamics; Wing-body aerodynamics

15. NUMBER OF PAGES
87

16. PRICE CODE
A05

17. SECURITY CLASSIFICATION OF REPORT	18. SECURITY CLASSIFICATION OF THIS PAGE	19. SECURITY CLASSIFICATION OF ABSTRACT	20. LIMITATION OF ABSTRACT
Unclassified	Unclassified	Unclassified	Unlimited

NSN 7540-01-280-5500

Standard Form 298 (Rev. 2-89)
Prescribed by ANSI Std. Z39-18
298-102